# Preparation and Application of Surface Science Model Catalysts in Realistic Conditions

**Dissertation**

zur Erlangung des akademischen Grades

**Doktor der Naturwissenschaften (Dr. rer. nat.)**

im Fach Physik

eingereicht im Fachbereich Physik

der Freien Universität Berlin

vorgelegt am 20. September 2013 von

**Franziska Ringleb**

Promotionskomitee:
Vorsitzender      Prof. Dr. K. Heyne
Gutachter          Prof. Dr. H.-J. Freund
Gutachter          Prof. Dr. H. Dau

Tag der wissenschaftlichen Aussprache: 28.10.2013

Diese Arbeit wurde von Januar 2010 bis September 2013 am Fritz - Haber - Institut der Max - Planck - Gesellschaft in der Abteilung Chemische Physik unter Anleitung von Prof. H. - J. Freund angefertigt.

# Abstract

Surface science model catalysts are elementary representations of applied systems by which different parameters of a catalytic process can be investigated separately and at the molecular scale. Studies on such model systems constitute the basis for present studies which aim at bridging the materials and pressure gap towards applied catalysts systematically. In this framework, the present thesis contributes to this goal by applying two approaches towards more realistic catalyst models.

The first part of this work documents research on ultrathin, metal supported oxide films in ambient conditions. FeO(111)/Pt(111) films were exposed to air and water and tested regarding CO oxidation at ambient pressure by infrared reflection absorption spectroscopy (IRAS). Pre- and post characterization was performed by low energy electron diffraction (LEED), temperature programmed desorption (TPD) and X-ray photoelectron spectroscopy (XPS). Experimental and theoretical results suggest, that in the presence of oxygen and water, a bilayer (FeO) → trilayer (FeO(OH)) transition occurs. The resulting FeO(OH) trilayer is stable in ambient conditions and shows similar CO oxidation activity at ambient pressure as previously reported for $FeO_2$ [1]. Ultrahin MgO(001) films grown on Ag(001) and Mo(001) were likewise tested for CO oxidation activity at 1 bar total pressure and characterized by XPS. Theoretical [2] and ultrahigh vacuum (UHV) studies [3] had indicated that these systems might efficiently activate molecular oxygen. However, no catalytic activity for ultrathin MgO(001) films in ambient conditions was observed.

The second part of this work presents an approach which takes into account the fact that most applied heterogeneous catalysts are prepared by wet chemical methods. Here, a Pd catalyst was prepared by liquid phase deposition (LPD) from a $PdCl_2$ precursor solution onto a MgO(001)/Ag(001) model support. Dissolution experiments, where the samples were post-characterized by AES (Auger electron spectroscopy), showed that MgO/Ag(001) films are only long-term stable in alkaline solutions. The XPS data indicates a linear correlation between Pd loading and precursor concentration. XPS was also used to characterize the thermally induced precursor decomposition at relevant stages. The activated LPD catalysts showed similar CO adsorption properties and activity towards CO oxidation as corresponding catalysts prepared by PVD (physical vapor deposition) - which is evidenced by TPD measurements.

# Zusammenfassung

Surface Science Modellkatalysatoren sind stark vereinfachte Ausführungen angewandter Katalysatoren. Sie ermöglichen es, verschiedene Parameter eines katalytischen Prozesses getrennt voneinander und auf molekularer Ebene zu untersuchen. Bisherige Studien solcher Modellsysteme stellen die Grundlage dar für die heutige Forschung, die bestrebt ist, existierende Diskrepanzen der Druckbereiche (*pressure gap*) sowie der Material - und Strukturkomplexität (*material gap*) zwischen Modellen und angewandten Systemen systematisch zu verringern.

Der erste Teil der vorliegenden Arbeit dokumentiert Untersuchungen von ultradünnen, metallgeträgerten Oxidfilmen unter Umgebungsbedingungen. FeO(111)/Pt(111) Filme wurden Luft und Wasser ausgesetzt und bezüglich ihrer katalytischen Aktivität hinsichtlich der Oxidation von CO unter Umgebungsdruck mittels Infrarot - Reflexions - Absorptionsspektroskopie (IRAS) getestet. Die Prä - und Postcharakterisierung wurde anhand von niederenergetischer Elektronenbeugung (LEED), temperaturprogrammierter Desorption (TPD) und Röntgenphotoelektronenspektroskopie (XPS) durchgeführt. Experimentelle und theoretische Ergebnisse deuten darauf hin, dass in Gegenwart von Sauerstoff und Wasser ein Übergang vom zweilagigen FeO zu einem dreilagigen FeO(OH) Film stattfindet. Die FeO(OH) Dreilage ist stabil unter Umgebungsbedingungen und besitzt eine ähnliche katalytische Aktivität gegenüber der Oxidation von CO unter Umgebungsdruck wie $FeO_2$ [1]. Ultradünne MgO Filme auf Ag(001) und Mo(001) wurden ebenfalls auf katalytische Aktivität bezüglich der CO Oxidation unter Umgebungsdruck untersucht und mittels XPS charakterisiert. Theoretische Studien und Experimente im UHV hatten darauf hingedeutet, dass diese Systeme in der Lage sind, molekularen Sauerstoff zu aktivieren. Es wurde jedoch keine katalytische Aktivität ultradünner MgO Filme unter Umgebungsbedingungen beobachtet.

Der zweite Teil dieser Dissertation zeigt einen Ansatz auf, welcher der Tatsache Rechnung trägt, dass die Mehrheit der angewandten heterogenen Katalysatoren mit Hilfe nass - chemischer Methoden hergestellt wird. In dieser Arbeit wurde ein Pd Katalysator durch Flüssigphasenabscheidung (LPD) aus einer $PdCl_2$ Präkursorenlösung auf einem MgO/Ag(001) Modellsubstrat abgeschieden. Auflösungsexperimente, bei denen die Proben durch Auger Elektronenspektroskopie (AES) post - charakterisiert wurden, zeigten, dass dünne MgO/Ag(001) nur in alkalischen Lösungen über einen längeren Zeitraum stabil sind. Die XPS Daten weisen auf eine lineare Korrelation zwischen der Pd Konzentration in der Lösung und der Menge an abgeschiedenem Pd hin. Die schrittweise thermische Zersetzung der Pd - Präkursoren wurde mit XPS untersucht. TPD Messungen zeigten, dass der aktivierte Pd - LPD Katalysator sich durch ähnliche CO - Desorptionseigenschaften und Aktivität gegenüber der Oxidation von CO auszeichnete wie ein entsprechender Pd Katalysator, der mittels PVD (physikalische Gasphasenabscheidung) hergestellt wurde.

# Contents

# Contents

# List of Figures

# List of Tables

# Acronyms

DFT .......... density functional theory
EELS ......... electron energy loss spectroscopy
EPR .......... electron paramagnetic resonance
HSA .......... hemispherical analyzer
IR ............. infrared
IRAS ......... infrared reflection absorption spectroscopy
ISS ........... ion scattering spectroscopy
LEED ........ low energy electron diffraction
LEEM ........ low energy electron microscopy
LIA ........... lock in amplifier
LPD .......... liquid phase deposition
PM‑IRAS .... polarization‑modulation infrared reflection absorption spectroscopy
PVD .......... physical vapor deposition
PZC ........... point of zero charge
RFA ........... retarding field analyzer
STM .......... scanning tunneling microscopy
STS ........... scanning tunneling spectroscopy
TPD .......... temperature programmed desorption
UHV .......... ultra high vacuum
UPS ........... ultraviolet photoelectron spectroscopy
XPS ........... x-ray photoelectron spectroscopy

# Chapter 1.

# Introduction

Heterogeneous catalysis is of paramount importance for the production of industrial goods and therefore the maintenance of our current living standards, but also for meeting upcoming environmental [4] and energy‑related [5, 6] challenges. Supported metal and metal oxide catalysts represent the most important class of heterogeneous catalysts in industrial practice [7].

In the past, the huge benefit of efficiently working catalysts has motivated intense research to understand fundamental principles of catalysis. However, catalysts for specific purposes can still not be designed *ab initio*. Often, one has to rely on trial‑and error methods without any guarantee to actually obtain the optimum catalyst in the end.

This situation is evidence for the great challenge of fundamental catalysis research. Its bottom up approach aims at understanding catalytic processes in detail and at the molecular scale. A comprehensive understanding of catalysis would ideally allow to find the global optimum of catalyst parameters for specific reactions by intelligent catalyst design. Surface science has contributed to a great extent to the accumulation of elementary knowledge and will remain indispensable in the future to answer remaining questions.

Surface science techniques are, however, not applicable for most industrial catalysts. First of all, these methods require mostly conductive samples. Secondly, they were developed for UHV conditions. This was done for good reason. Cleanliness of the freshly sputtered surfaces is provided for minutes or hours. But most of all, particles, by which the surfaces are probed (electrons, ions, atoms) have long inelastic mean free paths which allow comfortable distances between sample and detector.

Still, large discrepancies between surface science models and applied catalysts remain. They can be summed up as the *materials gap* which describes the differences in complexity ('simple' model systems vs. highly complex real catalysts) and the *pressure gap* which refers to the differences in reaction conditions (UHV vs. ambient or even higher pressures). In principle, there exists also a *preparation gap*, since model catalysts are commonly prepared by physical vapor deposition (PVD) in UHV whereas in industry, almost all supported catalysts are made by wet chemical impregnation of the support [8, 9]. The choice of preparation conditions affects the chemical and structural properties of catalysts, and hence, can lead to variations in the catalytic performance. In summary, the simplicity of model systems in contrast to the high complexity of applied catalysts is problematic since it renders the application of fundamental knowledge from surface science research in the real world difficult if not impossible in many cases.

Meanwhile, new conceptual and methodological developments have contributed to tackle this problem. In the initial stages of surface science research, the systems investigated were simplified as far as possible. Metal single crystal surfaces were investigated at low temperatures in UHV. Obviously, these systems are not adequate models of the real world. Still, important fundamental knowledge has been obtained from these studies which constitute the basis for ongoing research. More recently, dispersed metal particles on top of thin, metal single crystal supported oxide films have been introduced as model systems [10, 11]. They constitute a good compromise, since they comprise the most important components of standard catalysts - metal particles dispersed on an oxide - in a simplified manner and allow at the same time surface science techniques to be applied. Furthermore, their structure is of intermediate complexity, since the metal single crystal serves as a template for the oxide film growth, such that the oxides surfaces are still well defined.

To bridge the pressure gap, methods such as high pressure XPS [12], high pressure PM - IRAS [13], high pressure STM [14] and high pressure SFG [15, 16] are nowadays available and widely applied in fundamental catalysis research.

Research addressing the preparation gap has been less intense so far. There are a few studies available which report on surface science investigations into catalysts prepared by wet chemical procedures [17, 8, 18, 19]. In our group, the effects of exposing model supports to water vapor, ambient atmosphere and aqueous solutions have been studied in the past. Furthermore, catalysts were prepared by liquid phase deposition (LPD) on thin, metal single crystal supported oxide films [20].

This thesis follows up that previous work and contributes to bridging both the pressure and preparation gap. The first part deals with ultrathin films which have recently attracted increasing attention when it was found that they can exhibit outstanding catalytic activity due to their unique properties [21]. The present work focuses on the structural and catalytic properties of ultrathin MgO and FeO films, supported on metal single crystals, in ambient conditions.

The second part addresses particularly the preparation gap. MgO films grown on Ag(001) were utilized as a support for the preparation of a Pd catalyst by LPD. While getting closer to realistic conditions regarding the preparation procedure, full advantage could be taken of the surface science techniques available in our lab to get comprehensive information about the sample morphology and chemistry.

The thesis is organized as follows:

**Chapter 2** The experimental methods employed in this work are explained with respect to their theoretical background as well as the working principles of the instruments. The experimental setups, i.e. the IRAS - chamber, the STM - chamber and the SFG - chamber are described in detail.

**Chapter 3** The behaviour of ultrathin FeO films on Pt(111) at elevated pressures and in ambient conditions upon exposure to air and water is documented

and chemical and structural modifications are discussed. Results which illustrate the interaction of these films with small amounts of Au are shown. They are discussed in the framework of charge transfer from or to adatoms on ultrathin films. Finally, results about the catalytic activity of the FeO(OH)/Pt(111) system towards CO oxidation are shown.

**Chapter 4** Results of CO oxidation experiments on ultrathin MgO films are presented in this chapter. Films of different thicknesses were grown on two metal supports: Ag(001) and Mo(001). Their catalytic activity was tested in different CO:$O_2$ reaction mixtures balanced with He to ambient pressure.

**Chapter 5** This chapter summarizes the efforts to prepare a Pd-MgO/Ag(001) catalyst by LPD. As a first step, the stability of MgO films in aqueous solutions of different pH was tested. Subsequently, Pd-MgO/Ag(001) catalysts were prepared by exposing MgO(001)/Ag(001) thin films to a Pd precursor solution. The influence of varying deposition time, precursor concentration and other parameters on the loading and final state of the annealed catalyst was investigated. By means of temperature programmed desorption (TPD) measurements, CO adsorption as well as CO oxidation of LPD prepared Pd/MgO/Ag samples are compared to corresponding samples prepared by PVD.

**Chapter 6** Here, the most important findings of this work are summarized. This chapter also provides suggestions for further research in this field.

# Chapter 2.

# Methods and Experimental Setup

## 2.1. X-Ray Photoelectron Spectroscopy (XPS)

### 2.1.1. Introduction

XPS is a a specific type of electron spectroscopy and a very powerful technique for surface sensitive chemical analysis which was developed by Siegbahn and coworkers during the 1950's. Its popularity originates from the high information content, wide range of applications (all elements except Hydrogen and Helium can be analyzed) and its solid theoretical basis [22]. The technique is based on the determination of element specific binding energies of electrons in the atomic shells by a spectrometer. It takes advantage of the photoelectric effect by analyzing kinetic energies of photoelectrons ejected from the sample surface by X-rays.

### 2.1.2. Experimental Setup

The general XPS setup consists of an X-ray source pointing towards the sample, an analyzer system selecting electrons according to their kinetic energy and a detector. Commonly, the X-ray gun is equipped with a Mg $K_\alpha$(1253.6 eV) and an Al $K_\alpha$(1486.6 eV) source. This allows for excitation with two different energies and, therefore, for example, the easy distinction between XPS and Auger peaks. The X-ray source points towards the sample which has to be grounded in order to avoid charging which in turn causes an artificial shift of the peaks. The analyzer has to be connected to the same ground such that the Fermi levels of sample and analyzer are aligned. This, in turn, allows for the assignment of peaks to their corresponding binding energies. From figure 2.1 it becomes clear that, without knowing the photoelectrons initial kinetic energy $E_{kin,sample}$ or the samples work function $\varphi_{sample}$, the binding energy $BE$ can be expressed as:

$$BE = h\nu - E_{kin,analyzer} - \varphi_{analyzer} \tag{2.1}$$

So in order to determine the binding energy, the kinetic energy distribution has to be determined. This is done by a hemispherical analyzer (HSA). A simplified scheme of a HSA is shown in figure 2.2. The electrons ejected from the sample are focused by an electrostatic lens system onto the entrance slit. Subsequently, they enter the space between two hemispheres where they follow a trajectory which depends on their kinetic energy. The outer hemisphere is put on a negative potential $-V$ with respect to the inner hemisphere. Only electrons whose kinetic
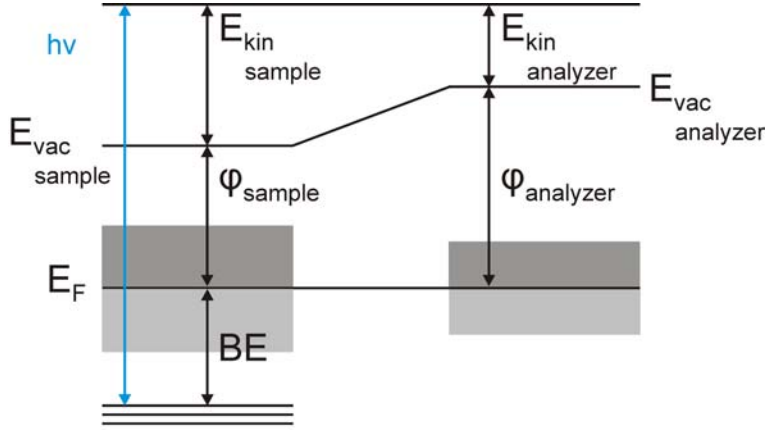
Figure 2.1.: Energy scheme of an XPS process: Sample and analyzer are electrically connected, such that the Fermi level is equal across the whole system. Knowing the excitation energy of the photons and the work function of the analyzer (a known constant) is then sufficient to calculate the binding energies of the core electrons

energy lies within a small interval around $E_{kin} = k_s e \Delta V$ ($k_s$ = device constant, $e$ = elementary charge) will finally reach the multichannel detector system.

### 2.1.3. Resolution and Line Shape

The energy resolution in XPS is in principle limited by the line width of the X-ray source $\Delta E_s$, the natural line width $\Delta E_0$ of the photoelectron process, local screening effects $\Delta E_{scr}$ and the resolution of the analyzer $\Delta E_a$. The full width at half maximum $\Delta E$ of a photoelectron peak adds (in Gaussian approximation) up to:

$$\Delta E = (\Delta E_s^2 + \Delta E_0^2 + \Delta E_{scr}^2 + \Delta E_a^2)^{\frac{1}{2}}$$

Narrow lines, such as Ag 3d are used for testing the analyzer resolution. The natural line width is determined by the lifetime $\tau$ of the core hole and can be estimated by the uncertainty principle as $\Delta E_0 = \frac{h}{\tau}$ with $h$ being the Planck constant. The energy resolution of the analyzer is proportional to the magnitude of the pass energy. In order to keep the resolution constant across a scan, the pass energy is usually fixed and the retardation of incoming electrons is varied instead by a lens system in front of the entrance slit.

The natural line shape of the photoemission process is a Lorentzian curve, but in addition, Gaussian broadening is caused by the analyzer. Therefore, the line shape of a symmetric XPS peak is well represented by a convolution of a Lorentzian and a Gaussian curve (Voigt profile). Photoelectrons in metals
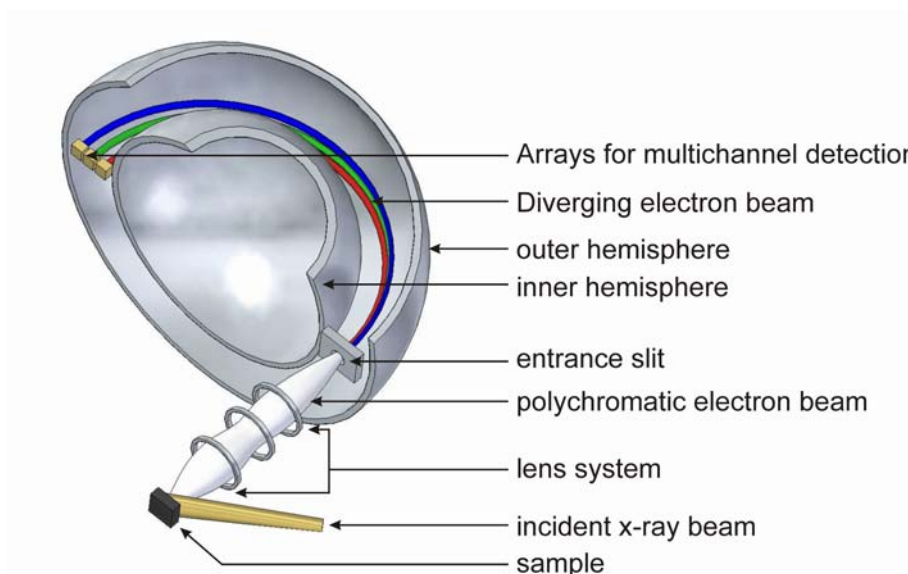
Figure 2.2.: Schematic representation of a hemispherical analyzer. It can be used for different techniques to measure the kinetic energy of various sorts of charged particles. In XPS, electrons are analyzed. In ion scattering spectroscopy (ISS), positively charged gas ions are analyzed.

with a high density of states near the fermi edge may suffer energy losses due to excitations into empty states above the Fermi level. Therefore, they often exhibit a tail at the high binding energy side of core peak which results in an asymmetric peak shape [23]. In the data analysis, this can be accounted for by fitting these curves with the so-called Doniach Sunjic (D-S) line shape which contains a characteristic asymmetry factor [24] (see figure 2.3).

### 2.1.4. Spectral Features

The core level states have energies that are characteristic for each element. The energies depend on the prinipal quantum number $n$, the orbital momentum $\vec{l}$ and the total angular momentum $\vec{j}$. The general notation for an XPS peak - $nl_j$ - therefore includes these three parameters. An electron with orbital momentum $\vec{l}$ and spin $\vec{s}$ has a total angular momentum of $\vec{j} = \vec{l} + \vec{s}$. Since the unpaired electron left after photoemission has either a parallel or an antiparallel orientation to the orbital momentum, each level with a non-zero angular momentum is split into a doublet (spin orbit coupling). The two peaks of a doublet have specific area ratios based on the degeneracy of states. For each $\vec{j}$, there are $2j+1$ states, which are characterized by the magnetic quantum number $m_j$. In a p orbital, for example, there will be 2 states for the $j = 1/2$ and four states for $j = 3/2$. Therefore, the $p_{1/2} : p_{3/2}$ peak ratio is $1 : 2$. It follows that the ratios for $d_{3/2} : d_{5/2}$ and $f_{5/2} : f_{7/2}$ are $2 : 3$ and $3 : 4$, respectively. Another parameter which is constant for a particular doublet is the energetic distance between the two sublevels. Both
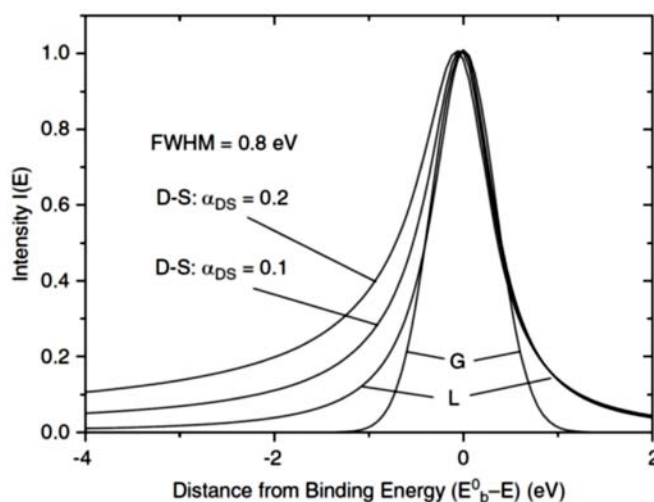
Figure 2.3.: Lorentz (L), Gauss (G) and Doniach Sunjic (D-S) functions for XPS peak fitting. The D-S function is plotted for different asymmetry factors $\alpha_{DS}$. Increasing values of $\alpha_{DS}$ lead to a small, but measurable shift to higher binding energy. Furthermore, it affects the full width at half maximum. (from [23])

the peak ratio and energy separation are helpful for fitting data, in particular in the case of overlapping doublets.

Apart from the core level peaks, several other features are detected in a broad range XPS spectrum.

- *Shake-up and shake-off lines:* When a photoelectron is emitted, there is a finite probability that the remaining ion is left in an excited state. The photoelectron energy is reduced in this case. This leads to a satellite peak at the high binding energy side of the core level peak. An example for a Shake-up line is the $\pi \rightarrow \pi^*$ line for carbon in aromatic compounds. Similarly, *Shake-off* events, where more than one electron is ejected at the time of photoionization, may result in energy losses of the primary photoelectron and therefore in broad structures at the high binding side of a core level peak.

- *Multiplet splitting:* Photoionization of an atom which has originally a non-zero spin can result in a coupling of the newly created unpaired electron left after photoemission with other unpaired electrons in the atom resulting in more than one possible final state. As a result, multiplet splitting occurs which can be observed best for photoemission from s orbitals [25].

- *Plasmon losses:* The outgoing photoelectrons can excite surface or bulk plasmons (collective oscillations of the electron gas) which leads to a peak at the high binding energy side of the core level peak. Surface plasmon peaks have generally lower intensities than the bulk plasmon peaks and their frequency is lower by about a factor of $\sqrt{2}$.

7

- *Auger electrons:* (see section 2.2 for the details of the Auger process) Auger electrons give rise to additional peaks in the spectrum. In contrast to primary photoelectrons, their kinetic energy is independent of the X-ray photon energy. Therefore, they can be distinguished from primary photoelectron peaks by changing the excitation energy.

- *Valence lines and bands:* At low energies (10-20 eV above the Fermi edge) low intensity lines and bands occur in the spectrum. They originate from photoelectrons from molecular orbitals or solid state valence bands.

A typical photoelectron spectrum is shown in figure 2.4. It can be plotted with a kinetic energy scale - the energy, that is actually measured. By using equation 2.1, the scale can also be expressed in terms of binding energy. The Fermi edge corresponds to the binding energy zero.
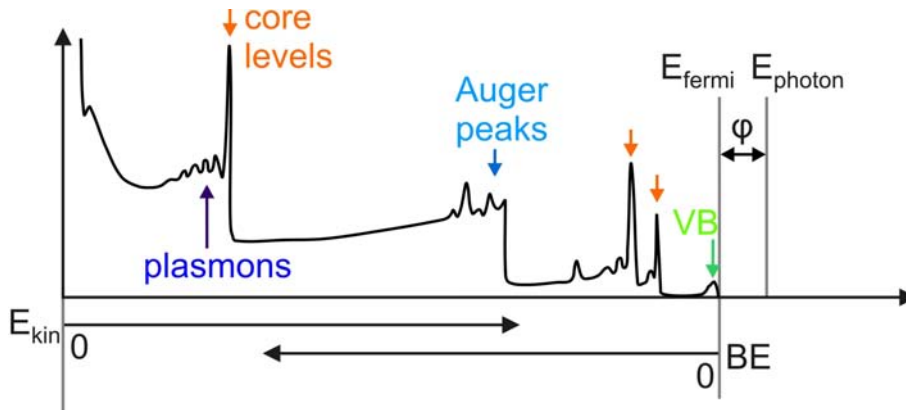


Figure 2.4.: Typical XPS spectrum. Apart from core level and valence band peaks, features due to energy losses of the primary electrons and Auger features can be observed.

### 2.1.5. Determination of the Chemical State

Even though the rough position of core level and Auger peaks is like a fingerprint for each element, several effects lead to an energy shift of these peaks, from which information about the chemical state can be obtained.

Ignoring final state effects, chemical shifts can be explained by a change of electron potential in an atom. This can occur due to a charge transfer between atoms of different electronegativity. Therefore, metals in metal oxides, for example, show typically a shift towards higher binding energies with an increasing oxidation state of the metal. Apparent binding energy shifts can, however, also be induced by a change of polarizability, band banding, particle size effects and charging of the surface.

The modified Auger parameter allows to determine the chemical state, since it is independent of static charging and does not require a work function correction [23]. Furthermore, it allows to disentangle the contributions of (i) extra-

atomic relaxation energy (polarization energy involving electrons from neighbouring atoms) $\Delta R_{ea}$ and (ii) the energy shift of the electronic ground state $\Delta V_i$ to the apparent binding energy shift. The modified Auger parameter $\alpha'_{AP}$ is defined as the sum of the Auger kinetic energy $E_{kin,AES}$ and the binding energy $E_{b,XPS}$ of a photoelectron peak of the same element.

$$\alpha'_{AP} = E_{kin,AES} + E_{b,XPS}$$

Both $E_{kin,AES}$ and $E_{b,XPS}$ depend on the analyzer work function and charging potentials, but these parameters cancel in the sum. Variations of the modified Auger parameter are based on the fact that Auger peaks usually shift stronger than photoelectron peaks upon a change of chemical state or the chemical environment. Since the chemical shifts in different shells are experimentally closely the same, the core level shift $\Delta E_{b,XPS}$ and the kinetic energy shift of the Auger electron $\Delta E_{kin,AES}$ can be expressed in the simplest approximation as

$$\Delta E_{b,XPS} = \Delta V_i - \Delta R_{ea}$$

$$\Delta E_{kin,AES} = -(\Delta V_i - 3\Delta R_{ea})$$

such that

$$\alpha'_{AP} = 2\Delta R_{ea}$$

The different dependence of $\Delta E_{b,XPS}$ and $\Delta E_{kin,AES}$ on $\Delta R_{ea}$ is due to the fact that photoelectron emission leads to a one core hole final state whereas an Auger process leads to a two core hole final state.

For a KLL transition, for example, $\Delta E_{kin,AES}$ can be expressed according to Wagner [26] as :

$$\Delta E_{kin,KLL} = -\Delta V_i(L) + \Delta R_{ea}(L^+L^+) - \Delta R_{ea}(K^+)$$

Since $R_{ea}$ is proportional to the square of the charging, it follows that $\Delta R_{ea}(L^+L^+)$ and $\Delta R_{ea}(K^+)$ differ by a factor for four and thus

$$\Delta E_{kin,KLL} = -\Delta V_i(L) + 3\Delta R_{ea}(K^+)$$

## 2.2. Auger Electron Spectroscopy (AES)

### 2.2.1. General Aspects

In a series of papers starting in 1923, Pierre Auger reported the spontaneous emission of monoenergetic electrons that had been emitted from atoms [27]. What he had observed is actually the result of a three electron process which is initiated by the removal of core electrons. The unoccupied state which is left behind is filled again, since the system is aiming at reaching the ground state. When an electron from a higher orbital or the valence band fills this hole, it loses
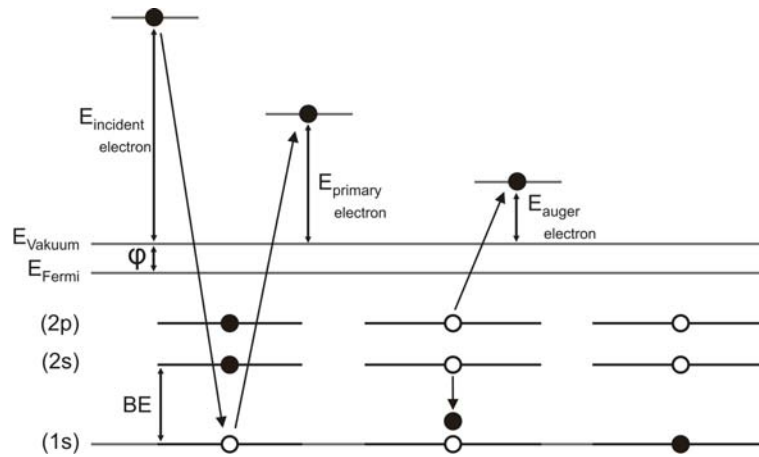
Figure 2.5.: Energy scheme of an Auger process: Initially, a core electron is removed, for example by an x-ray photon or an electron with high kinetic energy (left side). Subsequently, an electron from a higher shell fills the core shell. The energy released can be transferred to a second electron which is ejected with an energy depending on the different orbital energies (right side). However, alternative processes to ejection of an Auger are also possible.

energy that can either be dissipated by electromagnetic radiation or by exciting a secondary electron, a so called Auger electron, which then leaves the sample as well. Since for an Auger process a minimum of three electrons is involved, it can only be observed in elements with an atomic number $\geq 3$.

The Auger transitions appear in the kinetic energy spectrum as distinct peaks. However, the spectra have, in general, a very high background due to inelastically scattered primary electrons and all kinds of secondary processes. Therefore, instead of plotting the density of kinetic energy states N(E), it is common to plot the derivative N'(E) of this magnitude. In nowadays experiments, the excitation source is usually an electron beam with an energy of 3 - 30 keV. The escape depth of the Auger electrons for most elements is 1 - 3 nm for kinetic energies below 2 keV which is typical for Auger transitions. By applying experimentally determined sensitivity factors, it is also possible to make quantitative estimates with 10 - 50% precision.

## 2.2.2. Setup and Measuring Principle

A possible way of measuring Auger spectra is using a LEED instrument in the Auger mode. This setup can be roughly divided into an electron gun, a retarding field analyzer (RFA) and electronics that convert the RFA output into the final spectrum (see figure 2.6).

The electron gun provides the primary electrons which are emitted from a filament F. Whilst being accelerated towards the anode A, they are focused by a Wehnelt cylinder W. Behind the anode, the beam is further focused and
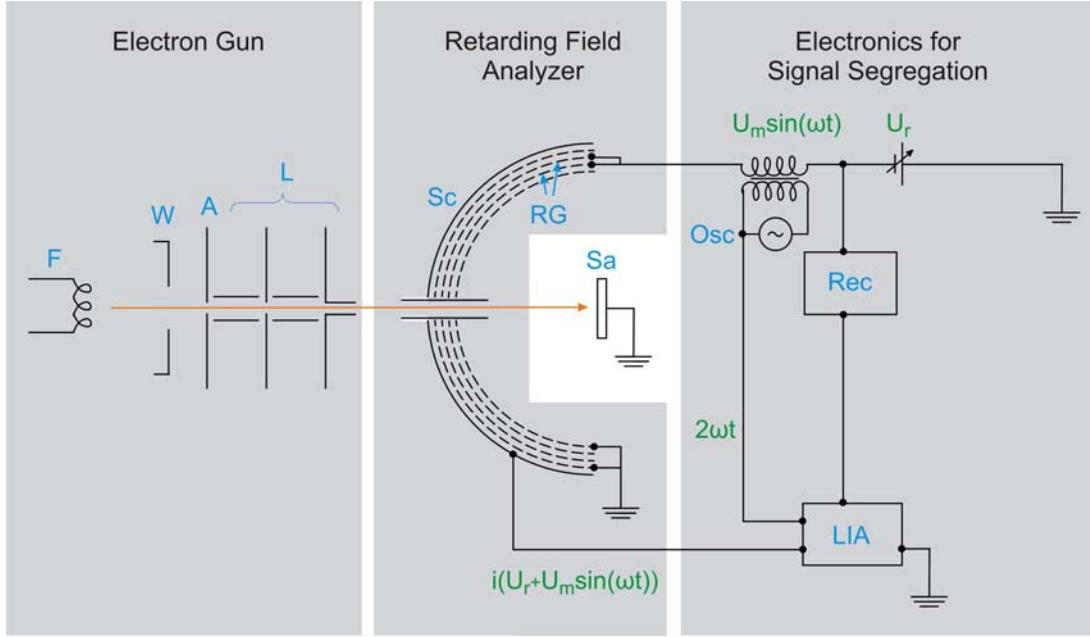
Figure 2.6.: Scematic auger setup: F = filament, W = Wehnelt cylinder, A= anode, L = electrostatic lens system, Sc = collector screen, RG = retarding grids, Sa = sample, Osc = Oscillator, LIA = lock‑in amplifier, Rec = recording instrument (computer)

collimated by a lens system L until it finally hits the grounded sample Sa and excites the core electrons.

The secondary electrons (elastically/inelastically scattered electrons and Auger electrons) are now separated with respect to their kinetic energy by the retarding field analyzer. The RFA consists of five concentric hemispheres (four grids and one collector screen) that are very close to each other. Coming from the sample, the electrons first have to pass the repeller grids RG. These are the two inner grids which are enclosed by two grounded grids. On the repeller grids a negative potential is applied such that they act as a highpass-filter which only allows for electrons of kinetic energy higher than the cutoff energy to pass and finally being collected at the Screen Sc. The current $i$ measured at the screen is therefore related to the density of states $N(E)$ in the following way:

$$i(U) \propto \int_{eU}^{\infty} N(E)dE$$

which means $di/dU \propto N(E)$ and therefore $d^2i/dU^2 \propto dN/dE$. The repelling potential is usually ramped linearly during one scan which is expressed by a linear term $U_r(t)$ and in addition modulated by a frequency $\omega$ with amplitude $U_m$ such that the resulting potential results as:

$$U(t) = U_r(t) + U_m sin(\omega t)$$

A Taylor expansion of $i$ looks as follows:

$$i(U_r + U_m sin(\omega t)) = i(U_r) + \frac{di(U_r)}{U_r}U_m sin(\omega t) + \frac{di(U_r)}{U_r^2}\frac{1}{2!}U_m^2 sin^2(\omega t)\dots$$

The signal coming from the screen is first preamplified before it is fed into the lock‑in amplifier (LIA) , locked at a frequency of $2\omega$ whose output is finally plotted versus $U_r$. Since the LIA is locked to $2\omega$, it will due to $sin^2(\omega t) = \frac{1}{2}[1-cos(2\omega t)]$ give an output which is proportional to $i''$ and therefore to $dN/dE$. It is also possible to lock the LIA to $\omega$ and get a direct spectrum proportional to $\frac{di(U_r)}{dU_r}$ and therefore also proportional to the density of states $N(E)$. However, Auger spectra are commonly plotted as $\frac{d^2 i(U_r)}{dU_r^2}[U_r]$ because the Auger features are always superimposed with a huge background due to inelastic processes (see figure 2.7).
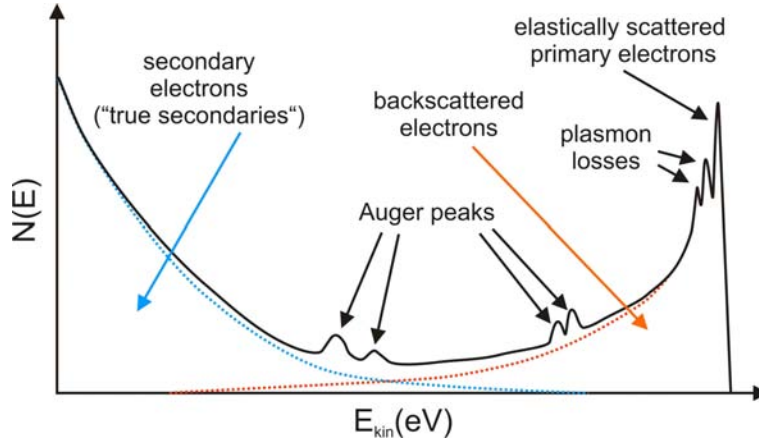


Figure 2.7.: Auger spectrum in the N(E) representation: The Auger features are relatively small in comparison to the huge backgroud being the superposition of inelastically scattered primary and secondary electrons. (Adapted from [22], p.12)

## 2.3. Ion Scattering Spectroscopy (ISS)

ISS or also called LEIS (low energy electron scattering) is a surface analysis technique which is based on measuring the energy loss of elastically scattered ions in binary collisions. An ion gun provides a beam of ions which are scattered at a target surface. The intensity of elastically scattered ions is then measured as a function of their final kinetic energy. Since the mass and and scattering angle of the detected ions are known, the masses of scattering surface atoms can be calculated from kinematics. The final kinetic energy of the projectile ($E$) is a function of the masses of projectile ($M_1$) and target atom ($M_2$), the scattering angle ($\theta$) and the initial kinetic energy of the projectile ($E_0$).

A scheme of a collision showing these parameters is depicted in figure 2.8. In an ISS measurement, the number of scattered ions is plotted as a function of
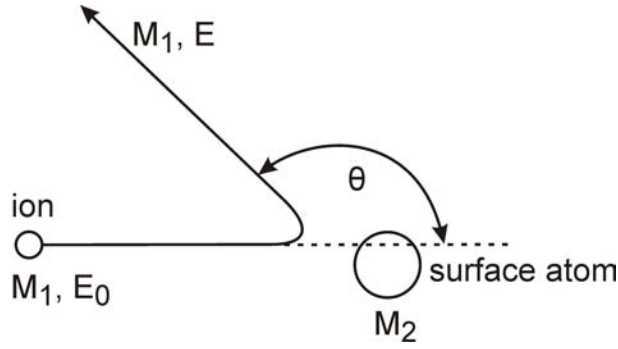
Figure 2.8.: Scheme of a collision and parameters which determine the kinematic factor.

normalized energy loss, i.e. $\frac{E}{E_0}$. This normalized energy loss is called kinematic factor and depends on the mass ratio $A = \frac{M_2}{M_1}$ and the scattering angle $\theta$ in the following way:

$$K(A, \theta) = E/E_0 = \left( \frac{\cos\theta \pm (A^2 - \sin^2\theta)^{\frac{1}{2}}}{1 + A} \right)^2 \qquad (2.2)$$

where the positive sign holds for $A > 1$ and the negative sign for $A < 1$. The kinematic factor as a function of scattering angle and mass ratio $A = \frac{M_2}{M_1}$ is plotted in figure 2.9. The graph illustrates, that the mass resolution is best for large scattering angles and small mass ratios, i.e. ISS has limitations in resolving heavy elements.
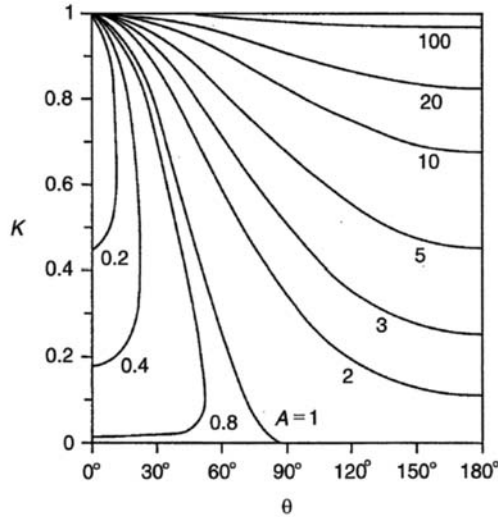


Figure 2.9.: Kinematic factor as a function of scattering angle and mass ratio $A = \frac{M_2}{M_1}$ (figure from [22]).

The energy of the scattered ion determines the interaction potential which it feels upon approaching the surface atoms. Whereas in Rutherford backscattering

(energy range: MeV) - the high energy counterpart of ISS (energy range: keV) - the interaction can be described by a Coulomb potential, in ISS, the effect of the electron shell has to be taken into account by modeling the interaction with a *screened* Coulomb potential.

The interaction time between ion and surface atom (order of magnitude: $10^{-15}$ - $10^{-16}$ s) is much shorter than lattice vibrations (order of magnitude: $10^{-13}$ s), such that in ISS, the ions 'see' a snapshot of a rigid lattice. ISS is extremely surface sensitive and probes basically only the outermost atomic layer of the surface. This is due to very efficient neutralization processes, whose probability increases drastically if the ion penetrates into deeper layers of the substrate. As a result, only ions scattered at the surface contribute to the signal. For noble gases with large ionization potentials (between 16 eV and 24 eV), which are frequently used for ISS, the Auger neutralization process is predominant, i.e. Auger electrons emitted from the surface neutralize the impinging ions.

ISS has been applied in studies of adsorbates and the surface composition of alloys and catalysts. It can also be used for structural analysis. Here, the concept of the shadow cones plays an important role. A shadow cone is formed by the envelope of initially parallel ion trajectories around and downstream a scattering target. Shadow cones for the case of low energy scattering can be calculated using a screened Coulomb potential [28]. The results agree quite well with experimental data. Using these concepts, interatomic spacings can be determined.

## 2.4. Low Energy Electron Diffraction (LEED)

### 2.4.1. Introduction

The first observation of diffraction patterns from backscattered electrons was reported in 1927 by Davisson and Germer [29]. In those days, this result corroborated the idea that also electrons do have properties of waves. The diffraction theory behind it is therefore applicable both to diffraction of particles as well as electromagnetic waves. So beside electron diffraction there are techniques, that rely on neutron or X-ray diffraction, for example. Each species interacts differently with matter and so the choice of method depends on the individual question that is to be answered. Nowadays, Low Energy Electron Diffraction (LEED) is a standard technique for UHV experimentalists to determine the long - range order of a surface. In most cases, a picture of the diffraction pattern is taken, but LEED offers also other ways to get more information about the structure of a surface. The dependence of the diffraction intensities on electron energy can be analyzed when so - called I(V) curves are measured. Also the profile of a diffraction spot can give further insight into the size of crystal domains, for example (Spot Profile Analysis (SPA) - LEED). An impressive example how temporally and spatially resolved LEED could even be used to investigate phase separation and self organization during a chemical reaction was demonstrated by Ertl and coworkers in 1985 [30].

Electrons interact strongly with matter compared to X-rays or neutrons. This means, that their inelastic mean free path is relatively short due to elastic or inelastic scattering etc. Their mean free path is also energy dependent. The minimum is at about $100\,\text{eV}$. In LEED, electrons of an energy of about $20\text{-}200\,\text{eV}$ are commonly used such that only electrons scattered within the upper $5\text{-}10\text{Å}$ contribute to the diffraction pattern. The strong interaction with matter leads on the one hand to high surface sensitivity, but it is also coupled to the disadvantage of a high rate of multiple scattering which demands complicated dynamical scattering models for structure analysis.

### 2.4.2. Theory

In general, the periodicity of a three-dimensional crystal can be described by one of the fundamental Bravais lattices whose periodicity is defined by a set of base vectors. From this set, the conditions for constructive interference and therefore diffraction can be determined. In principle, diffraction can occur only if the difference between the outgoing $(\vec{k_{out}})$ and incident wavevector $(\vec{k_{in}})$ equals a so-called reciprocal vector $\vec{G}$.

$$\vec{G} = \vec{k_{out}} - \vec{k_{in}}$$

The set of reciprocal vectors constitutes also a Bravais lattice, however, in reciprocal (or momentum) space. The reciprocal lattice is the Fourier transformation representation of the original - or direct - lattice. Each reciprocal vector (hkl) represents a set of parallel crystal planes (hkl) in direct space. Its length is inversely proportional to the interplanar distances of that family. It's direction is such that it points normal to the planes.

An illustration of the constraints for positive interference is the Ewald sphere (figure 2.10). Basically, a sphere with radius $\left|\vec{k_{in}}\right| = \left|\vec{k_{out}}\right|$ is constructed such that the incident wavevector $\vec{k_{in}}$ is pointing at the origin of the reciprocal lattice. All reciprocal points which now lie on the Ewald sphere represent vectors $\vec{k_{out}}$ for which the positive interference conditions are fulfilled.

With the length of the scattered wavevectors the radius of the Ewald sphere will change and reciprocal lattice points will disappear from or emerge on the sphere. This means that depending on length and incident angle of incoming waves, different families of lattice planes contribute to the appearance of diffraction spots.

To a first approximation, scattering at a surface can be modeled as scattering at a two dimensional lattice. In this case, the distance between reciprocal lattice points that lie on a line perpendicular to the direct lattice is infinitely small. Therefore, the reciprocal lattice consists basically of rods perpendicular to the surface. In this model, the diffraction conditions do not include constraints along the surface normal. An increase of the Ewald sphere leads merely to smaller angles between the diffraction maxima. For real samples, the peak intensities do depend on the primary energy due to multiple scattering at underlying planes.
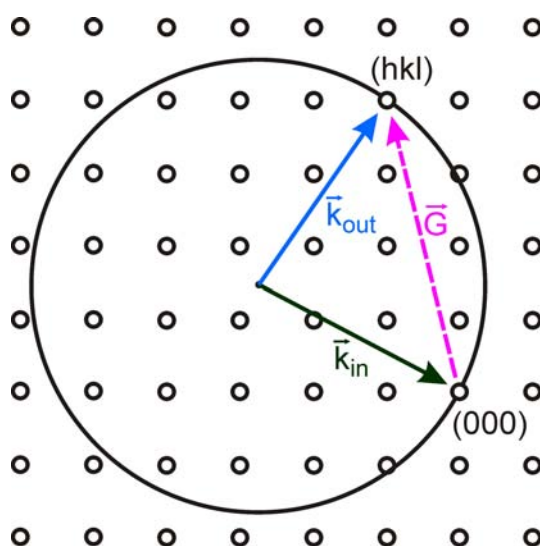
Figure 2.10.: The radius of the Ewald sphere depends on the length of the incoming wave $\vec{k_{in}}$ which points at the origin of the reciprocal lattice. Other lattice points which are located at the surface give rise to a diffraction peak from the set of parallel planes that they represent. (adapted from [31])

Real crystals are often much more complex than a Bravais lattice. Each point of the Bravais lattice represents a substructure in real crystals. This substructure is called atomic base. The relative positions of the different atoms that make up the base can be described by base vectors. That means, that the crystal lattice can be described more realistically by a convolution of delta functions distributed in a Bravais lattice array and the atomic base. The Fourier transform $FT$ of such a convolution equals - according to the convolution theorem - the product of the Fourier transforms of the Bravais lattice $f(x)$ and the base $g(x)$ ([32]).

$$FT(f(x) \otimes g(x)) = FT(f(x)) \cdot FT(g(x))$$

A diffraction pattern of a real crystal will therefore be a product of two functions. The principal diffraction spots originate from $FT(f(x)))$, but their intensities are modulated by $FT(g(x))$. $g(x)$ is a complex function called structure factor ($F$). For each diffraction spot, only the total intensity can be measured which is proportional to $|F(hkl)|^2$. The phase information is lost. For X-ray diffraction, it is possible to overcome this problem and to determine the atomic structure of the sample. This is possible because X-rays don't interact strongly with matter and multiple diffraction effects can be neglected. This is not true, however, for LEED. The incoming electrons are often scattered several times so many possible paths have to be taken into account for structure determination. The variation of intensities vs. electron energy can be modeled using multiple scattering approaches. However, modeling of such $I(E)$ spectra is very difficult and therefore not widely applied. However, from the simple LEED image, information about size, shape and symmetry of the unit cell can be derived.

### 2.4.3. Setup

For this work, the optics that were used for Auger measurements were also used for LEED (see figure 2.6). The electron gun works the same way, just the primary energy used for LEED is about 20 - 200 eV in contrast to 2 keV used for Auger measurements. For LEED, no ramp is applied at the retarding grids, but a constant repelling voltage to reduce the background. The fluorescent screen is used to visualize the modulation of diffraction intensities. For a high fluorescence output, the electrons are accelerated with an energy of several keV onto the screen.

## 2.5. Temperature Programmed Desorption (TPD)

### 2.5.1. Introduction

To understand heterogeneous catalytic processes, it is indispensable to obtain information about the interaction between the reactants and the surface. A very useful tool for obtaining such information is a method called temperature programmed desorption (TPD). Sometimes, it is also referred to as thermal desorption spectroscopy (TDS). This method involves the dynamic measurement of molecules desorbing from a surface by a mass spectrometer whilst the sample is being heated up at a constant heating rate.

It requires that the sample can be heated according to a well-defined temperature ramp. This is achieved by feeding the temperature reading from the thermocouple to a programmable feedback circuit. The feedback circuit in turn, controls the heating of the sample which might be resistive heating or heating by electron bombardment. The sample is usually exposed to a defined dose of particular gases at low temperature. The cone of a mass spectrometer is then placed in front of the sample as close as possible without having electrical contact. The mass spectrometer records all masses of interest in the course of the temperature ramp. A crucial factor for a precise measurement is the pumping speed. In an ideal machine, where it is infinitely high, readsorption can be neglected. For finite pumping speeds, besides desorption, readsorption occurs and changes the measured desorption trace.

### 2.5.2. Information

For 'simple' surfaces, i.e. periodic, homogeneous and flat surfaces, TPD is a method which can give relatively straightforward access to kinetic and thermodynamic information. When several desorption features are observed in one scan, for example, it can be deduced that there are several non-identical adsorption sites. Since the peak areas are in a first approximation proportional to the amount of desorbed species, also assumptions about the relative occupation of the different sites can be made. The occupation of sites depending on coverage gives information about preferential adsorption. If one can assume that the gas

completely desorbs, the saturation coverage and fractional coverages can be determined. However, one has to be aware that further desorption features might be above the maximum heating temperature or that sometimes species decompose irreversibly. Decomposition products like carbon, for example, might form much more stable deposits compared to the original molecule. TPD can also be extended to the observation of reactions taking place at the surface. When educts are codosed, the catalytic activity of a sample can be evaluated by monitoring the evolution of possible products. Another aspect of catalyst characterization by TPD is the area quantification of metal nanoparticles. The signal-surface area relation of a particular metal can be calibrated using a single crystal. When this metal is then deposited dispersively onto a support the particle size can be estimated from the desorption signal. This is a rough approximation, of course, which requires several assumptions, like the absence of SMSI, roughly equal density of adsorption sites at different facets etc. But in cases, where no other structural method like STM (scanning tunneling microscopy) is available, TPD can help to get an idea.

### 2.5.3. Theory

Apart from the analysis of peak areas, TPD can also be used to derive kinetic and thermodynamic parameters. This analysis is not trivial even for 'simple' surfaces and often assumptions and simplifications have to be applied to reduce the number of parameters. For complex surfaces like those of industrial catalysts, the number of parameters is much higher. Diffusion in pores, amorphous and inhomogeneous surfaces etc. come into play. For these systems, there is still no comprehensive theoretical model.

Kinetic models for reversible chemical reactions express the evolution of a product in terms of the decrease of educts over time. The exponential factor of the educt concentration in the rate equation determines the order of the reaction. The relative rate of desorption can be equally expressed as the change of coverage per unit time:

$$r_d = -\frac{d\theta}{dt} = k_{des}\theta^n \tag{2.3}$$

with

| | |
|---|---|
| $r_d$ | rate of desorption |
| $k_{des}$ | reaction constant for desorption |
| $\theta$ | coverage in monolayers |
| $t$ | time |
| $n$ | order of desorption |

When the rate constant $k_{des}$ is described by the Arrhenius equation

$$k_{des} = \nu E \left( -\frac{E_{des}(\theta)}{RT} \right) \tag{2.4}$$

with

| | |
|---|---|
| $\nu$ | pre-exponential factor of desorption |
| $E_{des}$ | activation energy of desorption |
| $R$ | gas constant |
| $T$ | temperature |

we end up with an equation referred to as the Polanyi-Wigner model [33]:

$$r_d = -\frac{d\theta}{dt} = \nu(\theta)\theta^n exp\left( -\frac{E_{des}(\theta)}{RT} \right) \tag{2.5}$$

Because of the interaction of adsorbates, $\nu$ and $E_{des}$ are dependent on coverage.

The order of desorption leads to characteristic desorption patterns that can be explained by the molecular mechanisms (see figure 2.11). Ag on Ru(0001), for example, shows zeroth-order desorption. Ag forms islands on Ru(0001) that are in equilibrium with a '2D gas' of Ag atoms migrating on the Ru. The potential of these 2D gas atoms is basically independent on $\theta$ as long as there are still islands since the 'gas pressure' stays constant. Therefore, the desorption shows a characteristic leading edge when the desorption peak is growing upon increased coverage. Below $0.5\,ML$, CO/Rh(111) desorption is a first order process. Here, the interaction between CO molecules can be neglected. The amount of desorption is proportional to $\theta$. $N_2$ desorbs in a second-order kinetic from Rh(100). Nitrogen atoms diffuse freely on the surface. When two nitrogen atoms meet, they can form $N_2$ which desorbs spontaneously.

Of course, apart from this qualitative understanding of the desorption order, one would like to extract other parameters of the Polanyi-Wigner equation from the data. There are several methods to do so. Some of the most prominent are the Redhead analysis, the complete analysis and the leading edge analysis.

The Redhead analysis [38] is relatively easy, but also based on assumptions which are sometimes questionable. It starts off by solving the Polanyi - Wigner equation for the temperature $T_p$ where the desorption rate is at maximum. When $n = 1$, and $\nu$ is estimated being a fixed value (usually about $10^{13}s^{-1}$, $E_{des}$ can be approximated as being

$$E_{des} = RT_p \left[ \ln\left( \frac{\nu T_p}{\beta} \right) - 3.46 \right] \tag{2.6}$$

where $T_p$ is the temperature where the desorption rate is at maximum and $\beta$ is the heating rate. So the $E_d$ can be estimated from one single spectrum just by determining $T_p$. However, because of the approximations, the results are often not satisfying. The reaction order has to be known. Furthermore, it is assumed that both $E_d$ and $\nu$ are independent of the coverage.
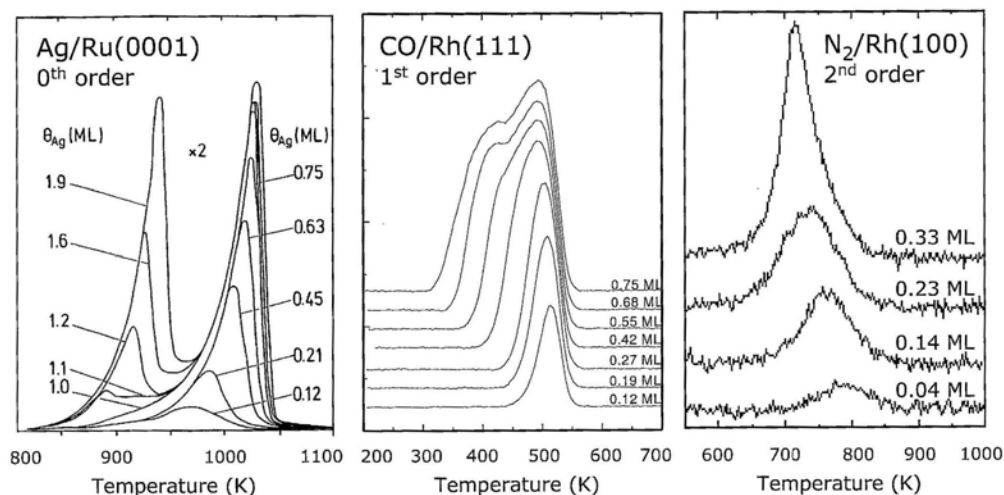
Figure 2.11.: Different orders of desorption. Left: zeroth-order desorption [34] of Ag.Middle: first-order desorption up to $0.5\,\text{ML}$ CO [35]. Right: second-order desorption[36] of $N_2$. Picture taken from [37]

Another, more demanding approach is the complete analysis that has been proposed by David King [33]. Here, several TPD spectra with different initial coverages are measured. A particular coverage $\theta$ is determined which is reached at different temperatures for the different initial coverages. The Polanyi-Wigner equation can be rewritten as:

$$ ln\left[-\frac{d\theta}{dt}\right] = \ln\nu(\theta) + n\ln\theta - \frac{E_{des}}{RT} \tag{2.7}$$

So since $\theta$ is a fixed and known value, by plotting $ln\left[-\frac{d\theta}{dt}\right]$ against $\frac{1}{T}$, $E_{des}$ can be derived from the slope. From the intercept $ln\left[\nu(\theta)\right] + n \cdot ln\left[\theta\right]$, $\nu$ can be determined if $n$ is known and vice versa.

Another approach based on a low number of assumptions is the leading edge analysis [39]. Here, it is approximated that at the very beginning of a desorption feature, the coverage is basically constant, namely the initial coverage $\theta_i$.

$$ r_d = \nu(\theta_i)\theta_i^n\, exp\left(-\frac{E_{des}(\theta_i)}{RT}\right) \tag{2.8}$$

For each known initial coverage, the first data points can be used for an Arrhenius plot. From the slope $E_d(\theta_i)$ can be determined. The intercept is equal to $\ln\nu(\theta_i) + n\ln\theta_i$. However, a high quality of data is required for the complete analysis to be applicable.

## 2.6. Infrared Reflection Absorption Spectroscopy (IRAS)

Vibrational spectroscopies are very versatile tools for chemical analysis. For the study of molecular adsorbates on flat metallic surfaces, reflectance‐based

infrared spectroscopy (IRAS) is extremely powerful. Its advantage lies in the high resolution, sensitivity and applicability on a wide range of samples. In contrast to a number of other surface science techniques, it does not require conductive samples. Furthermore, if it is applied in the polarization - modulation mode (PM - IRAS) it can be used to study samples at realistic conditions at high pressures while disentangling tiny adsorbate contributions from a large gas phase signals.

In a very simple picture, a diatomic molecule with an electric dipole will align in a permanent electric field. In an alternating electric field, as it is the case for an electromagnetic wave, this molecule will start to rotate and at the same time the bond length will start to oscillate due to the opposite forces acting on both atoms. Therefore, in general, IR absorption spectra show not isolated vibrational bands, but rotational - vibrational bands. The collective excitation of rotations and vibrations are subject to quantum mechanical selection rules.

In a more general case of more complex molecules it can be stated that a precondition for the excitation of vibrations by infrared light is not the existence of a permanent dipole moment in the first place, but that during excitation the dynamic dipole moment is altered.

An important measure for the ability of a molecule to absorb IR light, is its transition dipole moment $M_{i \to f}$ which can be deduced from perturbation theory.

$$M_{i \to f} = \langle \Psi_i | \vec{\mu} | \Psi_f \rangle \tag{2.9}$$

where $\vec{\mu}$ is the dipole moment operator and $\Psi_i$ and $\Psi_f$ the wavefunctions of the initial and the final state. The probability of a transition is, according to Fermi's golden rule proportional to the square of $M_{i \to f}$. The transition dipole moment is a vector, such that it is also determined how light has to be polarized in order to excite a transition.

Nowadays, FT - IR spectrometers which have a number of advantages compared to dispersive IR spectrometers used in former times, have become a standard tool. The heart of these systems is the Interferometer. It splits an incident collimated infrared beam by a beam splitter into two beams which are recombined after a variable path difference $\delta$ has been introduced by reflecting one of the beams at a movable, the other at a static mirror. Finally, the intensity $I$, which is modulated due to interference, is measured at the detector. For a monochromatic light source of frequency $\nu$, passing through an ideal optical setup, a cosine modulated function is detected ($I(\delta) \propto cos(2\pi\delta\nu)$). In a polychromatic case, this expression turns into an integral:

$$I(\delta) = \int_{-\infty}^{+\infty} S(\nu) cos(2\pi\delta\nu) d\nu \tag{2.10}$$

The Fourier transform of the intensity therefore is the distribution of amplitudes as a function of frequency, i.e. the spectrum of the light source.

$$S(\nu) = \int_{-\infty}^{+\infty} I(\delta) cos(2\pi\delta\nu) d\delta \qquad (2.11)$$

In principle, however, this spectrum also includes absorption features from the optical setup and is influenced by the detector response. Therefore, in order to only extract the absorption contribution from the sample, the spectra are usually background corrected by a reference spectrum measured in the same configuration without the molecule of interest.

In the Fourier transform, the integral over path difference $\delta$ from $-\infty$ to $+\infty$ is calculated. In the real spectrometer, however, the path of the movable mirror is limited. This corresponds to a multiplication of the real interferogram with a rectangular function $rect(\delta)$. The convolution theorem states that the Fourier transform of a product of two functions can be expressed as the convolution of the individual Fourier transforms of both functions. Therefore, the measured interferogram is convoluted with a sinc function $sinc(\delta)$, which is the Fourier transform of $rect(\delta)$.

Further corrections are commonly applied, like the introduction of a wavelength dependent phase factor to correct for the asymmetry of real interferograms and the multiplication with an apodization function to suppress artefacts.

The FTIR technique is also used in IRAS. An important aspect in the reflection mode is the polarization of the incident light. The polarization is defined as parallel (p) or perpendicular (s) with respect to the plane of incidence (figure 2.12, a)). Greenler calulated the phase shifts which s and p radiation undergoes at the point of contact with the surface (figure 2.12, b)). It becomes clear, that for incident angles between zero and 90 degrees, the s polarized light phase shifted by almost - 180°, such that the resulting vector sum of incoming and outgoing wave at the point of surface contact is basically zero. The p polarized light, on the other hand, is shifted much less and the shift gets close to zero at grazing incidence. Therefore, the vector sum of the incoming and outgoing wave is almost twice the amplitude of the wave. The parallel polarized light is therefore the only component which can excite adsorbates at the surface and the efficience of excititation is maximized using a configuration of grazing incidence. The fact that in IRAS, the incident beam must have a parallel polarized component, is called the *surface selection rule.*

For adsorbates on metal surfaces, this selection rule holds for an additional reason. The metal interacts with the dipole moments of the molecules. In the metal, image dipoles are created which are oriented opposite to the molecule dipole moments, such that dipole components parallel to the surface are screened by the metal. Therefore, only vibrations with a dynamic dipole component perpendicular to the surface, can be excited. This effect is called *metal surface selection rule.*

There are further effects which influence specifically the absorption of adsorbates such that the resulting spectra can differ significantly from corresponding gas phase spectra. For example, if a molecule is adsorbed with high coverage on a surface, the dynamic dipoles of the molecules can interact which leads to
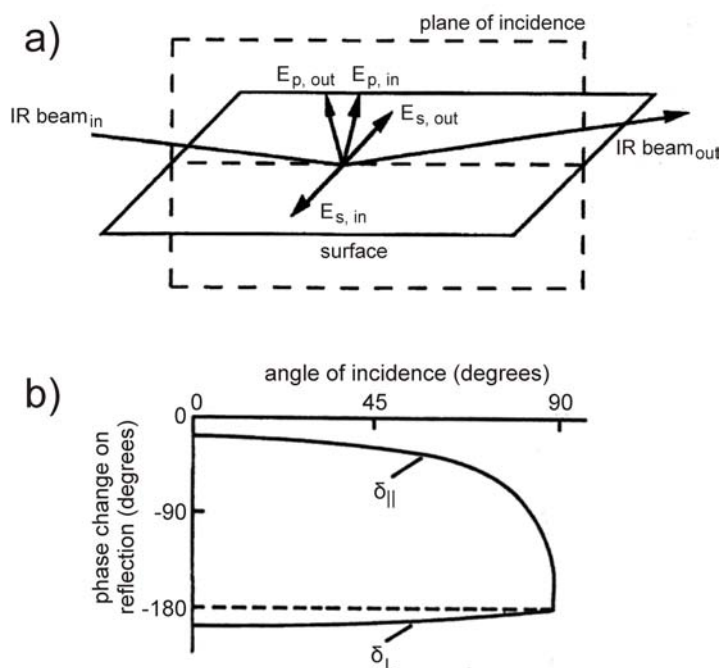
Figure 2.12.: Illustration of the surface selection rule. a) Definition of s and p
polarized light. b) Calculated phase shift of light polarized parallel
(p) and perpendicular (s) to the plane of incidence reflected at a
metal surface (after Greenler [40, 41]). Figure adapted from [22]

a blue shift in absorption. The absorption can also be affected by the interaction between subatrate and adsorbate as it has been described in case of CO on metals by the Blyholder model [42]. This model states, that CO adsorbs via a donation‑backdonation mechanism. It donates charge to the metal from its bonding $5\,\sigma$ orbital and the metal, on the other hand, donates charge from its d band to the antibonding $2\,\pi^*$ orbital of CO. As a result, the C‑O bond is weakened which leads to a red shift of the absorption compared to the gas phase signal.

The surface selection rule imposes some restrictions to the experiment. However, advantage can be taken of it in case of measurements at elevated pressures, where the gas phase signal can be separated from the contribution of adsorbates. This can be achieved by recording a spectrum using p and s polarized light in parallel. Molecules in the gas phase will absorb p and s polarized light equally. Adsorbates, on the other hand, are only excited by the p polarized light. Therefore, the difference spectrum of both components represents the absorption of molecules adsorbed on the surface. Experimentally, such measurements are realized by putting a photoelastic modulator (PM) behind a monochromator into the path of the incident beam. This technique is called Polarization‑Modulation IRAS (PM‑IRAS). The photoelastic modulator can alter the polarization of the incident beam with high frequency (74 kHz in our setup). The detector signal now contains a low frequency component (due to the movement of the movable

mirror) and a high frequency component due to the modulation by the PM. From the low frequency modulation, the average spectrum of p and s contributions can be obtained. From the high frequency component, the differential reflectance spectrum ($\Delta R/R$) can be obtained which can be corrected such that the desired difference spectrum is obtained.

## 2.7. Experimental Setup

### 2.7.1. Setup for Studies on Ultrathin Films
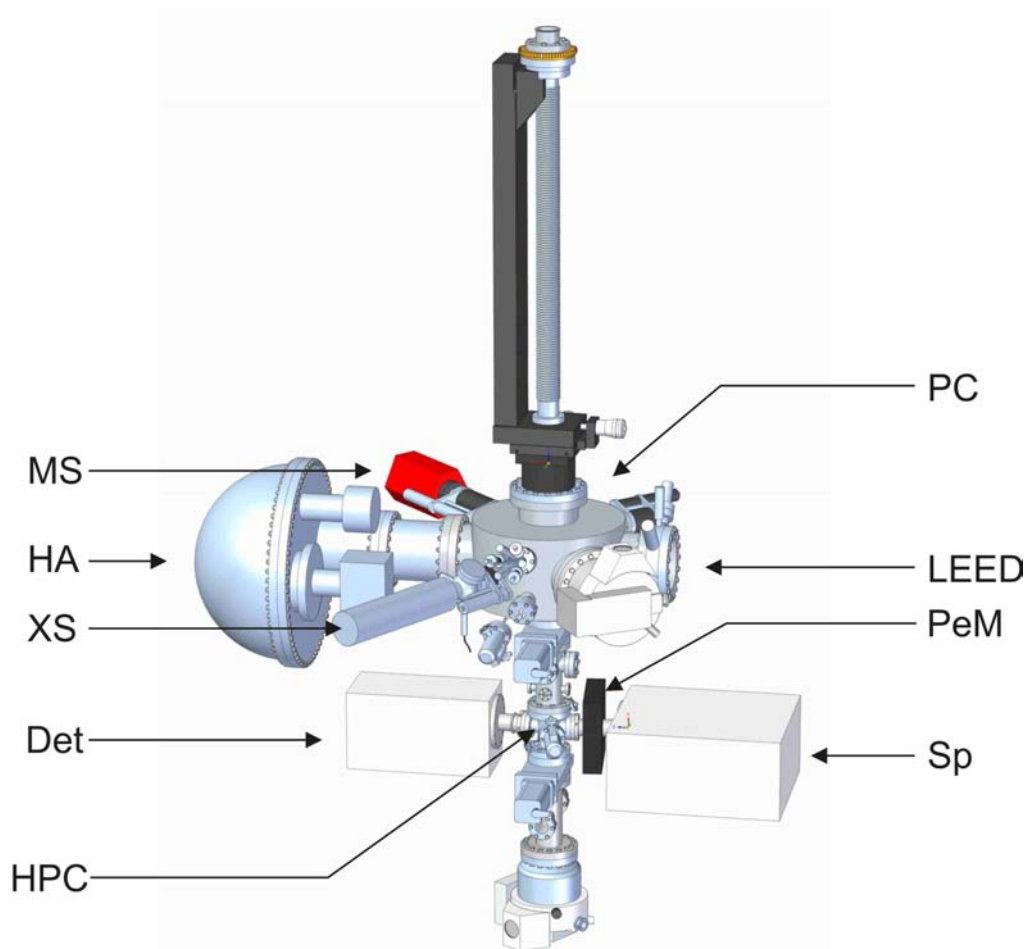


Figure 2.13.: PM-IRAS setup:MS = mass-spectrometer, HA = hemispherical analyzer, XS = X-ray source, Det = detector, HPC = high pressure cell, PC = preparation chamber, LEED = LEED optics, PEM = photoelastic modulator, Sp = spectrometer

The investigations on ultrathin films presented in chapters 3 and 4 were implemented in the IRAS setup described here. An exception are the STM studies

of FeO(111)/Pt(111) [1]. For these experiments, the samples were prepared in the Setup I and investigated by the Wandelt type STM described in the next section 2.7.2.
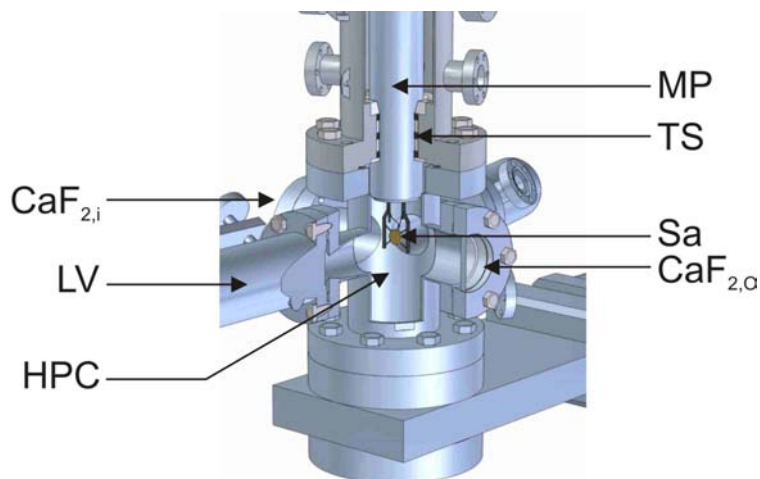


Figure 2.14.: PM-IRAS high pressure cell: $CaF_2, i$ = $CaF_2$ window for incoming IR beam from spectrometer, LV = leak valve for gas inlet, HPC = high pressure cell, MP = manipulator, TS = Teflon sealing, Sa = sample, $CaF_2, o$ = $CaF_2$ window for outgoing IR beam towards detector

A scheme of the complete IRAS setup is shown in figure 2.13. This system comprises a preparation chamber equipped with standard tools for crystal cleaning and thin oxide film growth. It is furthermore equipped with an X-ray gun (Specs) and a hemispherical analyzer (Phiobos 150, Specs) for XPS analysis as well as LEED optics and a quadrupole mass spectrometer. At the bottom, the preparation chamber is connected by a gate valve to a small UHV/high pressure cell. Here, IR studies can be performed in the IRAS or PM IRAS mode. The IR beam can enter and leave the cell via two $CaF_2$ windows. The infrared beam coming from the Bruker spectrometer (type IFS66v) enters the chamber via the first window, is directed towards the sample surface where it is reflected and finally leaves the chamber via the second window until it finally hits the $LN_2$-cooled MCT (Mercury-Cadmium-Telluride) detector. The setup is suitable for IRAS studies in UHV and at elevated pressures up to ambient pressure. A more detailed view of the UHV/high pressure cell is shown in figure 2.14, which illustrates how the manipulator seals the preparation chamber from the high pressure cell if the sample is in the position for IRAS measurements.

In this setup, the sample is mechanically fixed by a Tantalum wire loop which is directly spot-welded on two Molybdenum rods of the manipulator. In contrast to the other setups of our group, here, the sample is permanently fixed to the manipulator, i.e. it cannot be removed from the chamber without venting. The manipulator allows for liquid nitrogen cooling and the sample is heated

---

[1]performed by Huifeng Wang

resistively. For all experiments of the present thesis, a K-type (Alumel (95% Nickel, 2% Manganese, 2% Aluminum) - Chromel (90% Nickel, 10%Chromium)) thermocouple was attached to the sample to record the temperature which was cotrolled by a PID controller.

### 2.7.2. Setup for Liquid Phase Deposition Experiments
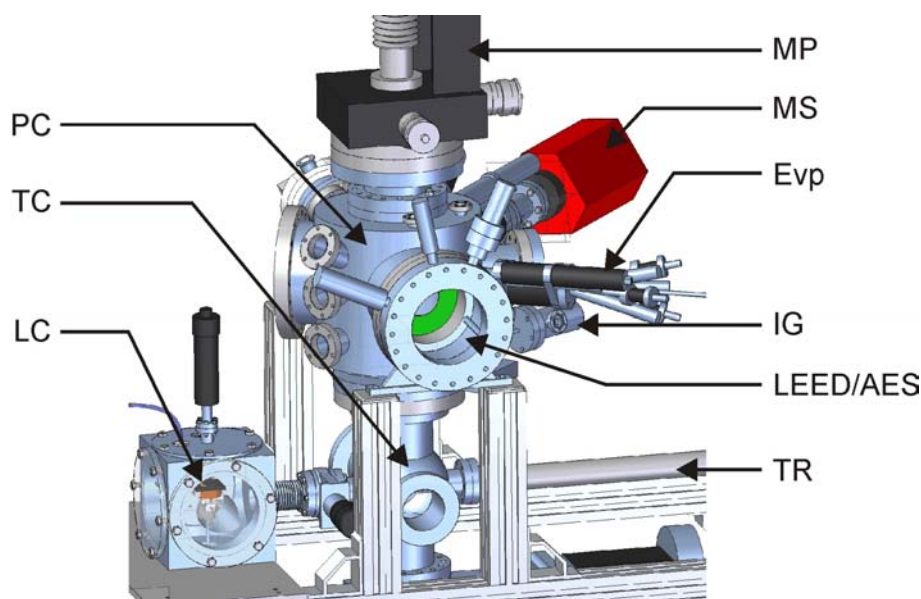


Figure 2.15.: LPD Setup I: PC = preparation chamber, TC = transfer chamber, LC = liquid chamber, MP = manipulator, MS = mass spectrometer, Evp = evaporator, IG = ion gun, LEED/AES = LEED/AES optics, TR = transfer rod

Two separate UHV systems were used for liquid phase deposition experiments. As in case of the IRAS setup, both systems are equipped with standard tools for crystal cleaning and thin oxide film deposition. A transfer chamber/load lock system allows for fast sample transfer between both chambers. The samples are mounted on a modified Omicron molybdenum sample plate. They are heated by putting a positive bias on the crystal and bombarding it with electrons emitted from a filament at the back side. The manipulators allow for cooling by air flow or liquid nitrogen. For the results presented in this work, the temperature was measure with a K-type thermocouple and controlled by a PID controller. The Ag(001) crystal used here had a diameter of 10 mm and a thickness of 6 mm.

Setup I is depicted in figure 2.15. It houses LEED optics with the option to perform AES measurements as well. A differentially pumped quadrupole mass spectrometer (Pfeiffer) for TPD measurements is available as well. Here, the Ag(001) crystal was cleaned and MgO films were deposited and characterized by LEED, AES and TPD.

Setup II was primarily used for XPS analysis. Amongst other things, it is equipped with a dual Al/Mg X‑ray source (Specs) and a hemispherical analyzer (Phoibos 150, Specs).

STM measurements were performed in a Wandelt type electrochemical STM [43] which is operated in ambient air or water.

# Chapter 3.

# FeO – An Ultrathin Metal Oxide Film in Ambient Conditions

## 3.1. Introduction

### 3.1.1. General Aspects about FeO

Iron oxides are widely used materials in industrial catalysis. They play a crucial role in major reactions like, for example, ammonia synthesis [44], the Fischer-Tropsch process [45], dehydrogenation [46] and the abatement of NO [47, 48]. They are commonly used as support for dispersed metal catalysts, but recently, ultrathin FeO layers supported on metals have attracted increasing attention as well. FeO layers have been grown on various supports such as Pd(111) [49], Pt(111) [50], Pt(100) [51], Ru(0001) [52], Ag(111) [53], Au(111) [54] and Mo (100) [55]. Most prominent, however, is the FeO(111)/Pt(111) system, since it shows enhanced activity towards CO oxidation which is due to a phase transition induced in oxygen-rich conditions [1]. So far, this process has been observed in surface science experiments applying pressures in the mbar range, but it might also be of importance for applied catalysts exposed to realistic conditions. The particular objective of this work was to study the behaviour of FeO(111)/Pt(111) in ambient conditions, i.e. its structural and chemical stability and catalytic activity at high pressures and in the presence of water vapor.

The (111) facet of a Pt crystal is of hexagonal symmetry with a lattice constant of 2.77Å. The symmetry of the FeO(111) lattice is identical, however, it has a lattice constant of 3.1 Å and therefore a lattice mismatch of 12% with respect to Pt(111). The FeO(111) film grows in a bilayer fashion on Pt(111), with the Fe layer in contact with the Pt surface, and the top oxygen layer terminating the film. If these two layers were isolated from the metal, the FeO(111) surface would be polar and therefore unstable due to the resulting net dipole moment. In the presence of a metal support, however, the bilayer relaxes, i.e. the oxyen-iron distance (and therefore the dipole moment) is reduced. Furthermore, the metal underneath compensates for the remaining dipole of the ultrathin layer. As a result, FeO(111)/Pt(111) is relatively inert.

In the FeO(111)/Pt(111) system, the FeO lattice is rotated by 1.3° with respect to the [$\bar{1}$00] direction of the Pt(111) lattice. Therefore, a rhombic Moiré pattern with a periodicity of about 26 Å can be observed in STM images. In 2D reciprocal space, the Moiré structure leads to hexagonal rosettes around each Pt spot which can straightforwardly be observed by LEED [50]. The large size of the Moiré unit cell is challenging for theoretical modeling. Even though calculations on the

Moiré cell as a whole have been performed [56], commonly, three regions within in the cell are investigated separately. These regions are distinguished by the registries of iron and oxygen atoms with respect to the underlying Pt: 1.) 'Fe on-top' - where Fe atoms sit on top of Pt atoms and O atoms sit on hollow sites, 2.) 'Fe fcc' - where both Fe and O atoms sit on hollow sites and 3.) 'Fe hcp' - where Fe atoms sit on hollow sites and O atoms sit on top of the Pt atoms (figure 3.1).
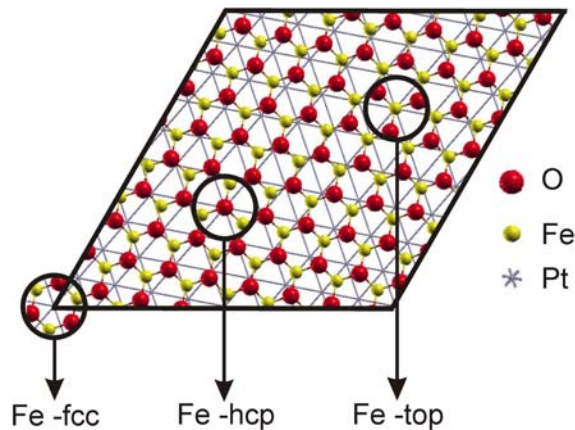


Figure 3.1.: 'Fe on-top', 'Fe fcc' and 'Fe hcp' regions in the Moiré unit cell of FeO(111)/Pt(111). The intersections between the gray lines represent the position of the surface Pt(111) atoms (adapted from [57]).

The behaviour of FeO in oxygen atmosphere has been investigated in detail [58]. In oxygen rich conditions, the FeO layer undergoes a phase transition to $FeO_x$ with $1 < x < 2$. The degree of oxygen enrichment depends on the oxygen chemical potential. Furthermore, it is not homogeneous across the Moiré unit cell. According to DFT calculations, the bilayer $\leftrightarrow$ trilayer transition is thermodynamically most favorable in the 'Fe hcp' region. In comparison to FeO, where the Fe layer is adjacent to the Pt(111) surface and the atop oxygen layer terminates the film, the oxygen rich $FeO_2$ phase forms a trilayer sandwich structure with the Fe atoms enclosed by two layers of oxygen. STM measurements showed, that an ordered array of islands is formed upon heating an FeO film at $470\,K$ in $20\,mbar$ oxygen atmosphere (figure 3.2, a)). These islands can be attributed to an $FeO_2$ phase. The lattice constant of the island pattern is slightly larger (3%) than the one of the FeO Moiré unit cell. This is due to the slightly reduced lattice constant of the $FeO_x$ phase compared to FeO. Each $FeO_2$ island exhibits a regular corrugation which is much higher than the corrugation of the FeO phase. From combined experimental and theoretical studies, it was concluded that this corrugation reflects a buckled film structure. Every third Fe atom relaxes out of the interjacent Fe layer almost up to the position of the upper oxygen layer (figure 3.2, b)). The buckled structure has a $(\sqrt{3} \times \sqrt{3})R30°$ structure with respect to the FeO lattice.
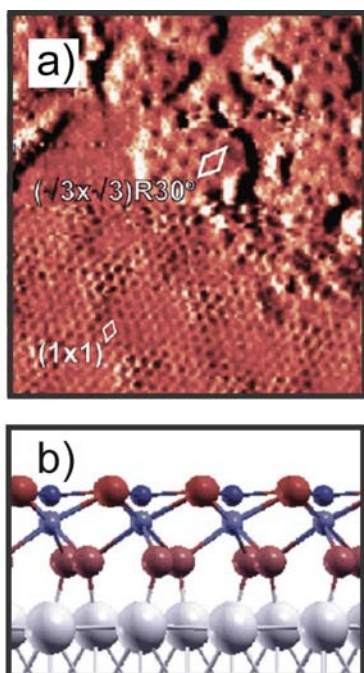
Figure 3.2.: a) STM image showing $FeO_x$ (top, $1 < x < 2$) and FeO (bottom) phases adjoining each other. b) Buckled structure of $FeO_2$ obtained from DFT calculations. Red spheres represent O atoms; blue spheres Fe atoms. (figures from [58])

### 3.1.2. A Model System for SMSI Effects

In 1978, the concept of Strong Metal Support Interaction (SMSI) was introduced, when the chemisorption properties of $TiO_2$ supported group VIII metals were observed to drastically change after high-temperature annealing [59]. Later on, SMSI was also found for metals supported on the oxides of Niobium, Vanadium and Manganese [60]. Whether or not SMSI occurs, depends on the specific combination of materials. Alloy formation or encapsulation of metal particles by an oxide layer are most commonly observed SMSI states. Initially, it was believed that ultrathin oxide layers mainly deactivate the catalytically active metal. In many cases, a strong decrease of CO and $H_2$ adsorption was observed. It has not previously been considered, that the ultrathin oxide overlayers, which cover the metal particles, might be the active species themselves.

More recent research has focused on the intrinsic catalytic properties of ultrathin metal oxide films supported on metals. Both native oxide films, derived from oxidizing the first few surface layers of a single crystal, as well as mixed systems - where the support is a different metal than the metal in the oxide film - have been investigated [21]. The CO oxidation over superficially oxidized Ru, for example, has been widely investigated. In a LEEM (low energy electron microscopy) study, it was found that $RuO_2(110)$ and a disordered, trilayerlike -O-Ru-OO surface coexist [61]. Even though oxygen has a higher activity towards Ru than Rh, Pt and Pd, surface oxide formation was also found for the latter metals [62, 63, 64, 65].

The type of mixed system, which is best understood nowadays, is FeO(111)/Pt(111). It is well established that FeO on Pt(111) single crystals is highly active towards CO oxidation at elevated pressures in the mbar range. The activity of these 1 ML thin films is higher than that of pure Pt(111) or $Fe_3O_4$

substrates [1]. Furthermore, it has been found that Pt particles supported on $Fe_3O_4$ also experience SMSI such that they are covered by single layers of FeO [66]. These systems also show enhanced activity towards CO oxidation in comparison to systems with pristine Pt particles [67]. This shows that the results from extended FeO films on single crystals are comparable to the behaviour of FeO on (111) facets of supported Pt particles. FeO/Pt(111) is therefore a suitable model for investigating the promotional effect of ultrathin oxide films covering metals and it is important to understand the mechanism behind.

The catalytic results reported so far have been obtained with samples that were transferred under clean conditions from UHV environment into dedicated high-pressure cells. In any realistic environment, for example, air, the surface will, however, also be exposed to traces of water. The interaction between water and oxides is of general importance in a number of fields such as geochemistry, material science, corrosion etc.. For catalysis, it plays an important role as well since water is always present in ambient air to some extent, which leads to facile surface hydroxylation of many oxides as soon as they are exposed to air. Furthermore, in applied catalysis, many preparation procedures involve contact between the support and a precursor solution. A crucial parameter for catalytic applications is, therefore, if the catalytically active phase, that is, the O-Fe-O trilayer, is also stable under more realistic conditions.

In our group, we investigated this question be means of IRAS , STM (scanning tunneling microscopy) and XPS. We studied the structure and chemical composition of a UHV-prepared FeO(111)/Pt(111) surface after exposure to water vapor and water vapor/oxygen mixtures as well as to ambient air and water. The catalytic activity of samples exposed to water vapor and oxygen was tested as well as their interaction with small amounts of deposited gold.

## 3.2. Experimental

### 3.2.1. Setups

The experiments were performed in the STM and in the IRAS setup (see section 2.7). Infrared spectra were acquired either in the standard IRAS mode or with the polarization modulation (PM-IRAS) technique using a photoelastic modulator (Hinds Instruments). Typically, 1000 scans were accumulated for one spectrum. All photoelectron spectra reported here are referenced to the Fermi energy of Pt(111) and were taken at an electron takeoff angle of 60° with the analyzer pass energy set to 20 eV.

### 3.2.2. Crystal Cleaning

One cleaning cycle of a Pt(111) single crystal consists of several steps:

- ○ sputtering   1 hour at 300 K; $3\,\mu A$ in $4 \cdot 10^{-6}$ mbar Ar
- ○ annealing   5 minutes at 1200 K in UHV
- ○ oxidation   10 minutes at 600 K in $1 \cdot 10^{-6}$ mbar $O_2$
- ○ annealing   5 minutes at 1200 K in UHV

By means of LEED, the crystalline order of the clean surface was checked. The hexagonal pattern of the Pt(111) surface leads to a simple hexagonal pattern in reciprocal space and therefore in the LEED image (see figure 3.3).



Figure 3.3.: LEED pattern of a clean Pt(111) surface.

### 3.2.3. FeO Film Preparation

Next, the FeO film was prepared by PVD:

- ○ deposition:   1 ML Fe at 300 K; deposition rate $\sim 1$ ML per minute
- ○ oxidation:   2 minutes at 1000 K in $1 \cdot 10^{-6}$ mbar $O_2$
  cooling down in $O_2$ to 500 K; cooling down to 300 K in UHV

Since both Pt(111) and FeO(111) have hexagonal symmetry, the symmetry of the LEED image stays the same. However, due to the Moiré pattern hexagonal rosettes appear around each Pt spot (see figure 3.4).
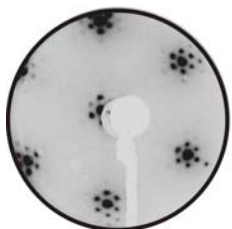


Figure 3.4.: LEED image of a pristine FeO(111)/Pt(111) film.

To check whether the film is closed, TPD measurements were performed (figure 3.5). The sample was exposed to a saturation dose of 10 L CO. The integral of the CO desorption signal was compared to a reference CO desorption signal from clean Pt(111). Pt(111) has a characteristic CO desorption feature at about 400 K. FeO, on the other hand, is inert towards CO adsorption. Therefore, the total amount of CO desorption from an FeO film is inversely related to the FeO coverage.
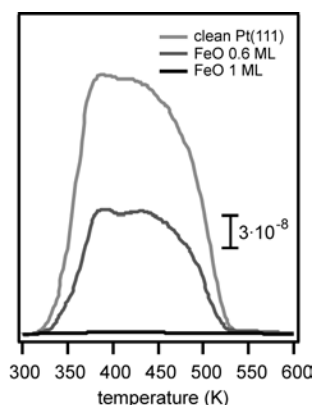
Figure 3.5.: CO TPD spectra from clean Pt(111) and FeO/Pt(111) samples with 0.6 and 1.0 ML coverage (dose: 10 L CO, heating rate: $3\,\mathrm{K\cdot sec^{-1}}$).

The quality of the film was also checked by XPS (figure 3.6). Besides CO desorption, the O 1s XP peak area is another indicator for the amount of FeO deposited. Furthermore, contaminations can be detected. In all stages of the FeO growth, the Pt substrate is detected exclusively in the metallic state with the Pt $4f_{7/2}$ binding energy located at around 71.1 eV [68]. For the pristine FeO film, the O 1s binding energy is found at 529.6 eV which lies within the range of values reported for FeO (around 529.8 eV [69]). The Fe 2p region overlaps with the Pt 4s peak, which is located at around 724 eV [70]. Here, we found a Fe $2p_{3/2}$ binding energy of about 710 eV. This corresponds well to values for FeO (Fe II) which have been reported around 709.9 eV [71]. However, a clear distinction to $Fe_3O_4$ (Fe(II) + 2 Fe(III)), whose bulk Fe $2p_{3/2}$ binding energy is located at about 710.4 eV [72], is rather difficult. From $Fe_2O_3$ (Fe(III)), on the other hand ($\sim$ 711 eV [73]), it can be distinguished more easily.
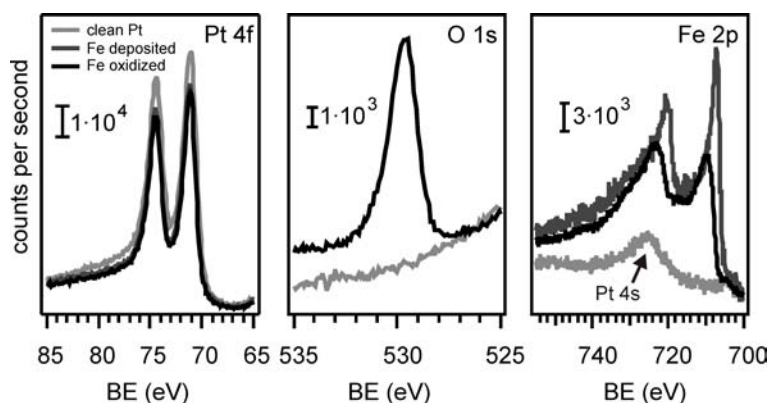


Figure 3.6.: FeO film preparation checked by XPS (Pd 4f, O 1s and Fe 2p regions).

### 3.2.4. Water Dosing

Water and water/oxygen exposure was carried out in the high-pressure cell, such that the background pressure in the preparation chamber remained unaffected. Millipore water was used which had been cleaned by several freezing-pumpout cycles in order to remove residual gases dissolved in the water. The gas pressure was monitored with a baratron capacitance manometer (MKS instruments) with

a sensitivity of $10^{-2}$ - $1000$ mbar. Unless stated otherwise, water was dosed with the ion gauge turned off because it turned out that the ion gauge filament affects the hydroxylation of the film.

## 3.3. Results and Discussion

### 3.3.1. Stability and Hydroxylation of FeO in Ambient Conditions
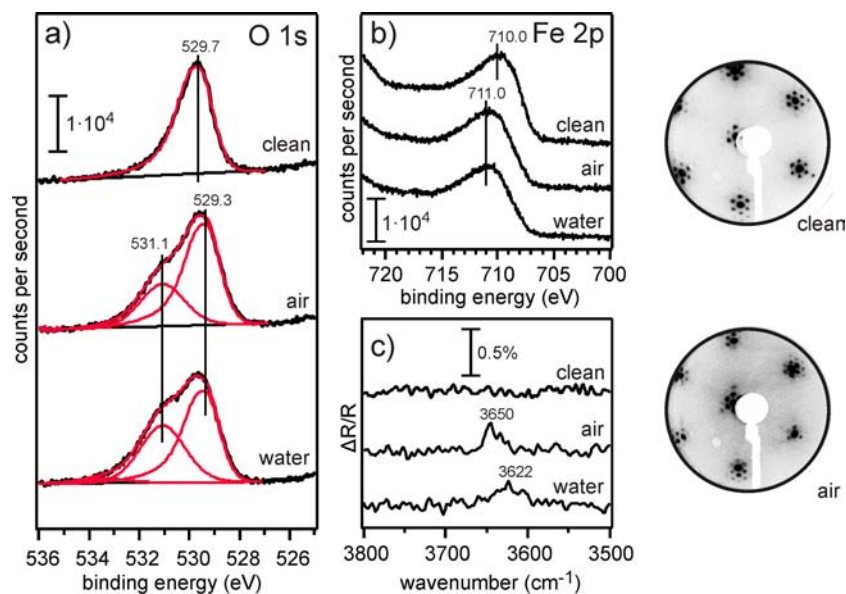


Figure 3.7.: FeO/Pt(111) exposed to air and water. a) XP O 1s region of pristine FeO and after air and water exposure. b) XP Fe 2p region of pristine film and after exposure to water. c) background corrected PM - IRA spectra after air and water exposure Right: LEED pattern of pristine film and after exposure to air. [1]

The exposure of FeO/Pt(111) to air and liquid water clearly induces strong changes in the film. The O 1s XP spectra reveal an enrichment and change of the nature of oxygen (figure 3.7, a)). In pristine FeO, only one oxygen species can be detected which has an O 1s binding energy of 529.7 eV and represents the terminating oxygen layer as described in section 3.1.1. Upon exposure to air, this 529.7 eV peak shifts by (-0.4) eV to lower binding energy. At the same time, an additional peak of 531.1 eV O 1s binding energy appears, which can be assigned to OH groups [74, 75]. The hydroxyl shoulder evolves *in addition* to the main peak such that the total peak area is increased and an enrichment of the film with oxygen can be deduced. Exposure to liquid water after air exposure induces no significant new modifications, but the degree of hydroxylation is slightly increased. The Fe $2p_{3/2}$ peak position shifts by $+1$ eV from 710.0 eV to 711.0 eV upon exposure to air and also upon subsequent exposure to liquid water. This indicates that iron is in a higher oxidation state (figure 3.7 b)) after such treatment. Whereas a Fe $2p_{3/2}$ binding energy around 710 eV is assigned

to $Fe^{+2}$ in the literature, a value around $711.0\,eV$ indicates $Fe^{+3}$ [76, 77]. The XPS results are corroborated by IRAS measurements (figure 3.7 c)). In contrast to the pristine sample, the spectra of samples exposed to air and subsequently to liquid water show absorption features in the range of $3620$ - $3650\,cm^{-1}$, which can be assigned to hydroxyl species. In the LEED pattern after air exposure, however, no changes are detected as compared to the pristine sample (figure 3.7, right). Apparently, the film maintains its long range order despite of the chemical changes.
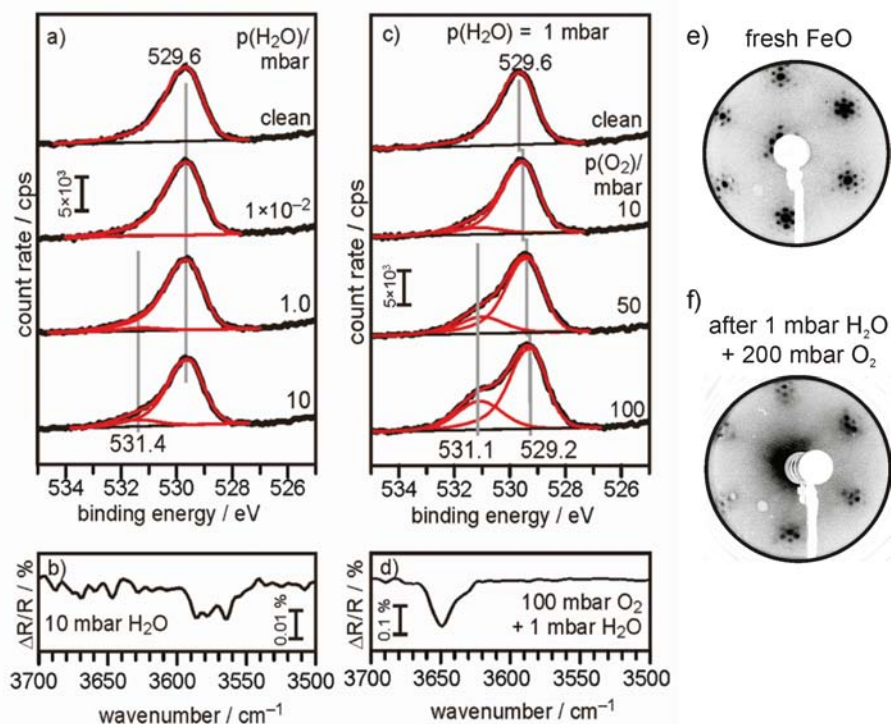


Figure 3.8.: a) XP O 1s region of an FeO(111)/Pt(111) film in the pristine state and after exposure to water at different pressures. b) IRA spectrum after obtained after interaction of $10\,mbar\ H_2O$ with FeO(111). c) O 1s XP spectra of clean FeO(111)/Pt(111) and after $H_2O/O_2$ coadsorption for $3\,min$ at room temperature. The $H_2O$ pressure was fixed at $1\,mbar$. d) IRA spectrum obtained after coadsorption of $1\,mbar$ $H_2O$ and $100\,mbar\ O_2$. Right: LEED patterns of an FeO sample before and after exposure to $1\,mbar\ H_2O$ + $200\,mbar\ O_2$.

The significant oxygen enrichment and hydroxyl formation on the FeO film in ambient conditions raises the central question: What is the driving force for this transformation? Oxygen constitutes a significant fraction of ambient air with a partial pressure of roughly $200\,mbar$. Water vapor is also always present in air in varying amounts. Is water alone sufficient to hydroxylate the film? We tried to answer this question by exposing the FeO film to increasing pressures of water vapor ($10^{-2}$ - $10\,mbar$) under clean conditions up to a pressure, which corresponds

to a typical water vapor pressure in ambient air (10 mbar corresponds to 50 % relative humidity).

No significant modifications were detectable in the O 1s region of the photo-electron spectra (figure 3.8, a)) up to a 1 mbar water vapor dose. Only after exposure to 10 mbar, a small hydroxyl shoulder appears. In contrast to expo-sure to ambient air, no significant shift of the O 1s main peak is apparent. The infrared spectrum shows an absorption peak at around $3570\,\mathrm{cm}^{-1}$ (figure 3.8, b)). Both methods indicate that a hydroxyl species was formed after exposure to 10 mbar water vapor. Comparison of IRAS and XPS data indicates, however, that this OH species is of different nature compared to those observed upon exposure to ambient conditions. Obviously, water alone is not responsible for the changes observed after exposure to air. Therefore, water was codosed with oxygen in order to model air exposure more closely.

Codosing 1 mbar of water vapor with varying amounts of oxygen results in a film showing properties very similar to those exposed to air and liquid water (figure 3.8, c) and d)). Again, the film is enriched with oxygen as evidenced by the corresponding O 1s spectrum. The OH absorption in the infrared region is located at around $3650\,\mathrm{cm}^{-1}$. A hydroxyl shoulder grows in addition to the main $O^{2-}$ peak which is again shifted to lower binding energy (529.2 eV). Starting the codosing experiments at low oxygen pressures, the OH:$O^{2-}$ peak area ratio increases continuously. At 100 mbar $O_2$, however, the ratio reaches a value close to the one observed upon exposure to air (see figure 3.7 a)). Upon a further increase of the oxygen pressure up to 200 mbar in the codosing experiment , we observed no further change of the ratio. Therefore, the water vapor/oxygen experiment seems to mimic quite well ambient exposure. Decisive conditions which drive the transition seem to be fulfilled. The degree of transformation seems to be related to the oxygen pressure.

As explained in section 3.1.1, FeO can be transformed from a bilayer to an $FeO_2$ trilayer by heating in oxygen atmosphere. After this transformation, an enrichment of oxygen is observed [78]. In the trilayer, Fe is embedded in a sandwich-like manner between two layers of oxygen. Since for our samples, oxygen is also the driving force for the transition, and we also observe a total enrichment of oxygen and a parallel oxidation of iron, we postulate the formation of a trilayer in ambient conditions as well. However, since in our case we observe a large degree of hydroxylation, we expect the terminating layer to consist of OH groups instead of oxygen atoms (see figure 3.9).
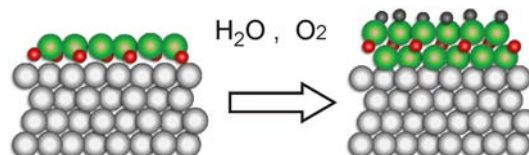


Figure 3.9.: Transition from an FeO bilayer to an FeO(OH) trilayer phase (light gray = Pt, green = O, red = Fe, dark gray = H).

Interestingly, the degree of hydroxylation of pristine FeO turned out to be influenced by the ion gauge (figure 3.10). When water is dosed without a glowing filament, OH groups only show up after a 10 mbar dose as explained previously (figure 3.8, a)). After water exposure, the O 1s main peak shifts by - 0.4 eV to lower binding energy. However, if the ion gauge is turned on during the dose, OH groups can be detected already after a $1 \cdot 10^{-4}$ mbar $H_2O$ dose exhibiting an O 1s binding energy of 531.5 eV (figure 3.10, a)). They are formed at the expense of lattice oxygen which is obvious since the lattice oxygen peak of the O 1s XPS region is diminished when the hydroxyl shoulder is evolved. The main O 1s peak does not shift - it remains chemically unchanged.
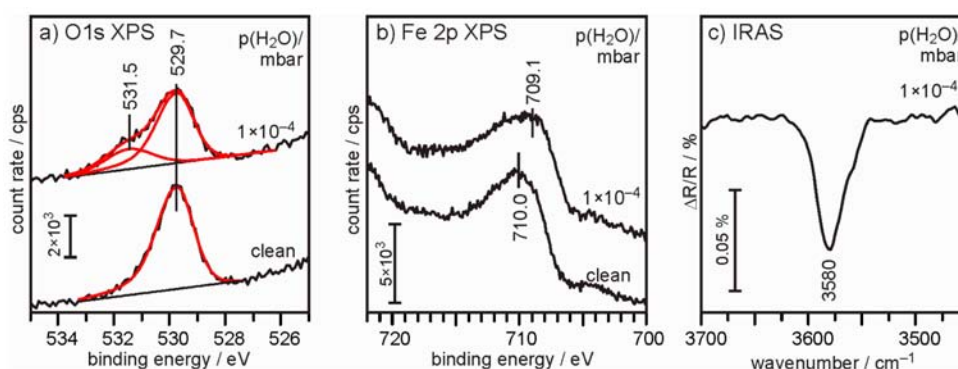


Figure 3.10.: a) O 1s and b) Fe 2p XP spectra of clean FeO(111)/Pt(111) and of the same sample after exposure to $1 \cdot 10^{-4}$ mbar $H_2O$ with the filament switched on during exposure. c) IRA spectrum obtained after water exposure showing the formation of hydroxyls exhibiting a stretching frequency of 3580 cm$^{-1}$.

The corresponding IRA spectrum shows an absorption peak around 3580 cm$^{-1}$ (figure 3.10, c)). In contrast, hydroxyl groups obtained by exposing the sample to air or upon codosing oxygen and water with the ion gauge turned off have different properties. They absorb infrared light at about 3650 cm$^{-1}$ and have XP O 1s binding energies around 531.1 eV (figure 3.7 a) and figure 3.8, c)). These results clearly show that two different OH species were formed. The ion gauge filament is considered to create reactive hydrogen radicals which reduce the FeO film partially. This is also reflected by the shift of the Fe 2p peak by - 0.9 eV to lower binding energy (figure 3.10, b)). Iron reduction and hydroxylation on an FeO(111)/Pt(111) film by atomic hydrogen created by a gas cracker has also previously been observed by Knudsen *et al.* [79]. In contrast, upon exposure to ambient conditions, Fe is oxidized such that the Fe 2p peak shifts by + 1.0 eV to higher binding energy reflecting the FeO(OH) trilayer formation (figure 3.7, b).

In summary, the film, which is formed in the presence of a hot filament at $1 \cdot 10^{-4}$ mbar $H_2O$, is hydroxylated, but not enriched with oxygen. It exhibits OH vibrations at different frequencies compared to FeO(OH) and iron is more reduced compared to FeO. These results would be consistent with the formation of a hydroxylated bilayer, i. e. FeOH (see figure 3.11). The fact that this structure

is formed at such low water pressures can be explained by the presence of highly reactive hydrogen radicals, which are created at the hot filament.

Going back to figure 3.8 a), it becomes evident that a sample showing the same characteristics can be obtained upon exposure of FeO to water vapor without the hot filament, however, at much higher water pressures (10 mbar $H_2O$). Therefore, without the ion gauge, FeOH formation is probably driven by $H_2O$ dissociation at defects.
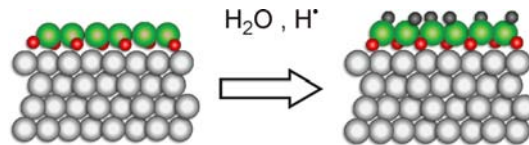


Figure 3.11.: Scheme of the postulated formation of FeOH (light gray = Pt, green = O, red = Fe, dark gray = H).

DTF calculations performed by Pachhioni and coworkers have shed light on understanding the processes which we observed experimentally. The large dimensions of the Moiré unit cell with a lattice constant of about 26 Å prohibited the treatment of the unit cell as whole. Instead, the three characteristic regions Fe on-top, Fe fcc and Fe hcp were investigated separately with respect to thermodynamics. A pseudomorphic model has been applied, where for each of the regions, a superposition of a $(\sqrt{3} \times \sqrt{3})$R 30° FeO(111) and $2 \times 2$ Pt(111) were used. The lattices of both were aligned and subsequently, the Pt lattice was expanded in order to meet the lattice parameter of the FeO [80] ($a_{FeO}$=3.1Å; $a_{Pt}$=2.77 Å). This system has been found to satisfactory describe experimental results obtained in earlier studies. The formation of an $FeO_2$ trilayer as a function of oxygen chemical potential turned out to be energetically most favourable in the Fe hcp region [58]. Therefore, further calculations were concentrated on this region. The role of the chemical potential of water $\mu_{H_2O}$ and oxygen $\mu_{O_2}$ and their interplay is summarized in the phase diagram shown in figure 3.12. As the red line depicts, oxygen enrichment, which goes along with a bilayer $\leftrightarrow$ trilayer transition, is almost exclusively determined by $\mu_{O_2}$. The degree of hydroxylation, on the other hand, is related to $\mu_{H_2O}$. It follows that both the bilayer and the trilayer can be free of OH groups, or partially or completely terminated with OH groups - depending on $\mu_{H_2O}$ [81].

This result is consistent with our experimental observations. By dosing water vapor only, we did not obtain a trilayer structure, but at high water pressure, which corresponds to a top left position in the phase diagram, a hydroxylated FeOH bilayer was formed (see figure 3.8 a)). At elevated oxygen pressure (bottom right position in the phase diagram), in contrast, an FeO $\rightarrow$ $FeO_2$ phase transition is observed [78]. Upon codosing water and oxygen at elevated pressures, which corresponds to a a position in the top right of the phase diagram, we obtained a hydroxylated FeO(OH) trilayer (see figure 3.8 b)) as a result of the combined effect of water ($\rightarrow$ hydroxylation) and oxygen ($\rightarrow$ trilayer formation).
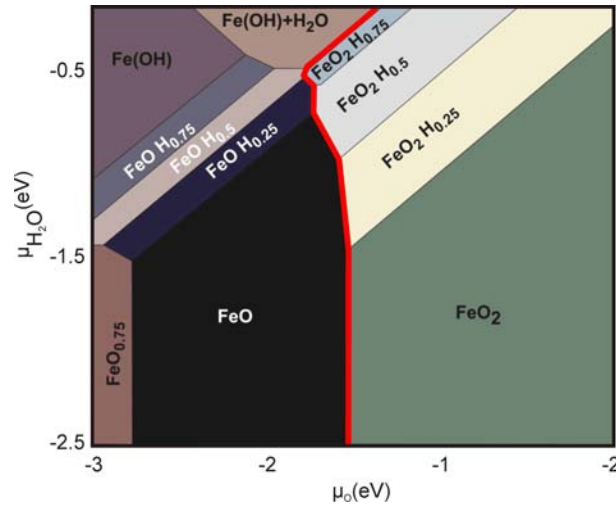
Figure 3.12.: The phase diagram calulcated by Pacchioni and coworkers visualizes the phases FeO transforms into as a function of water and oxygen chemical potentials. The red line illustrates the bilayer $\leftrightarrow$ trilayer transition [81].

Important insight on the structure of the transformed films can be obtained by STM imaging. Figure 3.13 shows $60\,\mathrm{nm} \times 60\,\mathrm{nm}$ images of FeO/Pt(111) measured in air (figure 3.13, left), water (figure 3.13, center) and in air after exposure to water (figure 3.13, right). The pattern observed in air resembles the Moiré pattern which was observed on $FeO_2$ trilayer films in UHV [58]. However, since here we have a hydroxylated film, the regularly arranged protrusions which represent $FeO_2$ islands in the hcp regions of the UHV samples are in our case most likely corresponding regions which have an FeO(OH) structure. Interestingly, the film seems to partially loose structural order when placed into water (the hexagonal symmetry is, however sustained which is shown by the FFT inset), but after water removal (figure 3.13, right) it becomes clear that the structural integrity has been maintained.
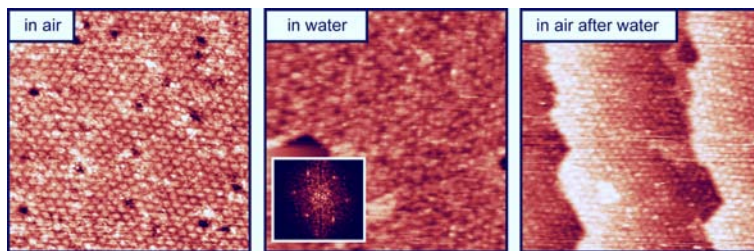


Figure 3.13.: STM images ($60\,\mathrm{nm} \times 60\,\mathrm{nm}$) of FeO(111)/Pt(111) measured in air (left), in water (center) and in air after exposure to water (right). (With courtesy of H. Wang)

### 3.3.2. Au Adsorption on FeO(OH)

Hydroxylation of an oxide support can significantly alter the nucleation behaviour and chemical state of metal nanoparticles. For Au on MgO/Ag(001) thin films, for example, this has been recently demonstrated by our group. By a combination of IRAS and XPS, it was found that Au became oxidized and was more stable towards thermal sintering on hydroxylated MgO films compared to pristine MgO films due to the formation strong Au‑O interfacial bonds [82]. This motivated us to investigate and compare the interaction of Au with FeO and FeO(OH). For these ultrathin films, the influence of the metal support is an additional factor which might affect the structure and chemical state of supported metal particles.
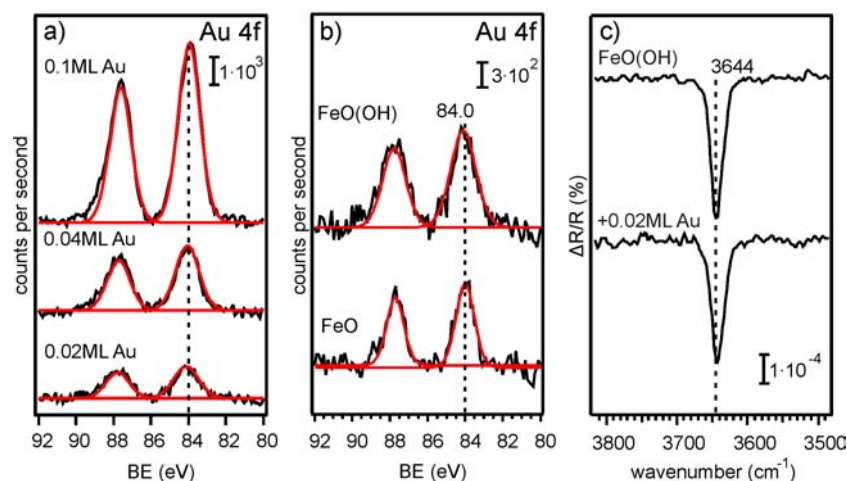


Figure 3.14.: a) XP Au 4f regions obtained after deposition of 0.02, 0.04 and 0.1 ML of Au on FeO(OH). b) XP Au 4f regions of 0.02 ML Au deposited on FeO(OH), $FeO_2$ and FeO. c) IRA spectra of an FeO(OH) sample before and after deposition of 0.02 ML of Au. In all experiments, Au was deposited at room temperature.

Metal adsorption studies on ultrathin FeO have been carried out using STM, STS (scanning tunneling spectroscopy), IRAS, EELS (electron energy loss spectroscopy), UPS and DFT. For Ag/FeO(111)/Mo(110) it was found that silver grows in a 3D mode already for coverages as low as 0.16 ML [83]. From an STM/STS/DFT study using extremely low coverages of Au (0.45‑0.75 Au atoms per Moiré unit cell of the oxide, which corresponds to less than 0.01 ML) at low temperatures (the STM was operated at 5 K), experimental evidence exists that on FeO(111)/Pt(111), Au adsorbs preferentially on top of oxygen atoms where it gets positively charged. It binds preferentially to the hcp domains where the surface dipole is particularly strong [57] such that self assembled arrays are formed [84]. In an FeO(111)/Pt(111) study applying IRAS, charged Au originating from very small clusters or even single atoms was found for low coverages at low tem-

peratures (90 K) whereas after sintering induced by annealing to 500 K, only metallic Au was detected [85].

In our study, we deposited submonolayer amounts of Au (0.02 ML, 0.04 ML and 0.1 ML) at room temperature on FeO(OH) samples (figure 3.14, a)). Furthermore, we compared by XPS the nucleation of 0.02 ML of Au on FeO(OH) to nucleation on FeO (figure 3.14, b)). In both cases, the Au 4f photoelectron spectra showed only one feature at 84.0 eV Au $4f_{7/2}$ binding energy which corresponds to metallic gold.

The infrared absorption of hydroxyl groups on FeO(OH) samples was investigated prior to and after deposition of 0.02 ML of Au (figure 3.14, c))). Neither did the absorption at $3644\,\mathrm{cm}^{-1}$ shift nor was its intensity diminished. This shows that the interaction between Au atoms and hydroxyl groups must be very weak or negligible.

In summary, we can conclude that at room temperature, for the coverages we used (0.02 - 0.1 ML), Au interacts only weakly with FeO and FeO(OH).

No charge transfer was observed nor did we detect any interaction between Au and the OH groups of FeO(OH). We cannot draw conclusions about whether or not preferential binding sites exist, but the absence of Au-OH interaction, the metallic character of Au even for smallest coverages and the knowledge that the trilayer regions in the Moiré cell form high protrusions in the electron density maps obtained from STM [58], make it seem likely that Au agglomerates in the non-hydroxylated 'valleys'.

### 3.3.3. Catalytic Activity of FeO(OH) towards CO Oxidation

The intrinsic catalytic activity of FeO in ambient conditions is another interesting aspect, since is has been shown that the $FeO_2$ trilayer is highly active towards CO oxidation [1]. It vastly outperforms the Pt(111) substrate and oxidizes CO via the Mars - van - Krevelen mechanism [86]. We checked the FeO(OH) film for reactivity by IRAS measurements in oxygen rich conditions, i.e. in a mixture of 10 mbar CO and 50 mbar $O_2$ which was balanced to 1 bar with He. There was no necessity to transform the pristine FeO to an FeO(OH) trilayer before the reaction. Residual water - which could not be avoided at a total pressure of 1 bar - and the high oxygen pressure were sufficient to transform the sample automatically (figure 3.16). The reaction was run at 450 K sample temperature for 80 minutes (figure 3.15).

We followed the reaction *in situ* in the high pressure IR cell by monitoring the gas phase absorptions of CO and $CO_2$ over time. After about 65 minutes, the CO in the reactor - whose volume is about $600\,\mathrm{cm}^3$ - was completely consumed and the $CO_2$ absorption reached a stationary plateau (figure 3.15, a), c) and d)). In contrast, the control experiment using a clean Pt(111) sample resulted in only minor changes of the initial gas concentrations after 80 minutes (figure 3.15, b) and d)). With the surface area of about $0.54\,\mathrm{cm}^2$, this leads to an approximated reaction rate for FeO(OH) of $4\cdot10^{16}$ molecules $\mathrm{sec}^{-1}\,\mathrm{cm}^{-2}$ whereas in the case of Pt(111), it can be approximated as $5\cdot10^{15}$ molecules $\mathrm{sec}^{-1}\,\mathrm{cm}^{-2}$. These results
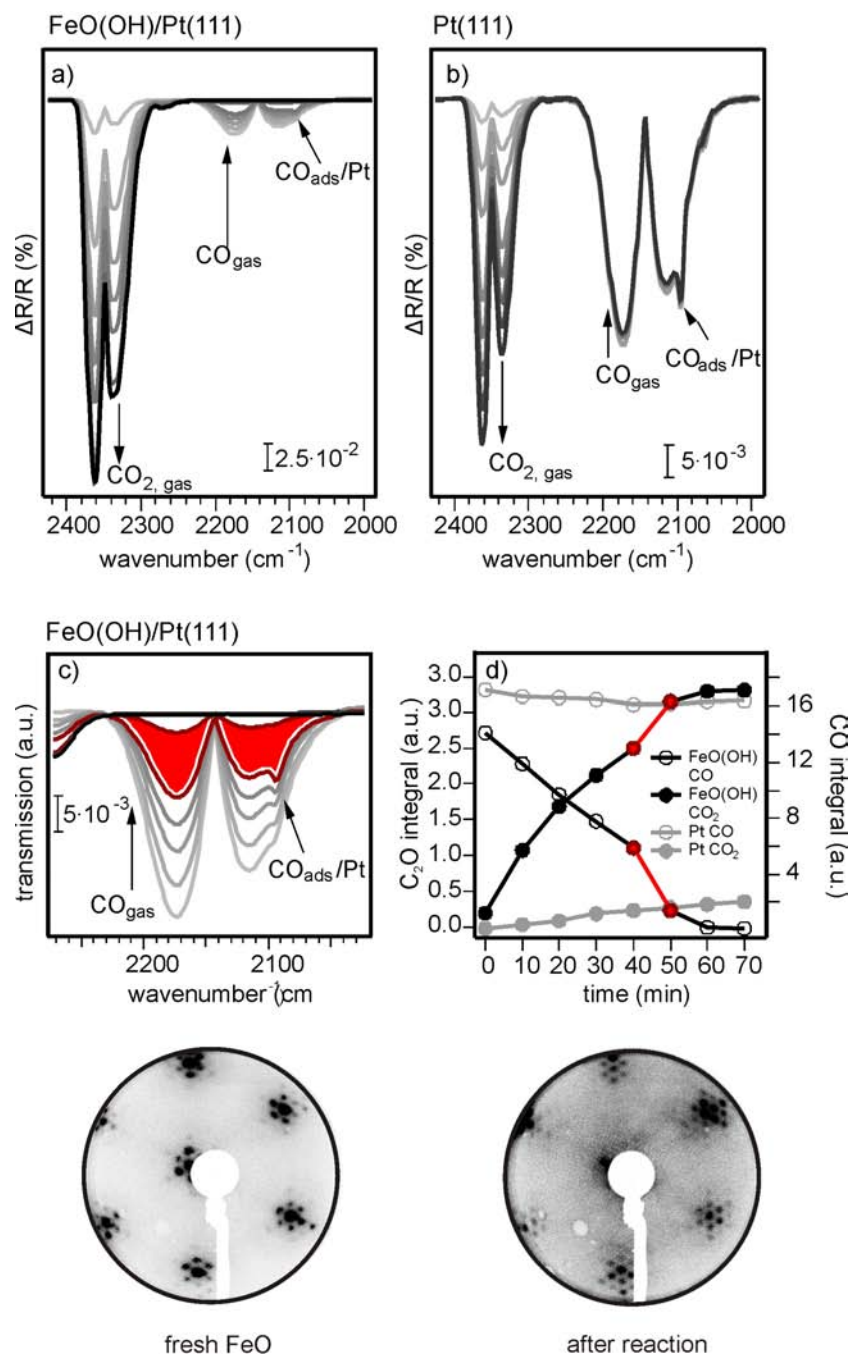
Figure 3.15.: Infrared spectra of the CO and $CO_2$ gas-phase spectral regions recorded during CO oxidation (10 mbar CO + 50 mbar $O_2$ balanced with He to 1 bar at 450 K for 80 min) over FeO(OH)/Pt(111) and Pt(111) (top and middle left). The spectra were recorded in intervals of 10 min. Middle right: Integrated intensities of the CO and $CO_2$ gas-phase IR signals as a function of reaction time. Bottom: LEED pattern before and after reaction.

clearly demonstrate, that not only $FeO_2/Pt(111)$ obtained in UHV conditions, but also the hydroxylated $FeO(OH)/Pt(111)$ trilayer, which is formed in ambient conditions, is highly active towards CO oxidation.
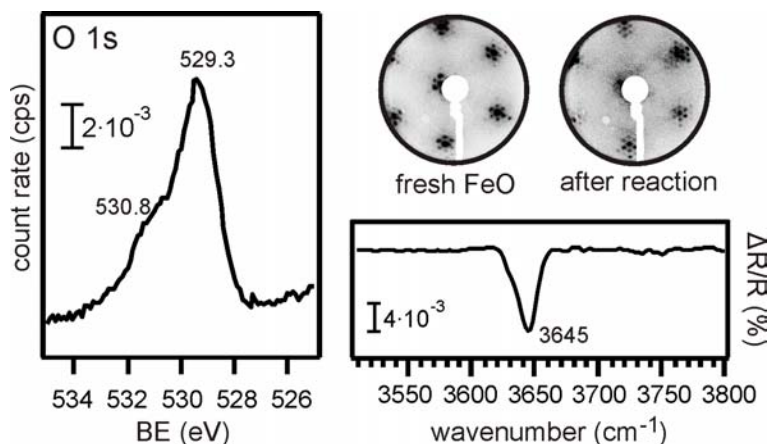


Figure 3.16.: Characterization of FeO before and after CO oxidation (10 mbar CO + 50 mbar $O_2$, balanced with He to 1 bar, 80 min at 450 K) by the XP O 1s region (top left) and LEED patterns (top right). Bottom: IRA spectrum after reaction.

A closer look at the IRAS spectra of figure 3.15, b) and c) reveals an interesting detail about the dewetting behaviour of FeO(OH). For the first 40 minutes, the FeO(OH) spectra exhibit a characteristic absorption peak at $2094\,cm^{-1}$ which is superposed on the gas phase CO absorption band (figure 3.15, c)). The same peak is found even stronger on the Pt(111) sample (figure 3.15, b)) where it remains present during the whole reaction period. It is due to CO adsorbed on the Pt(111) surface. Apparently, the FeO(OH) sample is partially dewetted at the beginning of the reaction when the CO concentration is still relatively high. The red data points in figure 3.15 d), whose difference correspond to the red area in 3.15 c), indicate a sudden increase in reactivity for the FeO(OH) sample. At this point, the CO/Pt(111) peak disappears in the spectra. The concurrence of both features is evidence for a rewetting of FeO(OH) at this moment. Here, the CO concentration has decreased sufficiently for the film to be stable again. The rewetting leads to a sudden jump in CO conversion.

In figure 3.16, XPS and IRAS measurements as well as LEED images which characterize a post-reacted FeO(111)/Pt(111) sample (after exposure to 10 mbar CO + 50 mbar $O_2$ balanced with He to 1 bar for 80 min at 450 K), are summarized. The XP O 1s region depicting the hydroxyl shoulder at 530.8 eV and the main peak at 529.3 eV in combination with the IR absorption features at 3645 - $3630\,cm^{-1}$ document the presence of the FeO(OH) phase after the reaction. The LEED pattern confirms that the films remains structurally intact. These results are evidence for a hydroxylated FeO(OH) trialyer analog to those which we obtained after exposure to ambient conditions (see figure 3.7).

The significance of the *in situ* characterization of the catalyst has to be pointed out here. It clearly demonstrates that, indeed, the FeO(OH) trilayer is the

active phase. In a previous study on CO oxidation on $FeO_2$ it was concluded based on an analysis of the post-reacted sample, that the trilayer dewets for reactions in oxygen poor conditions ($CO:O_2 > 1$) and remains stable in oxygen rich conditions [1]. Our *in situ* IRAS data shows, however, that even though our post-reacted sample exhibits properties of an intact FeO(OH) trilayer, the film dewets partially during the first 40 minutes of the reaction - despite of oxygen rich conditions ($CO:O_2 = 1:5$ at the beginning) - and rewets only after about 57 % of the CO have been consumed.

## 3.4. Conclusions

FeO(111)/Pt(111) and its derivates constitute a remarkable system. Not only are they evidentially a model for SMSI effects. They also possess an outstanding intrinsic catalytic activity and are surprisingly stable in ambient conditions. These properties make them a particularly interesting link between model catalysts and applied systems.

In air and water, FeO undergoes a bilayer $\rightarrow$ trilayer phase transition to FeO(OH) without dewetting or loosing its structural integrity. Due to different thermodynamic properties of each region of the Moiré unit cell, the trilayer transition does not proceed uniformly, but leads to the formation of a regular pattern of islands. This regular arrangement can be detected by STM in air and even water and can furthermore be detected by LEED after reinserting the sample into a UHV chamber. The trilayer formation is evidenced by an increase of the total XP O 1s peak area which goes along with a $\sim$(-0.4) eV binding energy shift of the main O 1s peak and the evolution of a high-binding energy shoulder which can be assigned to hydroxyl groups. Fe, which is now sandwiched between a bottom O layer and an atop OH layer, gets oxidized as can be concluded from a +1 eV binding energy shift of the $Fe\,2p_{3/2}$ photoelectron peak. Furthermore, the trilayer OH groups absorb infrared light in the range of 3620 - 3650 $cm^{-1}$.

Water and water/oxygen codosing experiments in UHV revealed, that the presence of oxygen is decisive to drive this transformation. When only water is dosed, OH formation starts only at 10 mbar water pressure and leads to a phase showing different properties compared to the FeO(OH) phase formed in ambient conditions. Different results compared to ambient exposure experiments are also obtained when water is dosed in the presence of a glowing ion gauge filament. Here, the main XP O 1s peak does not shift, but is partially converted into an OH species. In total, no enrichment of oxygen is observed. Fe is not oxidized but, on the contrary, reduced (the $Fe\,2p_{3/2}$ photoemission peak shifts by -0.9 eV) and IR absorption is found at lower wavenumbers compared to FeO(OH), namely at around 3570 $cm^{-1}$. This process is probably promoted by hydrogen radical formation at the hot filament.

The sum of experimental observations was corroborated by DFT calculations which predict oxygen to be the driving force for the transition from bilayer to trilayer. The water chemical potential, in contrast, affects the degree of hydroxylation.

The nucleation of Au on FeO(OH) and FeO was investigated in this work to get further insight into the adatom-support interaction for these systems. The inertness of FeO towards Au for the coverages used here, is in accordance with literature. Interestingly, also for FeO(OH) there was no evidence for charge transfer. Furthermore, the OH groups on FeO(OH) seemed to be unaffected by the presence of Au adsorbates. The weak interaction makes it seem likely that Au can easily aggregate in the 'valleys' of the highly corrugated trilayer structure.

To check whether the FeO(OH) phase formed in ambient conditions has similar intrinsic activity towards CO oxidation as the $FeO_2$ trilayer, we performed *in situ* IRAS measurements of the reaction in oxygen rich conditions in a helium balanced atmosphere of a total pressure of 1 bar. Analog to $FeO_2$, the FeO(OH) samples showed indeed a high catalytic activity clearly outperforming the Pt(111) substrate. During the initial stages of CO oxidation - when the CO concentration was still high - Pt(111) was partially exposed at the surface. The film rewetted the surface, however, after the amount of CO had fallen below a critical limit. The rewetting was reflected by a sudden rise of the reaction rate.

# Chapter 4.

# CO Oxidation on MgO at Ambient Pressure

## 4.1. Introduction

### 4.1.1. Ultrathin Oxide Films - Properties and Catalytic Activity

In surface science, simplified systems are used to model applied catalysts in order to understand fundamental catalytic processes and principles. One approach, that has over years been successfully applied in our institute, is the use of model catalysts consisting of metal nanoparticles dispersed on a thin, metal single crystal supported oxide film. Typical examples for supported oxide thin films are MgO/Ag(001), MgO/Mo(001), FeO/Pt(111), $Fe_3O_4$/Pt(111) and $SiO_2$/Ru(0001). Oxide thin films allow to mimic to a certain extent a bulk metal oxide support for the dispersed active species. Furthermore, they are sufficiently conductive - even if the bulk oxide is a wide band gap semiconductor or insulator - such that surface science techniques, which use charged information carriers, can be applied without severe charging.

The transition between properties of ultrathin and thicker films with bulk - like properties is not abrupt and the region of transition depends on the material composition. Therefore, there is no general limiting thickness (or a similar limiting parameter) to distinguish between 'ultrathin' and just 'thin' films.

Ultrathin oxide films can have very different electronic, structural and catalytic properties compared to their thicker counterparts which behave quite similar to bulk material. Generally, a metal oxide should be grown on a metal support of the same symmetry and similar lattice constant. Still, the different lattices never match perfectly. As a result, ultrathin films exhibit a higher density of structural defects at the surface compared to thicker films.

Furthermore, compared to thicker films, ultrathin films have a different electronic structure at the surface which is 'felt' by adsorbates. The electronic structure of the surface can be altered due to hybridization between metal support and oxide. Alternatively, the metal wave function can propagate into the oxide while decaying exponetially, but still with a significant contribution at the surface [87]. These metal - induced gap states are a general feature of ceramic - metal interfaces, but in the case of ultrathin films their contributions to changes in the electronic structure can even affect the surface. Additionally, an adsorbate itself can induce a large structural change in the film. Charged species can be stabilized well by inducing a strong polaronic distortion in ultrathin films [88] and an image charge in the underlying metal. Ultrathin films are particularly susceptible towards polaronic distortions, since their lattice is very flexible. This

is, for example, evidenced by their phonon modes, which are often softer than the corresponding bulk phonons [89].

In favourable cases, if the metal support has a low work function and the adorbate has a high electron affinity, an initially neutral adsorbate can even be spontaneously charged on an ultrathin film. This effect was first predicted theoretically for Au on MgO/Mo(001) [90]. Later on, it was confirmed experimentally to occur in the case of ultrathin (3 monolayers), but not on thicker (8 monolayers) MgO/Ag(001) films [91]. $NO_2$ has also been shown to become charged on ultrathin MgO/Ag(001) films [92] and has by DFT been predicted to get charged on BaO and $Al_2O_3$ [93, 94] as well. These results show that ultrathin films can substantially alter the properties of adsorbates. The ability to spontaneously charge adsorbates and to stabilize them can be a key point for catalytic activity.

Thin oxide films have mainly been used as a support for dispersed metal particles, which constitute the catalytically active species. Only recently, the intrinsic catalytic properties of ultrathin metal oxide films have attracted increasing attention. The 1 ML FeO(111)/Pt(111) film, whose structure and chemical and catalytic properties are explained in chapter 3, is an example for such a system.

In 2008, Hellman *et al.* [2] postulated in a theoretical paper that ultrathin MgO(001)/Ag(001) films should be catalytically active towards CO oxidation as well. Their calculations indicated that these films should activate adsorbed molecular oxygen by forming and stabilizing a superoxo species ($O_2^-$) [2]. In 2011, Gonchar [3] *et al.* reported the observation of activated oxygen (about 2-5 monolayer percent) on 4 ML MgO(001)/Mo(001) thin films by EPR (electron paramagnetic resonance) which was stable even at 350 K. The authors did not observe a superoxo species on thicker films. The promising results for ultrathin MgO films on Ag and Mo supports encouraged us to study in more detail the catalytic activity of both MgO/Ag(001) and MgO/Mo(001) films in CO oxidation at ambient pressures.

### 4.1.2. MgO - General Aspects

Magnesium oxide is a wide band gap (7.8 eV) [95] insulator. It crystallizes in a rock-salt structure, i.e. two intercalated fcc lattices with a lattice constant of 4.21 Å[96] (figure 4.1). Due to its simple electronic and geometric structure, it has been widely studied as a model system both as bare oxide and as a support for catalytic metal particles.

There is a large difference in electronegativity between Mg (1.2) and O (3.5) which causes a charge transfer of two electrons from Mg to O. As a result, MgO has an ionic character with a closed shell electronic structure and is thermally stable over a wide temperature range [97]. Its melting point is at 3125 K; its boiling point at about 3870 K [98]. In principle, the pristine surface is relatively inert, but defects (colour centers, undercoordinated sites at edges and corners etc.) have a large impact on the surface chemistry and render the surface more reactive ([99] and references therein). In vacuum, [001] facets are energetically
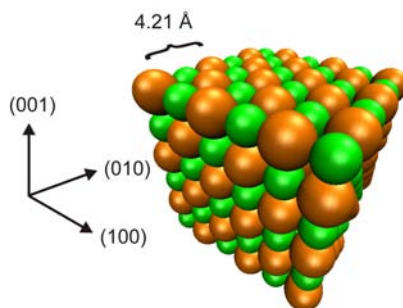
Figure 4.1.: The MgO lattice consitsts of two intercalated fcc lattices of Mg$^{2+}$ cations (green) and O$^{2-}$ anions (orange).

most stable. These Tasker type I surfaces neither have a net charge in the single layers nor is there a net dipole moment perpendicular to the surface [100].

In surface science, MgO is often used both as a single crystal [11, 101] and thin film [102, 103? ] model support for metal particles since it is relatively inert. But also, MgO itself is catalytically active towards several reactions, as for example the oxidative coupling of methane [104, 105], water-gas shift [106, 107] and the dehydration of methanol and formic acid [108].

## MgO on Mo

Molybdenum crystallizes in the bcc structure with a lattice constant of 3.15 Å [109] and is a refractory metal with a melting point of 2885 K [110]. It therefore allows for high temperature annealing which is the great advantage of this substrate. The high temperature treatment significantly improves the quality of thin MgO(001)/Mo(001) films [111].

In heteroepitaxal growth, the lattice mismatch $m$ between support and film is an important parameter. It determines, how much tensile or compressive stress a film experiences. The support lattice serves as reference, such that the lattice mismatch is defined as $m = \left[ \frac{a_f - a_s}{a_s} \right]$ with $a_f$ and $a_s$ being the lattice constants of film and substrate, respectively. Between the MgO(001) and the (001) surface of Mo, there is a mismatch of - 5.2%. Due to this relatively large mismatch, a superstructure with a periodicity of 60 Å is formed for thin MgO(001)/Mo(001) films (1 - 7 ML) (see figure 4.2). This leads to a regular modulation of the support - film separation (and therefore interaction), tilting of the film and regions of different alignment of both lattices. For 15 - 20 ML films, the surface is characterized by nonpolar steps. A relaxed film is not observed up to $\geq 25$ ML, where, however, 0.5% of the strain still remains [111].

## MgO on Ag

Out of all metals, Ag has the highest electrical conductivity [112]. The Ag crystal has an fcc structure with a lattice constant of 4.09 Å. Therefore, the lattice mismatch for an MgO(001)/Ag(001) system is + 2.9% [113], such that a
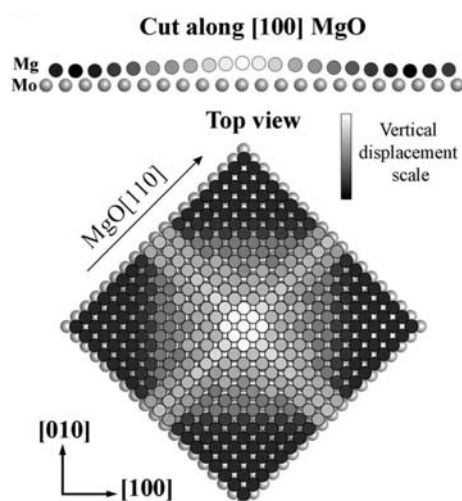
Figure 4.2.: Scheme of the elementary cell of the square super structure with a periodicity of 60 Å formed for thin MgO(001) films on Mo(001) to release the stress due to the lattice mismatch (from [111]).

compressive stress is imposed on thin MgO films by the Ag support. Still, this mismatch is rather small such that films of good quality can be obtained even in the ultrathin limit [114]. On the other hand, the melting point of Ag is rather low (1234.93 K) and the Ag(001) surface tends to reconstruct upon heating to about 600°C which allows only for annealing at relatively low temperatures. The MgO film grows in a layer - by - layer fashion (Franck van der Merve mode) on Ag(001) [115]. $Mg^{2+}$ cations are located at the hollow sites whereas $O^{2-}$ anions are located on top of the Ag atoms (see figure 4.3). Ultrathin films (1 - 3 ML) experience particularly strong compression from the Ag substrate, which is compensated by the introduction of dislocations. Mosaic formation has been observed for 1 - 7 ML films, with (100) planes tilted in the <010> directions. The tilting angle $\theta$ was found to be highest for 1 ML films and decreased with coverage $\Theta$ ($\theta \propto \Theta^{-5}$) [115]. Therefore, the defect density is expected to be highest for ultrathin films (1 - 7 ML).
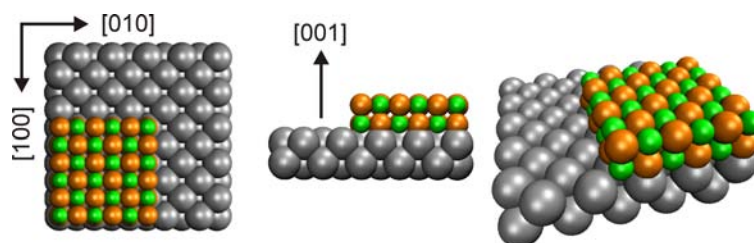


Figure 4.3.: MgO(001) crystallizes in a rocksalt structure on the (001) facet of a silver single crystal (fcc lattice). $Mg^{2+}$ cations (green) sit at the hollow sites whereas $O^{2-}$ anions (orange) sit on top of the Ag atoms (grey).

In summary, both supports offer different advantages. The MgO/Ag(001) system has a smaller lattice mismatch (+ 2.9% [115]) than the MgO/Mo(001) system (-5.2% [111]) and should therefore induce less strain in the ultrathin film. Mo, on the other hand, is a refractory metal, which allows for much higher annealing temperatures to reduce the defect density. According to DFT calculations, the work function of Mo covered by MgO is reduced by 2 eV [87] which would lead to an easier charge transfer to an adsorbed species. Furthermore, it has a high density of states at the Fermi edge and could therefore provide a large amount of electrons available for tunneling in the course of adsorbate activation [90].

## 4.2. Experimental

All CO oxidation experiments were performed using double side polished Ag and Mo crystals in the IRAS chamber (see section 2.7.1 for details). Cleaning, preparation and characterization (except IRAS) were carried out in the upper chamber. The samples were held by a tantanlum loop which was spotwelded to two molybdenum rods of the manipulator. The temperature was measured with a K - type thermocouple and both samples were heated by resistive heating. The cleanliness of the samples was checked by LEED and XPS prior to and after film deposition.

Cleaning of Mo

$\qquad$ 15 min sputtering in $1{\cdot}10^{-5}$ mbar $Ar^+$ ($I_{sample} = 0.8$ A)

$\qquad$ annealing to 950 °C (short flash)

Deposition of MgO on Mo(001)

$\qquad$ $1{\cdot}10^{-6}$ mbar $O_2$ atmosphere at 330 °C

$\qquad$ about 1 ML per minute

$\qquad$ afterwards 10 minutes annealing at 730 °C in UHV

Cleaning of Ag

$\qquad$ 30 min sputtering in $1{\cdot}10^{-5}$ mbar $Ar^+$ ($I_{sample} = 0.5$)

$\qquad$ 30 ,min annealing to 420 °C

Deposition of MgO on Ag(001)

$\qquad$ $1{\cdot}10^{-6}$ mbar $O_2$ atmosphere at 300°C

$\qquad$ about 1 ML per minute

$\qquad$ afterwards 5 minutes annealing at 400 °C in UHV

IRAS measurements which were run during the CO oxidation reaction were performed in the high pressure reaction chamber. The reaction was run at atmospheric pressure while a circulation pump was permanently mixing the gases.

The spectra were recorded with a Bruker IFS66v/S spectrometer and a liquid nitrogen cooled MCT detector. For each spectrum 500 scans were collected at a resolution of $4\,cm^{-1}$ and subsequently averaged. Unless otherwise stated, the procedure after moving the sample to the bottom chamber for CO oxidation measurements was as follows: The sample was flashed to $400\,°C$ and cooled down to room temperature ($\rightarrow$ background spectrum). The gases ($O_2$ and CO) were dosed one after the other ($\rightarrow$ 1 spectrum after each dose). Finally, the pressure was adjusted to 1 bar by adding helium ($\rightarrow$ 1 spectrum). The circulation pump was turned on 5 minutes prior to starting the reaction, such that the gases were well mixed right from the start of the heating ramp. The sample was heated at a rate of 1K/min from $30\,°C$ up to $150\,°C$. During this period, a spectrum was measured every 10 minutes. The background and baseline corrected IRAS spectra were analyzed by integrating the differential reflectance in the range of $2268$ - $1986\,cm^{-1}$ to quantify the CO consumption and between $2401$ - $2268\,cm^{-1}$ to quantify the $CO_2$ evolution.
.

## 4.3. Results and Discussion

### 4.3.1. CO Oxidation on MgO(001)/Mo(001)

In this measurement series, clean Mo(001), 3 ML MgO/Mo(001) and 30 ML MgO/Mo(001) samples were investigated. The CO pressure was always set to 5 mbar at the beginning. The oxygen pressure, however, was varied. Oxygen poor (0.25 mbar), stoichiometric (2.5 mbar) and oxygen rich (250 mbar) conditions were applied, since oxygen activation is the most critical step in this reaction and has so far only been observed experimentally to occur in the 2 - 5 monolayer percent range on ultrathin MgO/Mo(001) [3]. During the 2 - hour reaction ($30\,°C$ - $150\,°C$; 1 K/min), a decrease of about $1.5\,\%$ of the total pressure was observed which has to be taken into account in the data analysis. There are several components on the reaction chamber being potentially responsible for the loss (Teflon sealings between both chambers, leak valve, valve between reaction chamber and turbo pump).

For all samples, the total $CO_2$ evolution was very small (see figure 4.4); no significant activity was observed. Furthermore, there is no evident dependence on the oxygen pressure. The slight, linear decrease of the CO signal can probably be assigned to leaking of gases as mentioned above. In summary, the data seems rather random and potential activity of the samples was out of the resolution of our setup. Obviously, we cannot draw general conclusions from our measurements, but within the frame of reaction conditions that we used, activity for CO oxidation could not be observed for ultrathin MgO films on Mo(001).

Figure 4.5 shows the XP O 1s and Mo 3d regions of all samples (bare Mo(001), 3 ML MgO/Mo(001), 30 ML MgO/Mo(001)) in the pristine state and after reaction in oxygen poor, stoichiometric and oxygen rich conditions.
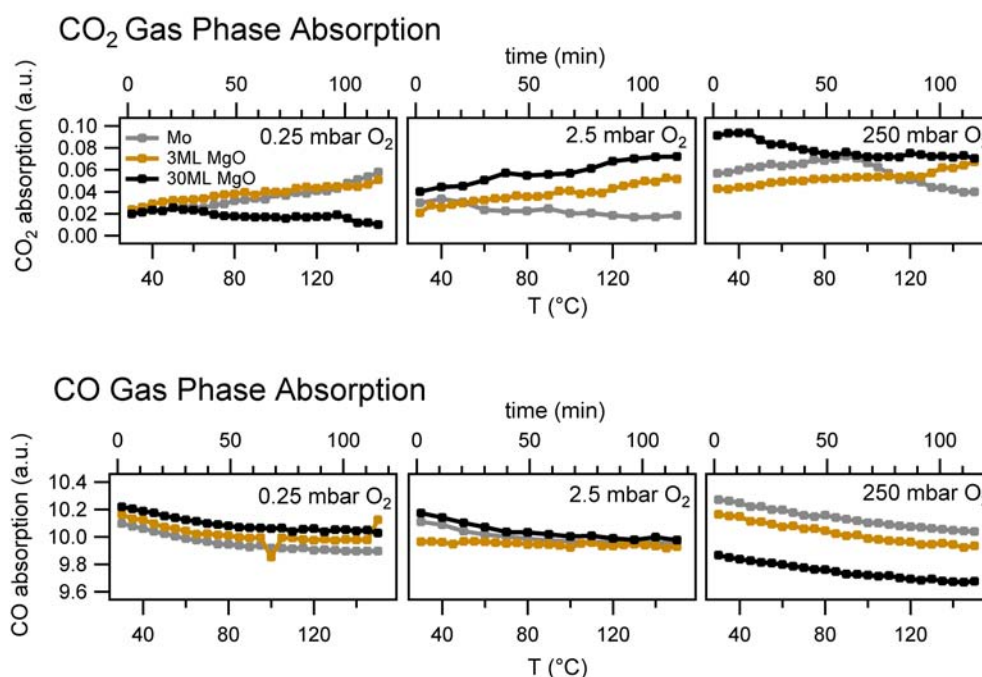
Figure 4.4.: Integrated infrared gas phase absorption of CO and $CO_2$ during CO oxidation reactions on MgO/Mo(001) films of different thickness at 1 bar total pressure (the pressure was adjusted by adding He). Left: 0.25 mbar $O_2$ + 5 mbar CO. Middle: 2.5 mbar $O_2$ + 5 mbar CO. Right: 250 mbar $O_2$ + 5 mbar CO.

Chemical modifications of the clean Mo sample can be observed after reaction. The peak at 530.4 eV binding energy in the O 1s region indicates the presence of oxygen at the surface. The signal intensity gets higher for higher oxygen pressures during the reaction.

Literature does not provide an unambiguous assignment of this feature. The O 1s binding energies for oxygen adsorbed on Mo(110) (530.2 eV [116]), MoO (530.5 eV [117]), $MoO_2$ (529.9 eV [118] - 531.1 eV [119]) and $MoO_3$ (529.8 eV [120] - 531.6 eV [119]) are reported in close vicinity and with overlapping ranges.

More insight can be gained by looking at the corresponding Mo 3d regions. The Mo 3d signal intensity decreases with increasing oxygen pressure in accordance with the increasing O 1s signal. In addition to the Mo $3d_{5/2}$ peak at 228.2 eV originating from metallic Mo [121], an oxidized Mo species evolves at 232.2 eV. This corresponds to $MoO_3$ [122]. Molybdenum in lower oxidation states is unlikely here, since such features are located at lower binding energies. $MoO_2$ shows a $3d_{5/2}$ peak around 229.5 eV [123] and the corresponding feature for MoO is located at around 228.3 eV [117]. Not surprisingly, the fraction of oxidized Mo is increasing with increasing oxygen pressures.

The 3 ML MgO/Mo(001) film shows an O 1s feature at 530.8 eV in the pristine state. The corresponding Mo $3d_{5/2}$ peak is located at 228.1 eV, indicating a metallic state of the substrate. However, due to the MgO film on top, the signal

intensity is lower than in the case of clean Mo. After reaction, the O 1s peak shifts by 0.6 eV to lower binding energy (530.2 eV) while a shoulder comes up at the high binding energy side at 532.0 eV, which can be assigned to hydroxyl groups. At the same time, molybdenum is, like in the case of clean Mo, partially oxidized to Mo(VI) as evidenced by a newly developed doublet with the Mo $3d_{5/2}$ peak at 232.4 eV. Apparently, the substrate is still exposed at the surface to some extent. This would be in line with the observation of exposed Ag at the surface of thin MgO(001)/Ag(001) films (see section 5.3.2 for details).

In the case of the 30 ML MgO/Mo(001) samples, the Mo 3d sample is strongly attenuated. Partial oxidation of the metal is not observed for any reaction condition, but can not be completely excluded since the signal is just slightly above the noise level. The O 1s peak shifts with increasing oxygen pressure from 531.1 eV for the pristine film to 530.6 eV for the used film after an oxygen rich reaction. Again, partial hydroxylation is evident from the high binding energy shoulder at 532.7 eV. The size of the shoulder is not proportional to the total O 1s signal, but is roughly equal to the size of the shoulder of the 3 ML MgO films, which supports the idea of a superficial hydroxylation. Such a superficial hydroxylation could be explained by the high pressure conditions (1 bar total pressure) which make it difficult to completely exclude residual water.
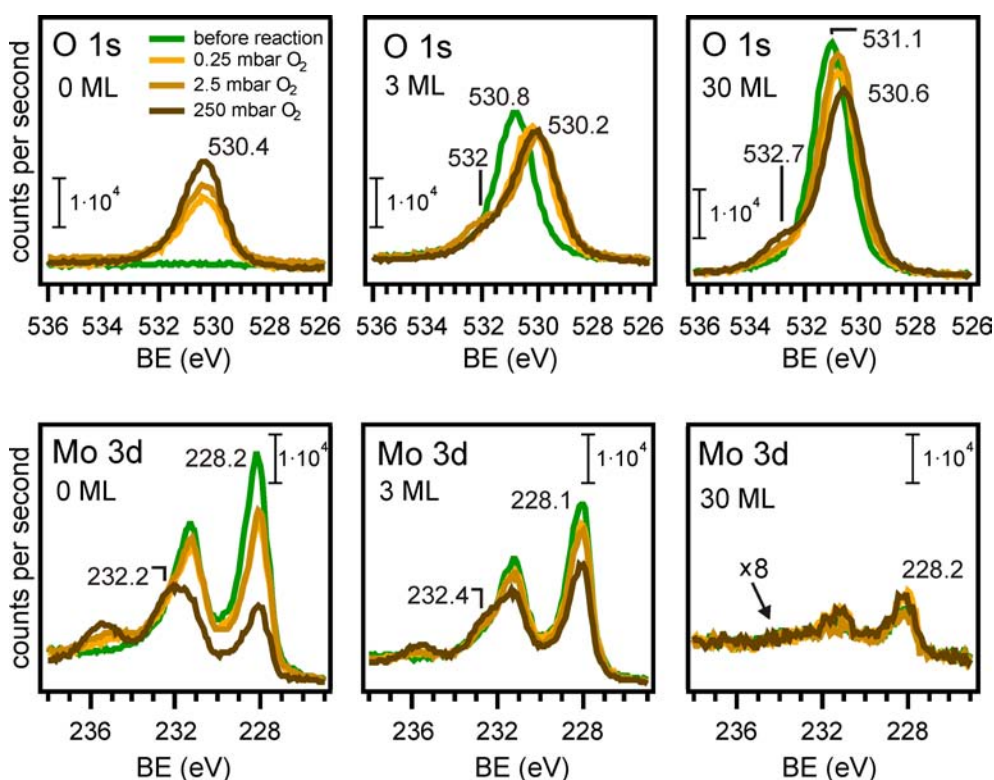


Figure 4.5.: XP O 1s and Mo 3d regions of all samples (bare Mo(001), 3 ML MgO/Mo(001), 30 ML MgO/Mo(001)) in the pristine state and after reactions in oxygen poor, stoichiometric and oxygen rich conditions.

### 4.3.2. CO Oxidation on MgO(001)/Ag(001)

In the MgO/Ag(001) series, clean Ag(001) as well as MgO films exhibiting a thickness between 2 and 50 ML were tested. For all reactions, an initial CO pressure of 5 mbar was used. The oxygen pressure was adjusted to 2.5 mbar (stoichiometric conditions) or 250 mbar (oxygen rich conditions) and the total pressure was finally adjusted to 1 bar by adding He. Figure 4.6 summarizes the magnitudes of CO and $CO_2$ IR absorption for all samples over the entire reaction time. Clearly, clean Ag(001) shows a high intrinsic activity. This is reflected in the $CO_2$ evolution and CO diminishment during the reaction. None of the MgO covered samples outperformed the high activity of Ag, such that there is no indication that the ultrathin Mg(001)/Ag(001) samples possess particular catalytic properties. With increasing thickness, the activity is progressively diminished but never reaches zero; not even for 50 ML films.
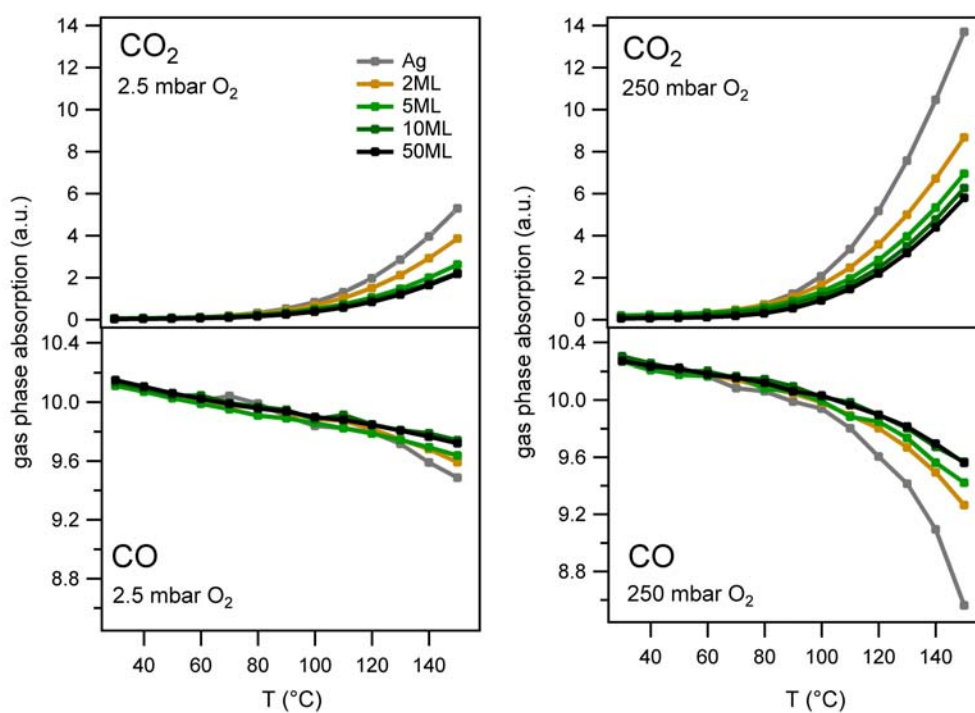


Figure 4.6.: Infrared gas phase absorption of CO and $CO_2$ during CO oxidation reactions on MgO/Ag(001) films of different thickness at 1 bar total pressure (adjusted by adding He). Left: 2.5 mbar $O_2$ + 5 mbar CO balanced with He. Right: 250 mbar $O_2$ + 5 mbar CO.

Since Ag is so active, the contributions from the edge of the crystal, which has not been exposed to Mg during film growth, have to be considered in the analysis (see figure 4.7). The crystal has a diameter of 10 mm and a height of 2 mm. For an ideal cylinder of these dimensions, the side makes up 29 % of the total surface area - quite a substantial amount! If one assumes in a crude approximation that top and bottom sides are completely covered by thick MgO films whose activity is

negligible and the side remains completely uncovered, then the measured activity should be reduced to 29 % compared to a clean Ag crystal.
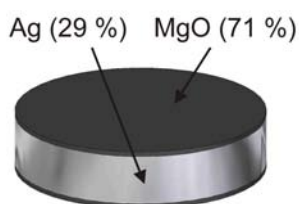


Figure 4.7.: In a simple cylinder model, Ag contributes still by 29 % to the total reactivity of a sample covered with MgO on both sides.

Since the gases were distributed homogeneously in the chamber by the circulation pump and the total pressure was approximately constant, the IR absorption can be assumed to be proportional to the partial pressure of the gas species under consideration. In case of a thick (50 ML) MgO/Ag(001) film, the final $CO_2$ IR absorption after reaction was 41 - 46 % lower than the corresponding signal in case of a clean Ag(001) sample. Of course, the sides of the MgO covered Ag crystal will not be perfectly uncovered which should reduce the measured activity even more, but on the other hand the side area is not smooth at all and should have a higher total surface area than approximated from the cylinder formula, comprising all sorts of facets and defects . In general, a deconvolution of contributions from MgO and exposed Ag is not possible from this data alone.

One can, however, compare the catalytic activity of the 50 ML MgO/Ag(001) and 30 ML MgO/Mo(001) samples. Since Mo does not show any significant activity, any difference between both samples should be attributable to Ag exposed at the side.

Figure 4.8 compares CO consumption and $CO_2$ evolution in oxygen rich conditions (250 mbar $O_2$) and stoichiometric conditions (2.5 mbar $O_2$) on thin (2 ML MgO/Ag and 3 MLMgO/Mo) and thick MgO films (50 ML MgO/Ag and 30 ML MgO/Mo) on both substrates. In oxygen rich conditions (figure 4.8, top), where the highest activity would be expected, the thin film data illustrates vast differences between both metal supports with respect to catalytic activity. Clearly, this is due to the high intrinsic activity of Ag (see figure 4.6, bare Ag) as compared to the negligible activity of Mo (figure 4.4, bare Mo). But even for thick films which are expected to be completely closed (see section 5.3.2), and in stoichiometric conditions (figure 4.8, bottom), where the activity should be rather low, there is some $CO_2$ evolution for the MgO/Ag sample. Again, the $CO_2$ evolution for the MgO/Mo sample is negligible in comparison. This indicates, that even after deposition of 50 monolayers of MgO, the edges of the Ag crystal are not completely covered and still contribute to the total activity.

Oxygen activation is a critical step during the reaction process. Therefore, a sufficiently high oxygen adsorption capacity is a crucial precondition. General tendencies of a correlation between oxidizing properties and the oxygen adsorption capacities of metal oxides have been reported [124]. In order to test for oxygen adsorption, $O_2$ TPD measurements were performed on MgO(001)/Ag(001) films of different thickness. In figure 4.9, $^{18}O_2$ desorption spectra from samples

Figure 4.8.: Direct comparison of $CO_2$ evolution and CO consumption between MgO films grown on Ag and on Mo. Top: Thin films ($2\,ML\ MgO/Ag$ and $2\,ML\ MgO/Mo$) in oxygen rich conditions ($250\,mbar\ O_2$). Bottom: Thick films ($50\,ML\ Mgo/Ag$ and $30\,ML\ MgO/Mo$) in stoichiometric conditions ($2.5\,mbar\ O_2$).

ranging from clean Ag(001) to 40 ML MgO(001)/Ag(001) are shown. Prior to the measurements, the samples were exposed to a saturation dose of $^{18}O_2$ at 100 K. A temperature ramp starting at 100 K and going up to 600 K with a rate of 3 K/sec was applied.

For the clean Ag(001) surface, a large desorption feature at around 160 K can be observed. For all MgO covered surfaces, this peak is drastically decreased in size, but it remains present even up to 40 monolayers of MgO. It shifts to higher temperatures with increasing MgO thickness, such that the maxima of the clean Ag sample and the 40 ML MgO/Ag sample are separated by about 20 K. Apparently, the Ag desorption is somehow affected by the presence of MgO. However, at 40 ML thickness, the samples do not expose silver at the surface any more (see section 5.3.2). Here, the residue of the characteristic peak might originate from the side of the crystal, where silver might still be partially exposed. The additional broad signal between 100 K and 300 K decreases only slightly with increasing film thickness. At least a significant fraction is most likely due to background desorption. Defect mediated adsorption will certainly also play a role. For MgO(001)/Ag(001) thin films, it has been shown that the composition of defects on the surface depends on thickness [125]. The contribution should be rather small, though, and cannot be separated from the background.
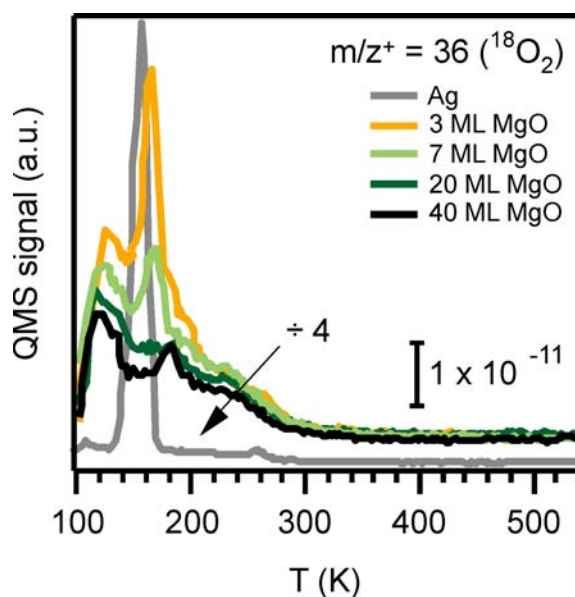


Figure 4.9.: $^{18}O_2$ TPD spectra on clean Ag(001) and thin MgO(001)/Ag(001) films of different thickness (rate = 3 K/sec).

The chemical changes which the samples underwent were traced by comparing XP spectra taken before and after the reaction. Figure 4.10 shows O 1s and Ag 3d regions of 2, 5, 10 and 50 ML MgO(001)/Ag(001) samples in the pristine state and after the reaction in oxygen rich conditions (5 mbar CO + 250 mbar $O_2$). The O 1s binding energies (figure 4.10, top) of the pristine samples shift to higher values with increasing film thickness (from 530.0 eV for 2 ML MgO/Ag to 531.1 eV for 50 ML MgO/Ag). Altieri *et al.* [126] attribute this phenomenon to

a reduction of on-site Coulomb interaction and charge transfer energy due to the presence of strong interfacial image potential screening by the metal. After the reaction in 250 mbar $O_2$, the samples are clearly hydroxylated as indicated by a shoulder showing up at around 531.2 eV. The intensity of the OH signal is roughly equally high for all samples, which shows that this modification affects only the surface. The main O 1s peaks have shifted to lower binding energy by about 0.8 - 1 eV, but still show the same relative shift with respect to each other. In contrast to the previous CO oxidation measurements on MgO(001))/Mo(001) thin films, the silver substrate is not oxidized after the reaction. For all samples the Ag $3d_{5/2}$ peak is located at 368.3 eV, confirming the metallic state of the substrate before and after the reaction (figure 4.10, bottom).
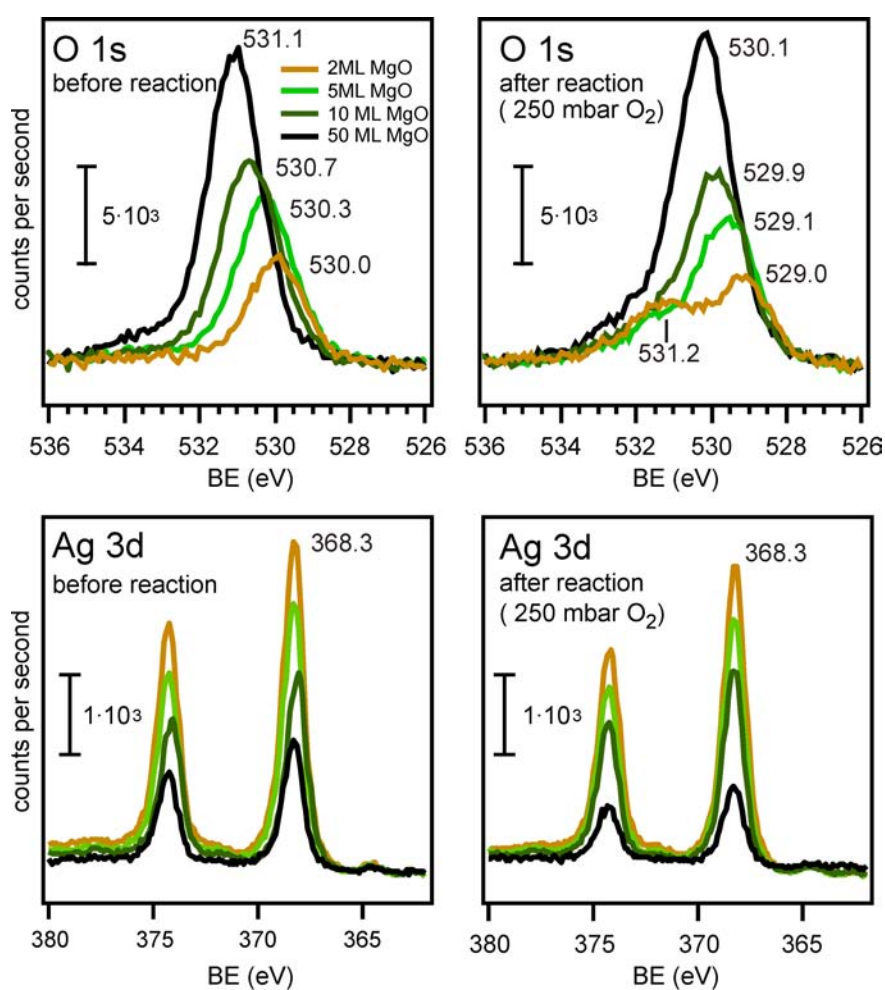


Figure 4.10.: XP O 1s and Ag 3d regions measured before and after reaction in oxygen rich conditions (5 mbar CO + 250 mbar $O_2$ balanced with He to 1 bar)

## 4.4. Conclusions

DFT calculations predict that molecular oxygen is spontaneously activated by transformation into a superoxo species upon adsorption on ultrathin Mg/Ag(001). This is supposed to result in a high catalytic activity of these films towards CO oxidation. In addition, EPR measurements indicate the spontaneous formation of activated oxygen on ultrathin Mg/Mo(001) with an estimated coverage of 0.02 - 0.05 ML superoxide on a 4 ML film. In order to test the activity of ultrathin MgO films supported on both Ag(001) and Mo(001) experimentally, we performed CO oxidation experiments at atmospheric pressures which we monitored by in situ IRAS. Furthermore, we investigated changes on the surfaces by analyzing pristine and post - reacted samples by XPS.

### MgO/Mo(001)

Clean Mo(001) as well as 3 ML and 30 ML MgO/Mo(001) were tested in CO oxidation conditions at atmospheric pressure with varying CO:$O_2$ mixtures (5 mbar CO + 0.25 mbar, 2.5 mbar or 250 mbar $O_2$ balanced with He to 1 bar). Mo(001) turned out to be a catalytically inert support showing no intrinsic activity. Both the ultrathin 3 ML as well as the thick 30 ML MgO/Mo(001) films showed no enhanced reactivity for any of the reaction conditions either. The CO conversion seemed rather random and was generally very low.

XPS measurements revealed that molybdenum was oxidized to Mo VI by the formation of $MoO_3$ after reaction on clean Mo samples and even when covered with a 3 ML MgO film. The degree of oxidation was increased for higher oxygen pressures. For the 30 ML MgO/Mo(001) films, the Mo 3d signal was just slightly above the noise level. A partial oxidation was not detectable in this case. These results are in principle consistent with ISS data for MgO on Ag(001), showing that only in the range of 30 ML MgO and above, Ag is completely absent at the surface (see section 5.3.1). An additional finding from XPS data is that the MgO films were partially hydroxylated after the reaction. The $O_{hydroxyl}/O_{lattice}$ fraction was higher for the thin films, i.e. the hydroxylation was superficial.

### MgO/Ag(001)

Clean Ag(001) and MgO(001)/Ag(001) films ranging from 2 to 50 ML thickness were investigated in this work. For the CO oxidation measurements, 5 mbar CO plus 2.5 mbar (stoichiometric) or 250 mbar (oxygen rich) $O_2$ were balanced with He to 1 bar total pressure. The $CO_2$ evolution was clearly dominated by the intrinsic activity of Ag. With increasing MgO film thickness, the activity decreased monotonically. No evidence for particular catalytic properties of ultrathin MgO layers on Ag was found. As in the case of molybdenum, MgO is hydroxylated after a 2 - hour reaction whith the $O_{hydroxyl}/O_{lattice}$ fraction decreasing for thicker films. In contrast to Mo(001), the surface of the Ag substrate was not oxidized after reaction, but remained in all cases in a perfectly metallic state. $^{18}O_2$ TPD spectra show that much more oxygen sticks to Ag than to MgO. As a general

trend, the oxygen adsorption capacity decreases continuously with MgO film thickness. Besides a characteristic desorption feature originating from oxygen on silver, there is a broad background signal. Desorption from MgO films might be contributing to this background, such that it cannot be excluded. The amount or a potential type of interaction (adsorption on terraces, defect‑mediated adsorption) can not be determined from this data.

In summary, we did not observe any significant catalytic activity of ultrathin MgO/Mo or MgO/Ag films towards the oxidation of CO outperforming thick films or the substrates. Obviously, this conclusion holds only for the parameter space which we investigated, such that we cannot make general statements. Furthermore, we have no information about the occurrence and degree of oxygen activation on our samples such that we can not directly contradict the predictions from DFT calculations and experimental results from EPR measurements. However, both our TPD and IRAS measurements strongly suggest that for our conditions, the formation rate of peroxide anions must be small even in the most optimistic scenario. What is special about the present study is that the samples were tested at ambient pressure, i.e. in more realistic conditions compared to previous studies. As a result, partial hydroxylation of the surface was observed by XPS after the reaction. An effect of the hydroxyls on the catalytic activity of the films cannot be excluded. Whatever the reason for inactivity might be, a lack of oxygen supply is unlikely, since the films are inactive even for very oxygen rich conditions ($5\,\mathrm{mbar}$ CO $+$ $250\,\mathrm{mbar}$ $O_2$).

# Chapter 5.

# Deposition of Pd on MgO/Ag(001) by Wet Impregnation

## 5.1. Introduction

### 5.1.1. MgO‑Supported Pd Catalysts ‑ General Aspects

Supported Pd catalysts are widely used in industry for hydrogenation, dehydrogenation and coupling reactions for the synthesis of fine and bulk chemicals [127]. In the field of fine chemicals, palladium is arguably the most versatile and the most widely applied catalytic metal. With the exception of hydrogenation and dehydrogenation and increasingly also C‑C coupling reactions, commercial Pd catalysts are mostly homogeneous ones with or without organic ligands [128]. A major drawback of homogeneous catalysis, which is of economic and environmental relevance, is the issue of separating the catalyst from the products. For this reason, the development of heterogeneous Pd catalysts has become a major area of catalyst research [129]. Supported Pd catalysts have been prepared on activated carbon [130], metal oxides [131] (silica, alumina, MgO, ZnO, $TiO_2$, $ZrO_2$ etc.), clays [132], zeolithes, organic polymers and others [133]. Furthermore, research has gone into fixing Pd complexes on a support, where ligands act as anchors by forming covalent bonds with the support [134].

A widely used model support for investigations aiming at elucidating the properties of supported Pd nanoparticles is MgO(001). For example, nucleation and growth of Pd [135, 136, 101], its cluster‑size dependent CO oxidation activity [137], or the oxidation and restructuring of Pd particles in oxygen environment [138] have been investigated using bulk MgO(001) single‑crystals as support. Furthermore, thin MgO(001) films grown on either Ag(001) or Mo(001) supports have been utilized to investigate the nucleation of single Pd atoms [139, 140], the reactivity of size‑selected Pd clusters [103], or the electronic properties of Pd on MgO(001) [141, 142]. The Pd‑MgO system has also been intensively studied computationally, including topics such as the fundamental interaction of Pd atoms with the MgO surface and its point defects [143, 144], the diffusion of small Pd clusters [145, 146], the morphology of larger Pd particles [147, 148], or the oxidation of small Pd clusters [149]. In addition, the fact that Pd particles of well‑defined morphology can be prepared on MgO powders provided the basis for detailed investigations into chemisorption properties and reactivity, for example, in CO adsorption, CO hydrogenation, or methanol decomposition, that allowed a direct comparison of the observed spectroscopic features to results

from studies on Pd single-crystals and Pd particles grown on single-crystalline oxide support [150, 151].

From a more applied catalysis point of view, MgO is an interesting material because of its basic properties. It has been reported that the selectivity in the CO hydrogenation reaction over supported Pd catalysts is strongly directed towards oxygenated products when basic oxides such as MgO are used as support itself or as a promoter in Pd catalysts supported by other oxides [152, 153], which has been related with the stabilization of formate-type intermediates at the Pd-MgO boundary [154]. Another test reaction, where Pd-MgO catalysts give promising results, is phenol hydrogenation [155, 156, 157]. It has been shown that both, the Pd dispersion and the long term activity are higher over Pd-MgO compared to Pd-$Al_2O_3$. The observed differences were explained by the stronger interaction of Pd with MgO and the suppression of coke formation over the basic MgO [156]. The basic properties of MgO have also been suggested to be the origin for the observation of electron-rich Pd particles on this support, a conclusion that has been deduced from reduced Pd binding energies [157] and from the specific stretching frequencies of CO on Pd-MgO catalysts [158, 159].

From a practical point of view, the main drawback of MgO is its rather low stability, which limits its use as a support material in heterogeneous catalysis. Although MgO powders with high specific surface area can be prepared, this material strongly sinters following deposition of Pd by wet preparation routes such as impregnation or deposition-precipitation [160]. The reason for the sintering may be found in the instability of MgO in humid and aqueous environment. In particular, in acidic solutions, which are most frequently applied in Pd catalyst preparation by impregnation, dissolution is a more serious problem for ionic oxides such as MgO than for the more covalent oxides such as $Al_2O_3$ and $SiO_2$.

The reactivity of MgO towards water and the restructuring and dissolution in aqueous environments represent a challenge for studies aiming at bridging the surface science model approach to applied catalysis. In order to elucidate the influence of surface hydroxyls on the interaction of metals with MgO surfaces, our group has recently investigated the controlled hydroxylation of model MgO(001) thin film surfaces and the nucleation and sintering of gold on hydroxylated MgO [75, 161, 82].

In an attempt to further move towards realistic conditions, our group has recently introduced a surface science approach to mimic the preparation of applied catalysts. It utilizes thin, metal single crystal supported oxide films as substrate to study the formation of supported metal catalysts via real-world preparation techniques such as impregnation or deposition-precipitation. This allows to apply the full range of surface science techniques on realistically prepared samples. In our previous studies, $Fe_3O_4(111)$/Pt(111) films were used as substrate, which were shown to be very stable in various conditions (strongly acidic to strongly basic) [162, 163].

In the present work, an analog approach is applied to study the preparation of an MgO-supported Pd model catalyst by applying wet-chemical preparation routes and using Ag(001)-supported MgO films as substrate.

Since MgO is more soluble than iron oxides, the stability of Ag(001)-supported MgO(001) thin films in various aqueous environments has first been explored in order to find appropriate conditions for Pd deposition. Next, the thermal decomposition of adsorbed Pd precursor complexes into Pd nanoparticles was studied with XPS and STM for Pd deposited on ultrathin (5 monolayers, ML) and thick (60 ML) MgO films. Furthermore, the Pd loading and the chemical state of the raw catalyst were investigated as a function of precursor concentration and deposition time on thick (60 ML) MgO films. Subsequently, several deposition parameters which determine the chemical state of the Pd deposit were investigated in detail. Finally, CO chemisorption and CO oxidation probed with TPD allowed to compare the properties of Pd-MgO model catalysts prepared by Pd deposition from aqueous precursor solution with those of a Pd-MgO sample prepared exclusively in UHV via physical vapor deposition of Pd. Before going into the results of this study, a short introduction will be given into catalyst preparation methods and the chemistry of the Pd precursor and MgO substrate in aqueous solutions.

### 5.1.2. Preparation Methods

In general, the preparation methods in applied catalysis differ vastly from those used to prepare surface science model catalysts. While in surface science, the catalyst is usually prepared by evaporation of the desired metal onto a support followed by an annealing step, the situation is much more complex in the case of industrial catalysts. Here, the metal source is commonly a salt or precursor complex which is suspended in aqueous or organic solvents. A range of different procedures can be used to immobilize the precursor on a substrate, for example dry or wet impregnation, ion exchange, sol-gel processing, deposition-precipitation or deposition-reduction. After the deposition step and before drying, the raw catalyst can be rinsed to remove undesired components. To remove the ligands with higher purity, a calcination procedure is applied - commonly by heating in oxygen - which leads to sintering and oxidation of the deposited metal. The remaining oxidized metal particles are finally activated by a reduction step [164] (see figure 5.1).

Impregnation is the most frequently applied method for the preparation of heterogeneous Pd catalysts [165]. Here, the support is exposed to a solution which contains the metal precursor as a complex. Two types of surface-precursor interaction are considered as being strong enough to drive precursor adsorption: I) electrostatic interaction between surface OH groups and ligands of the metal complex, which requires that the two species exhibit opposite charge [166] and II) ligand substitution by surface groups [167].

The degree of electrostatic interaction is determined by the charging of both, the precursor and support, which, in turn, is governed by the pH of the precursor solution. Depending on the pH, the precursor can undergo hydrolysis/condensation reactions or ligands can be replaced by protons or hydroxyl groups. Upon contact with aqueous solutions, the surface of most metal oxides
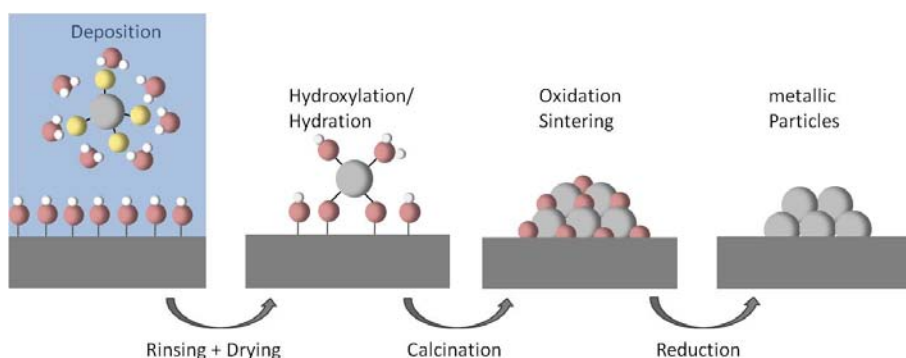
Figure 5.1.: Common steps applied in industrial catalyst preparation (gray = metal, yellow = ligand, red = oxygen, white = hydrogen)

is hydroxylated. The pH‑dependent protonation/deprotonation equilibrium of surface hydroxyls determines the overall surface charge. The point of zero charge (PZC), i.e. the pH at which the surface net charge equals zero, depends on the acidity of the different OH groups present on the surface. The fact that there is no overall charge at the PZC can, however, also mean that positively and negatively charged groups are equally present such that electrostatic interaction is possible even under these conditions. An example that demonstrates the influence of the solution pH on the catalyst loading was provided by Contescu *et al.* [168].

Impregnation is often performed with highly porous supports and can be classified into two categories depending on the pore/solution volume ratio. In dry impregnation, the volume of the precursor solution is equal to the support pore volume. The solution is completely sucked into the support pores by capillary forces, such that no waste of precursor solution remains. Since precursors are often expensive, this can be a substantial advantage. Wet impregnation, on the other hand, involves the use of an excess of precursor solution. Often, a washing step is carried out before drying to remove unwanted residues from the surface, which could have negative consequences for the catalyst properties such as poisoning or reduced metal dispersion. The single‑crystalline model support used in this study is flat and non‑porous. Capillary forces can therefore not contribute to the precursor transport such that dry impregnation cannot be applied here. Instead, a procedure which resembles wet impregnation was applied.

In the case of Pd catalysts it has been observed that (i) washing the raw catalyst, (ii) calcining prior to reduction and (iii) gas phase reduction instead of liquid‑phase reduction favour a high dispersion of Pd particles [165]. In the experimental work presented here, all these conditions were fulfilled.

### 5.1.3. The Pd Precursor

In order to understand the processes which lead to the final catalyst, information about the chemistry of the precursor complex is of importance. The solubility of $PdCl_2$ powder - from which the precursor complex is derived - in water

is minuscule. It can be dissolved in concentrated hydrochloric acid where predominantly $[PdCl_n(H_2O)_{4-n}]^{2-n}$ complexes are formed [169]. The relative concentrations for $n = 1 \ldots 4$ depend on the chlorine concentration. When the pH is increased, the ligands are gradually replaced by $OH^-$ groups (see figure 5.2). Around pH 4, the neutral $Pd(OH)_2(H_2O)_2$ complex is a stable hydrolysis product which tends to condensate into long, polynuclear chains forming small colloidal nanoparticles or a precipitate. Once formed, these complexes are stable over a wide pH range [170]. Their structure has been investigated by TEM, EXAFS and UV-diffuse reflectance spectroscopy [171, 127]. In order to avoid the formation of a precipitate during preparation of an alkaline precursor solution, the pH needs to be changed from acidic to alkaline as rapidly as possible. In strongly alkaline conditions (pH 12), mononuclear $Pd[OH]_4^{2-}$ complexes are formed [169].
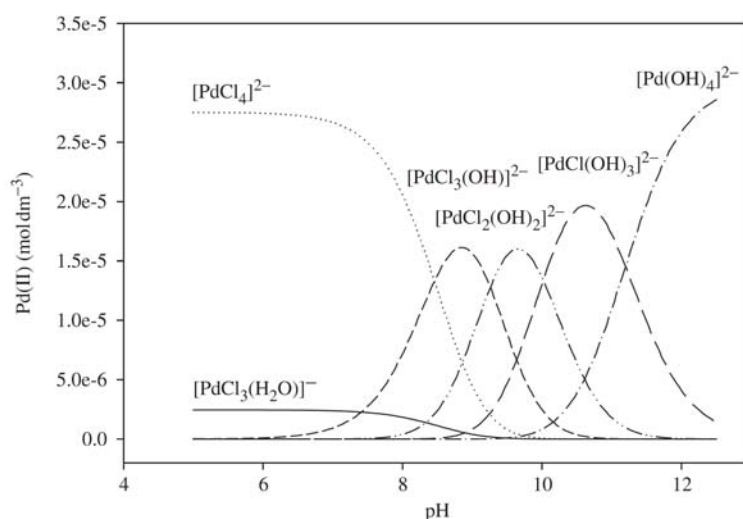


Figure 5.2.: Pd complexes in aqueous solutions. The ligand composition depends on concentrations and pH. Here, the pH dependence is plottet at a chlorine concentration of 0.5M [169].

### 5.1.4. MgO - Water System

Bulk MgO is known to be poorly soluble in pure water (86 mg·l$^{-1}$ at 30°C [172]) whereas it dissolves rapidly in acidic solutions [173, 174, 175, 176].

MgO dissolution studies have been performed with powders [177, 178], rotating discs[177], cleaved [179] or polished bulk crystals [180] and small crystallites - so called MgO smoke [181, 182]. Furthermore, this topic has been investigated computationally [183, 184]. However, a direct comparison between different studies is not possible, because they deal with different samples, time scales, pH values and MgO surface/solution volume ratios.

There is general agreement that MgO dissolves faster in acidic than in alkaline solutions. *In situ* AFM images reported in [184] clearly illustrate this effect.

Hacquart and Jupille [181, 182] concluded from their studies on small MgO crystallites that the dissolution rate depends on the type of facet and that even the dissolution mechanism might be facet dependent. As a consequence, studies on poorly defined surfaces and powders would only yield a dissolution rate averaged over all contributing facets and surface structures which would be highly dependent on the surface order and facet composition. Indeed, the spread of reported rates is quite broad.

In principle, the dissolution of MgO proceeds via the desorption of $OH^-$ and $Mg^{2+}$. The mechanisms, however, differ between the acidic and basic regime and there is no comprehensive evidence which proves a particular mechanism to be the one and only. Theoretical calculations show that the adsorption energy on MgO is larger for protons than for hydroxyl groups [183] which explains the high PZC of MgO (about 12). Therefore, the surface hydroxyls are protonated even in the neutral regime.

Both Vermilyea [178] and Fruhwirth *et al* [177] observed high dissolution rates in the acidic regime which they assigned to a thermodynamically controlled proton attack mechanism. They assigned the slowdown of dissolution towards the neutral regime to a proton attack mechanism which is increasingly controlled by the diffusion of $H^+$. Proton attack of an hydroxylated MgO surface might proceed as

$$(MgOH)^+ + H^+ \Leftrightarrow Mg^{2+} + H_2O$$
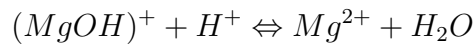
At about pH 8, they observed a plateau [178] and a small increase [177] of the dissolution rate towards higher pH. The authors claim that in this range, the proton attack mechanism is replaced by an $OH^-$ attack mechanism which could be written as

$$(MgOH)^+ + OH^- \Leftrightarrow Mg^{2+} + 2OH^-$$

.
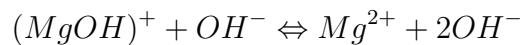
This reaction would drive the pH to even higher values. However, at pH values above 9 the rates decline continuously which the authors assign to the formation of $Mg(OH)_2$. $Mg(OH)_2$ dissolves very slowly and protects the bulk by forming an impermeable layer [185]. According to this picture, a superficial layer of $Mg(OH)_2$ would be formed as a dissolution intermediate - at least in alkaline solutions:

$$(MgOH)^+ + OH^- \Leftrightarrow Mg(OH)_2$$

$$Mg(OH)_2 \Leftrightarrow Mg^{2+} + 2OH^-$$
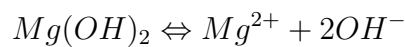
Vermilyea [178] proposed the formation of such a layer, since the observed dissolution rates were quite close to those of pure $Mg(OH)_2$ in this pH range and

significantly lower than what was expected for MgO. However, he could not find experimental evidence for this hypothesis, such that he expected this layer to be very thin.

For MgO in vacuum or in an atmosphere of inert gases, the (001) facet is energetically by far the most stable having a surface energy which is half that of MgO(110) [186]. It was theoretically predicted that the (111) facet would be the most stable one in water environment [186, 187] which was confirmed experimentally [181, 182] (See Fig.5.3).
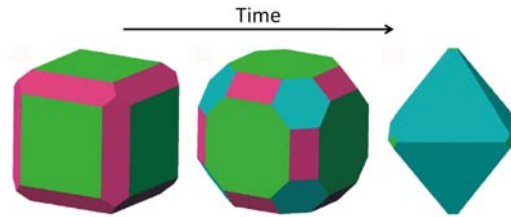


Figure 5.3.: Dissolution of MgO crystallites exhibiting (001) facets in aqueous solution [181]. Initially, (110) facets evolve at the edges of the cubes. Later on, (111) facets evolve at the corners which finally become dominant.

So upon increasing the humidity of the atmosphere, the MgO(001) surface should become more and more energetically unfavourable. Holt *et al* [179], who did AFM studies on bulk MgO single crystals, reported strong restructuring of the surface in terms of roughening and precipitation of aggregates of up to 200 nm height when the relative humidity of air exceeded 50%. It has been shown by our group that the entire surface of a thin MgO(001)/Ag(001) film is hydroxylated and roughened upon exposure to water vapor at pressures higher than $10^{-6}$ mbar [75]. Therefore, it is clear that samples that have been freshly prepared in UHV and are taken out of the chamber - which represents a sudden and drastic change of equilibrium conditions - will be hydroxylated, rough and rich in defects. Since the dissolution at defects is believed to proceed faster than on low index planes [180, 185], we expect a high initial dissolution of our roughened MgO/Ag(001) thin films. A requirement for LPD on MgO thin films is to find deposition conditions for which the films are stable within the time span of exposure to the aqueous solution, i.e. where negligible dissolution rates are observed. A dissolution rate of zero represents a steady state equilibrium between dissolution an precipitation. Apart from re-precipitation of $Mg(OH)_2$ which is especially favoured in alkaline conditions, a possible role of carbonate is discussed by [179]. Even deionized water is enriched in carbonate when it is exposed to ambient air for some time due to $CO_2$ dissolution. Therefore, equilibrated laboratory water has a slightly acidic pH of 5-6 with a carbonate concentration of about 5-10 ppm. $Mg^{+2}$ might therefore precipitate as

$$Mg^{2+} + CO_3^{2-} \Leftrightarrow MgCO_3$$
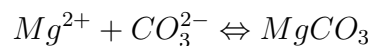
Analogous to the precipitation of $Mg(OH)_2$, this is a reversible process which might contribute to a steady state equilibrium accompanied by reshaping of the surface and embedding of carbon. Mass transport and re-precipitation phenomena leading to the formation of amorphous structures have been observed by several authors (See Fig. 5.4) [179, 182, 176, 188].
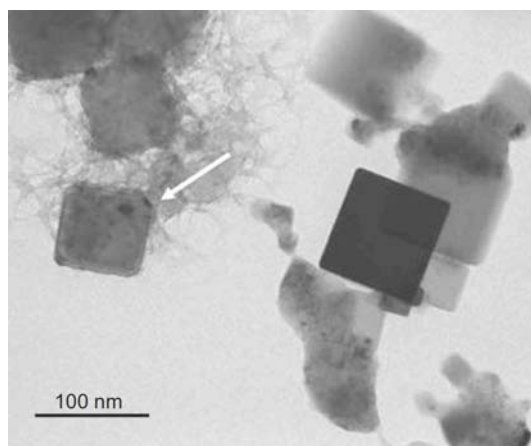


Figure 5.4.: Upon exposure of MgO(001) crystallites to humid air for one day, mass transport and redeposition of amorphous material was observed by Hacquart and Jupille[182]. They assume the amorphous material to be $Mg(OH)_2$.

## 5.2. Experimental

### 5.2.1. General

For all experiments concerning LPD of Pd on MgO, crystal cleaning and oxide film deposition as well as sample characterization by LEED, AES and TPD were performed in the STM preparation chamber. For XPS measurements, the sample was transferred to the SFG chamber (see section 2.7.2 for details). The Ag(001) crystal was cleaned by several cycles of sputtering for 1 hour (0.5 A sputter current in $5 \cdot 10^{-6}$ mbar $Ar^+$ atmosphere) and subsequent annealing for 30 minutes to 430°C. Prior to deposition, the crystal quality and cleanliness were checked by LEED and AES.

Magnesium oxide was deposited in an atmosphere of $1 \cdot 10^{-6}$ mbar $O_2$ at 300° C and at a deposition rate of one monolayer per minute. In a final step, it was annealed for 5 minutes in UHV to 430°C. The freshly prepared MgO film showed the same LEED periodicity as clean silver. Figure 5.5 shows Auger spectra of Ag(001), 60 ML MgO(001)/Ag(001) and, for completeness (even though AES was not used for the analysis of Pd), Pd‑MgO/Ag(001) prepared by LPD (5 min, 2.5 mM $Pd^{+2}$). The most prominent peak of the $Ag_{MNN}$ series is located at 356 eV. This feature disappears after deposition of 60 ML MgO while a new peak at 507 eV originating from the $O_{KVV}$ Auger process appears instead. Kinetic energies of Auger electrons of magnesium are located at 1180 eV (KLL) and at

about 40 eV (LVV). The LVV peak could indeed be detected for thicker films. However, the settings had to be changed to get an acceptable signal at such a low energy. The signal to noise ratio was low and the reproducibility of the signal intensity poor, such that this peak was not be used for quantification. The most intense peak of the Pd $_{MNN}$ series is located at 330 eV. The peaks of the MNN series of both Ag and Pd overlap which complicates quantitative data analysis. In the present work, XPS was used instead to quantify the loading of Pd.
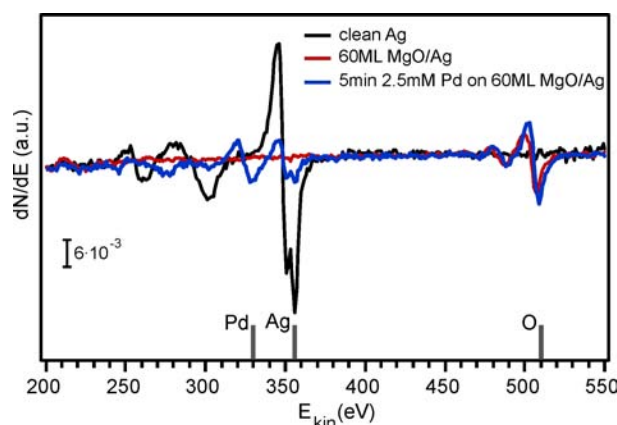


Figure 5.5.: Auger spectra of Ag(001), 60 ML MgO(001)/Ag(001) and Pd-MgO/Ag(001) prepared by LPD (5 min, 2.5 mM Pd$^{+2}$).

## 5.2.2. LPD of Pd onto MgO

In order to minimize contaminations, all LPD glassware was cleaned by a wet chemical procedure prior to use. In a first step, the dishes were put in an alkaline solution (pH 9 - 10) of KMnO$_4$ (3.5 l Millipore water, 3 pellets of KOH, a few spatula tips of KMnO$_4$) over night . Subsequently, they were rinsed with Millipore water before being immersed in an acidic (pH < 0) H$_2$O$_2$ solution (3.5 l Millipore water, 200 ml 30 % H$_2$O$_2$, 10 ml concentrated H$_2$SO$_4$). The dishes were rinsed again and finally boiled in Millipore water.

The deposition of Pd from the liquid phase was carried out in ambient air, such that the MgO(001)/Ag(001) substrate, which had been prepared in UHV, was taken out of the vacuum chamber. Subsequently, the sample holder was suspended in a beaker with the crystal facing down. The beaker was filled with precursor solution until the crystal surface was wetted by a hanging meniscus (see figure 5.6). With this configuration, unwanted contact between precursor solution and the sides of the crystal or parts of the sample holder was minimized.



Figure 5.6.: Deposition of Pd from precursor solution in a hanging miniscus configuration.

## 5.3. Results and Discussion

### 5.3.1. MgO Thin Films in Water - Dissolution Experiments

**MgO Thickness Calibration**

To our best knowledge, no studies about the behaviour of MgO thin films in aqueous solutions have been reported so far. Therefore, the stability of these films had to be tested prior to any LPD experiments, such that appropriate deposition conditions could be determined. Using thin MgO/Ag(001) films allows the gradual decline of MgO layer thickness and therefore the dissolution rates to be monitored with high precision. In this work, the change of film thickness was quantified by AES. A MgO thickness calibration curve was acquired first by measuring Auger reference spectra of MgO(001)/Ag(001) films of different thickness, which were prepared by PVD.

In principle, Auger signal intensities of a substrate $S$ and a film $F$ can be expressed as a function of film thickness $d$. A crucial parameter is the inelastic mean free path $\lambda_X^Y$, which is the characteristic length, at which the intensity of an electron beam of energy $X$ has decreased by $\frac{1}{e}$ when passing through a medium $Y$. Since the distance, which Auger electrons travel through the film, depends on the angle $\theta$ between their velocity vector and the surface normal, it has to be expressed as $\frac{-d}{\cos\theta}$. For the hemispherical retarding field analyzer used in this work, an average angle of 42° can be used in good approximation [189]. The substrate Auger electrons are attenuated in a simple exponential manner when passing through the film, such that their intensity can be expressed as:

$$I_S\left(d\right) = I_{S,0} \cdot \exp\left(\frac{-d}{\cos\theta \cdot \lambda_S^F}\right) \tag{5.1}$$

Auger electrons originating from the film are both created and attenuated in the same medium. It follows that:

$$I_F\left(d\right) = I_{F,0}\left[1 - \exp\left(\frac{-d}{\cos\theta \cdot \lambda_F^F}\right)\right] \tag{5.2}$$

$I_{X,0}$ contains, amongst others, information about the detection efficiency which is a device constant, the transmission factor and the Auger cross section. In this work, the device specific $I_{Ag,0}$ and $I_{O,0}$ were obtained from a clean Ag(001) crystal and a very thick MgO/Ag(001) film for which the Ag peak was completely suppressed in the spectrum.

The experimental calibration curve was compared to the theoretical model with fits obtained with *Igor* using values for $\lambda_X^Y$ from different sources [190, 191, 192] (see table 5.1 and figure 5.7). In summary, all theoretical fits overestimate the experimental oxygen signal and the $V_{pp}(O)/V_{pp}(Ag)$ ratio and underestimate the experimental silver signal (see figure 5.7). Similar results, showing the same tendency of strongly overestimating the $V_{pp}(O)/V_{pp}(Ag)$, have been obtained previously [193]. It has to be considered at this point that the model simplifies the system by assuming a perfectly smooth film on top of a perfectly smooth

| Source | $\lambda_{Ag}^{MgO}$ (356 eV) | $\lambda_{O}^{MgO}$ (507 eV) |
|---|---|---|
| Akkermann [190] | 9.74 Å | 12.65 Å |
| Tanuma [191] | 11.38 Å | 14.9 Å |
| Kwei [192] | 11.88 Å | 15.39 Å |
| free fit | 34.96 Å | 34.86 Å |

Table 5.1.: Inelastic mean free paths in MgO
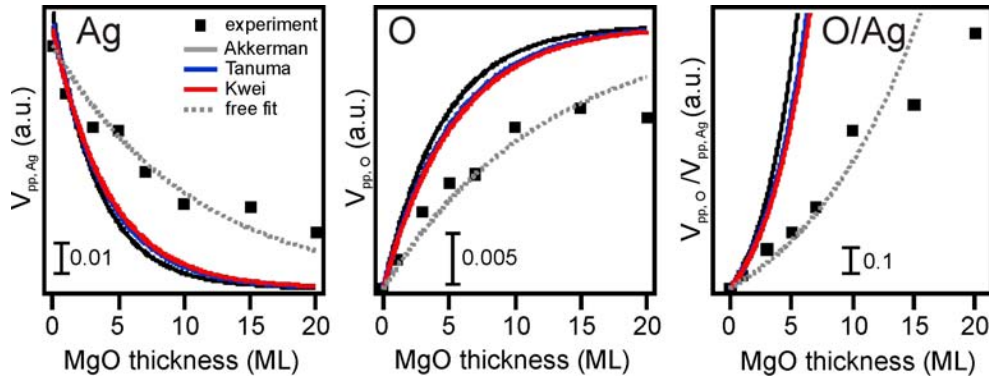


Figure 5.7.: Experimental calibration data is compared to theoretical fits using values for $\lambda_X^Y$ from different literature sources [190, 191, 192]. In addition, a free fit was performed, such that in following experiments, nominal thicknesses could be assigned.

substrate. Therefore, we can conclude that the real films are most likely irregular in thickness. Since the reproducibility of absolute intensities of Ag and O signals in our spectra was not satisfactory, we instead used the more reliable peak‑to‑peak ratio $V_{pp}(O)/V_{pp}(Ag)$ as a measure of thickness.

In order to evaluate the dissolution studies to be presented below, and to assign - if not absolute - at least nominal thicknesses, the calibration curves were modeled with a simple exponential fit where the inelastic mean free path was an adjustable parameter (see figure 5.7, curves of free fits).

Since such a strong divergence between theoretical model and experiment was observed in the Auger measurements, the question arose, at which nominal MgO coverage the Ag substrate is completely covered. Obviously, to avoid Pd‑Ag interaction, a complete closeness of the MgO films is a crucial precondition for further LPD experiments. The film closeness as a function of nominal thickness was investigated by ISS, which allows to probe the outermost atomic layer of the sample exclusively (see section 2.3). A clean Ag(001) surface as well as MgO(001)/Ag(001) films of thicknesses ranging from 2 to 32 monolayers were characterized by ISS using a beam of ionized helium. The spectra were analyzed

by determining the areas of peaks that could be assigned to Mg, O and Ag. Ag
was detected at the surface for up to 15 monolayers and only disappeared com-
pletely for 32 monolayers (see figure 5.8, top and bottom left). The peak areas
for Mg and O, on the other hand, fluctuated slightly around a constant value
for any investigated MgO coverage (see figure 5.8, bottom right). In summary,
these measurements clearly show that Ag is exposed at the surface for films up
to a nominal thickness of at least 15 monolayers.
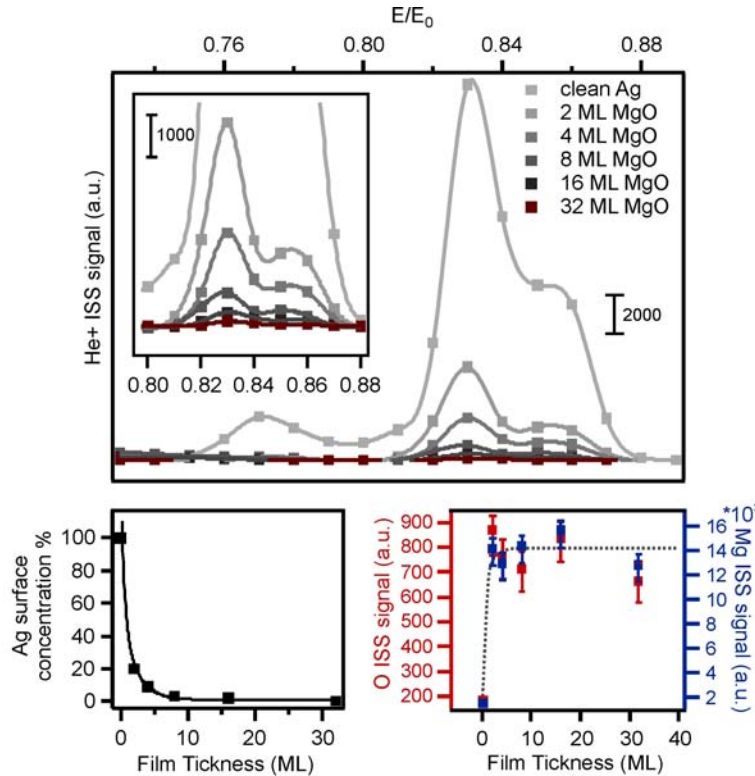


Figure 5.8.: He$^+$ ISS spectra of MgO(001)/Ag(001) films of different thickness.
Top: Ag region corrected by a linear background. Bottom left: Nor-
malized Ag surface concentration as a function of MgO thickness.
Bottom right: O and Mg signals as a function of MgO thickness.

The ISS results were corroborated by XPS data measured at BESSY II
(Berlin)[1]. Figure 5.9 shows the Ag 3d region of a 20 ML MgO(001)/Ag(001)
sample before and after annealing to 850 K in comparison to the signal of clean
Ag. The measurements were carried out at extremely surface sensitive conditions
such that the outermost atomic layer was predominantly probed. Photoelectrons
were collected at grazing angle (80°) and the excitation energy (470 eV) was cho-
sen such that Ag 3d photoelectrons had a kinetic energy of about 100 eV, i.e.
a very low inelastic mean free path. From intensity analysis, the surface con-
centration of silver is estimated to be 0.3 - 3% on the 20 ML MgO(001)/Ag(001)

---

[1]These measurements were carried out in collaboration with Helmut Kuhlenbeck, Elena Pri-
morac, Osman Karslioglu and Hengshan Qiu (Fritz-Haber-Institut, Berlin)

sample. Its Ag $3d_{5/2}$ peak before and after annealing is located at the binding energy of metallic silver (368.3 eV), such that an electrical connection between bulk and surface Ag cannot be excluded.
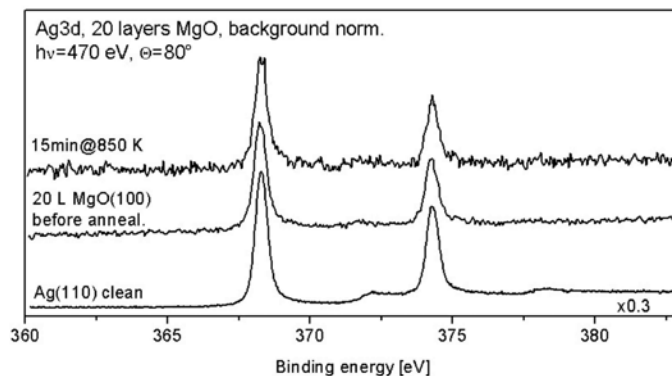


Figure 5.9.: XPS spectra of a 20 ML MgO/Ag(001) before and after annealing compared to the spectrum of a clean Ag(100) surface measured at BESSY II, Berlin (measurement at grazing angle, photon energy = 470 eV ).

## Dissolution of Thin MgO Films

Since from literature, the role of pH on the stability of MgO had become apparent, the stability of 20 ML MgO/Ag(001) thin films was tested in solutions of different pH. Freshly prepared films were exposed to Millipore water whose pH had been adjusted by NaOH and HCl. The films were characterized by AES before and after exposure (see figure 5.10) using the calibration described in section 5.3.1 for quantitative analysis.

Figure 5.11 a) summarizes the the dissolution behaviour for pH 2, pH 7 and pH 12 in the course of 20 min exposure. For pH 2, only a lower limit of the dissolution rate could be assigned, since after 5 seconds the film was completely dissolved. This time span is, however, the minimum exposure period which could be realized with acceptable certainty. At pH 7, intermediate rates were observed, such that the film was dissolved after about 40 sec. At pH 12, at the PZC of MgO, the films were most stable. Figure 5.11 b) shows data obtained from a long-term exposure (90 min) of a 20 ML MgO/Ag(001) film to a pH 12 solution. After an initial period of fast dissolution, the film exhibits long-term stability which indicates that after some time, the surface is at equilibrium in solution such that a stable surface state is reached.
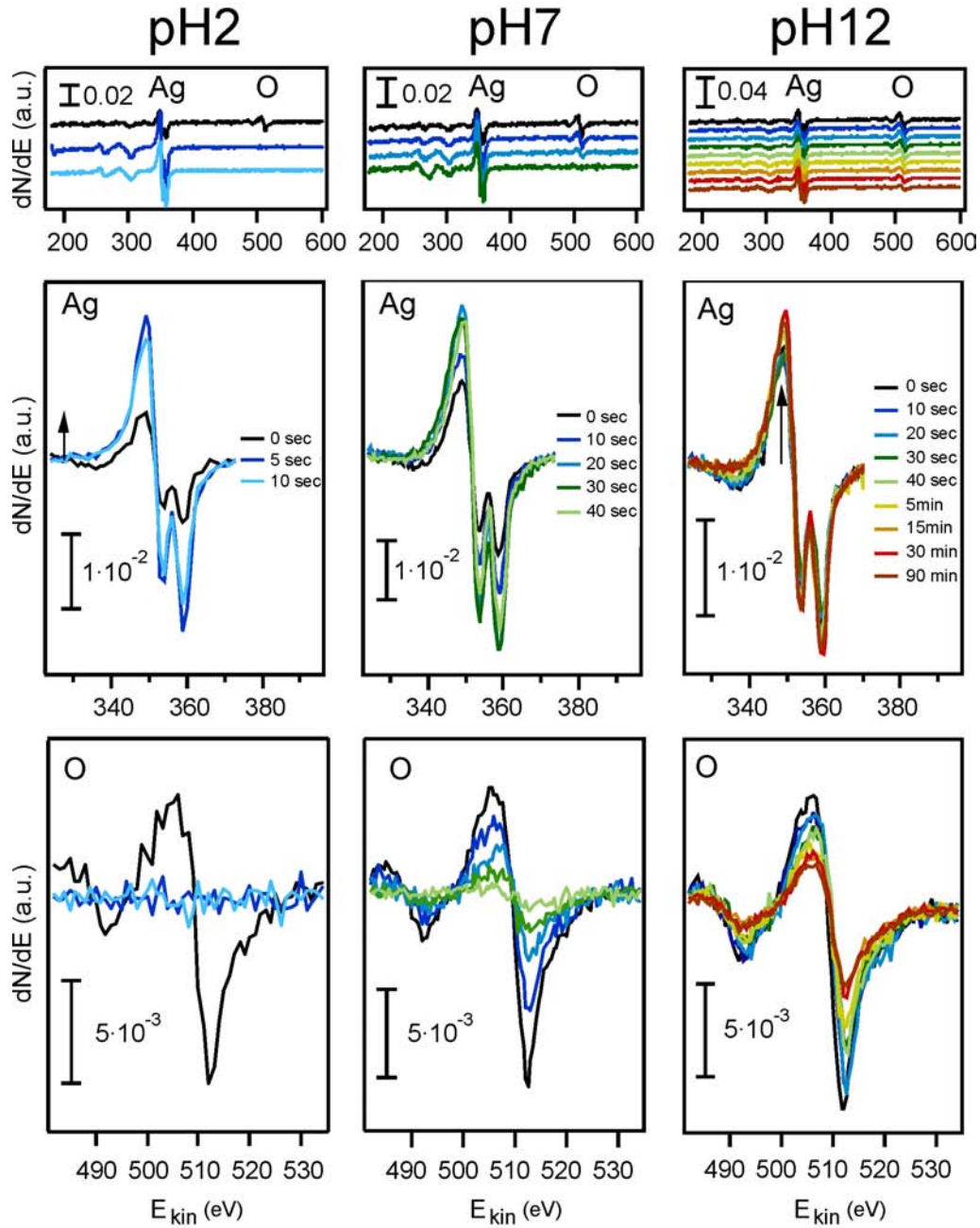
Figure 5.10.: Auger spectra of stepwise dissolution of two 20 ML MgO/Ag(001) samples at pH 2 (left) and pH 7 (center) and pH 12 (right).
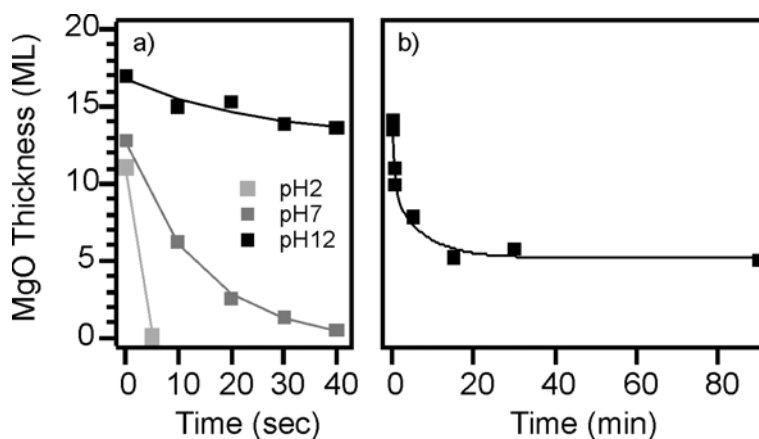
Figure 5.11.: Dissolution of 20 ML MgO/Ag(001) films - quantitative analysis of AES data. a) Short - term dissolution at pH 2, pH 7 and pH 12. b) Long - term dissolution at pH 12.

The initial dissolution rates calculated from figure 5.11 are: $4.1 \cdot 10^{-9}\,\mathrm{mol \cdot cm^{-2} \cdot s^{-1}}$ (pH 2), $9.7 \cdot 10^{-10}\,\mathrm{mol \cdot cm^{-2} \cdot s^{-1}}$ (pH 7), and $1.4 \cdot 10^{-10}\,\mathrm{mol \cdot cm^{-2} \cdot s^{-1}}$ (pH 12). These values are in the range of MgO dissolution rates reported previously [178, 177, 194, 175]. The deceleration of dissolution during long - term exposure to alkaline solutions is compatible with the formation of a brucite $(\mathrm{Mg(OH)_2})$ - like surface layer on MgO, which inhibits dissolution [178]. For comparison, reported dissolution rates for brucite at pH 12 are in the range of $10^{-14}\,\mathrm{mol \cdot cm^{-2} \cdot s^{-1}}$ [195].

From the results presented above it is clear that any catalyst preparation study with thin MgO films as used in the present study must be carried out with strongly alkaline precursor solutions in order to avoid complete dissolution of the MgO substrate during the precursor adsorption process. The acidic $\mathrm{PdCl_2}$ precursor solution was, therefore, hydrolized by adding NaOH, and care was taken to avoid precipitation of $\mathrm{Pd(OH)_2}$ during the hydrolysis step. At pH 12, which was set for all precursor solutions used in this study, the predominant Pd species in solution are $\mathrm{Pd(OH)_4^{2-}}$ complexes [169].

### 5.3.2. LPD of Pd on MgO Thin Films

**Initial Tests - Residues and Surface Roughness**

Besides $\mathrm{Pd(OH)_4^{2-}}$ complexes, the LPD precursor solution contained chlorine and sodium ions. Both ions constitute potential surface contaminants which might affect the structural and chemical properties of the final catalyst. Chlorine is particularly undesirable, since it evidently changes the metal particle dispersion and binding strength of adsorbates [196, 197, 198, 199]. Our aim was, however, to simplify the system as far as possible and rule these influences out. Without the application of a cleaning step after deposition (20 ML MgO/Ag(001), 5 mM $\mathrm{Pd^{2+}}$, 60 min), a large chlorine signal was detected by AES (with the $\mathrm{Cl}_{LVV}$ peak at 181 eV) on our samples and remained stable upon heating up to 600 K (see figure
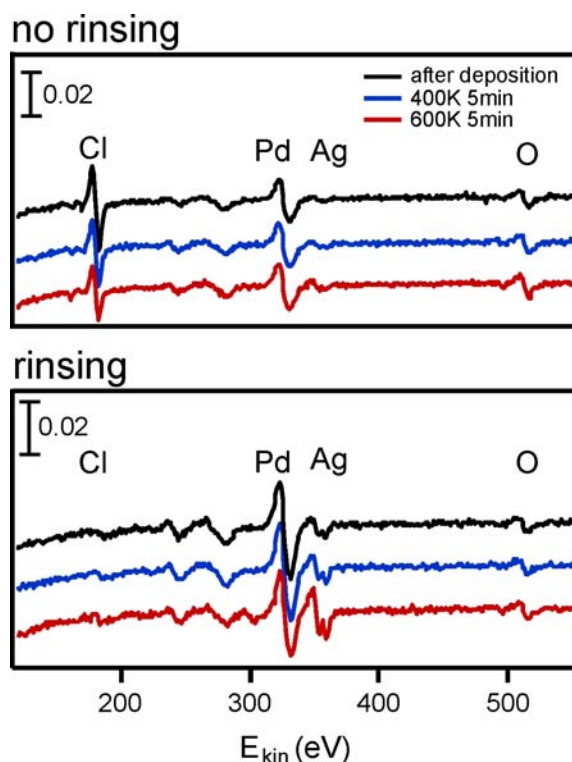
Figure 5.12.: Effect of rinsing after LPD deposition of Pd on a 20 ML MgO/Ag(001) film. Top: Deposition of 5 mM PdCl$_2$ for 60 min at pH 12. Bottom: Deposition of 5 mM PdCl$_2$ for 10 min at pH 12 and subsequent rinsing with blank solution (0.01 M NaOH, pH 12).

5.12, top). In contrast, chlorine was barely detectable after rinsing a sample with 0.01 M NaOH blank solution (pH 12) after deposition (20 ML MgO/Ag(001), 5 mM Pd$^{+2}$, 10 min; see figure 5.12, bottom). To exclude effects due to chlorine on the properties of the final catalyst, the samples were rinsed with 3 ml Millipore water after deposition in following experiments. In subsequent XPS control scans of the Cl 2p and the Na 1s regions, neither chlorine nor sodium were detected.

The chemical modifications of the film, which were induced by deposition and subsequent annealing, were documented by XPS. Figure 5.13 shows the O 1s region of a 60 ML MgO/Ag(001) sample before and after LPD of Pd (5 min, 0.5 mM Pd$^{+2}$) as well as after annealing to 710 K. The pristine films exhibits an O 1s peak at 530.5 eV. Strong chemical modifications are induced by exposing the sample to the aqueous solution. The main peak shifts by -0.5 eV to 530.0 eV and an additional shoulder evolves at 531.4 eV which indicates partial hydroxylation of the surface. The changes can be reversed by annealing to 710 K. Thermal decomposition of the hydroxyl groups is indicated by the absence of the shoulder at 531.4 eV.
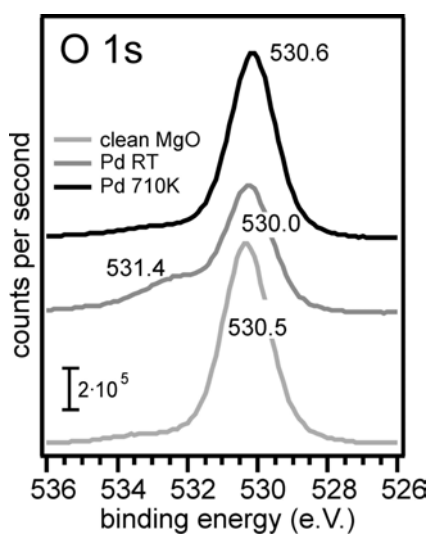
Figure 5.13.: XPS O 1s region of a 60 ML MgO/Ag(001) sample (i) in the pristine state, (ii) after LPD of Pd (5 min 0.5 mM Pd) and (iii) after subsequent annealing to 710 K.

LEED was used to monitor structural changes of the surface in the course of Pd deposition (see figure 5.14). The periodicity of the Ag(001) pattern remained after the deposition of 60 ML MgO. However, the LEED spots became more blurry indicating that the MgO(001) was less ordered than the Ag(001) substrate. After LPD of 1 mM $Pd^{+2}$ (pH 12) for 5 min - which corresponds to about 0.4 ML Pd - the surface exhibited no LEED pattern any more. This is most likely due to the irregular arrangement of Pd precursor complexes on the surface and the strong roughening of MgO upon exposure to ambient conditions. A faint MgO pattern could be restored after annealing to 710 K (see figure 5.14). Whereas in XPS the modifications of the support induced by LPD seem reversible, LEED indicates that the reordering after the thermal decomposition of OH groups is incomplete.
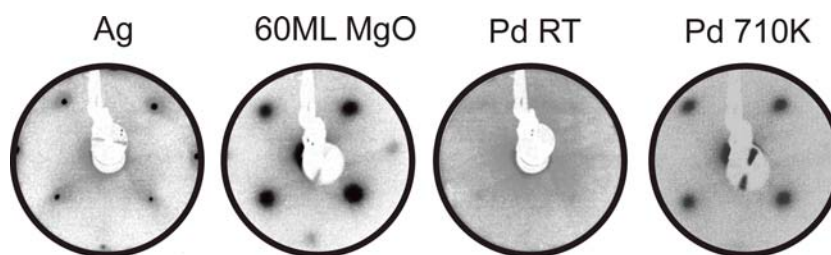


Figure 5.14.: LEED patterns from left to right: (i) clean Ag(001), (ii) 60 ML MgO(001)/Ag(001), (iii) 60 ML MgO(001)/Ag(001) after LPD of Pd (5 min, 1 mM $Pd^{+2}$), (iv) the previous sample after annealing to 710K.

**Pd Deposition on Ultrathin MgO Films**

Initial Pd deposition experiments were carried out with ultrathin films in order to allow the morphology of the resulting surfaces to be examined with STM. Figure 5.15 a) and b) show representative STM images of a 5 ML MgO/Ag(001) sample after LPD of 1 mM $Pd^{+2}$ for 5 min and subsequent annealing to 600 K.

The larger scale image (figure 5.15 a), 160 nm × 110 nm) displays a rough surface with morphological features in the range of 10 nm in diameter. This structure is clearly different from pristine MgO(001) thin films which is illustrated by a comparison to a 2 ML MgO(001)/Ag(001) sample prepared by PVD and imaged in UHV [200] (figure 5.15, c)). The increased roughness is a consequence of the structural modifications during the initial partial dissolution of the MgO surface upon exposure to the alkaline precursor solution. Although protrusions with different contrast are observed, a distinction between MgO - related features and Pd nanoparticles is not obvious from figure 5.15 a). However, on a smaller scale (figure 5.15, b); 100 nm × 60 nm), the distinction between support and Pd nanoparticles becomes more evident. Here, the brighter protrusions, which are assigned to Pd nanoparticles, can clearly be differentiated from the rough support. A few darker spots observed in this image are indicative of small holes down to the Ag(001) substrate. Taking tip convolution effects into account, the diameter of the Pd particles can be estimated to be about 3 nm.
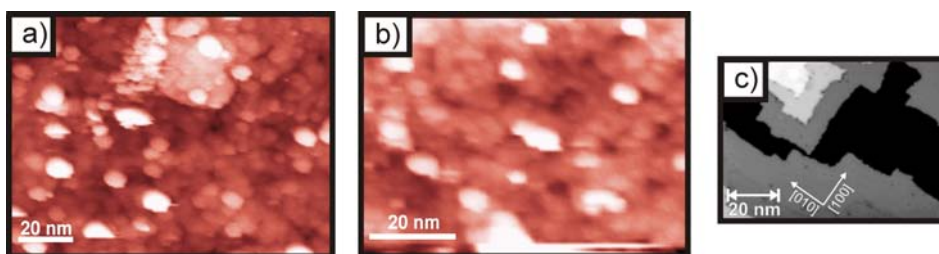


Figure 5.15.: STM images measured in air of a 5 ML MgO/Ag(001) sample after LPD of 1 mM $Pd^+$ for 5 min and subsequent annealing to 600 K. a) 160 nm × 110 nm. b) 100 nm × 60 nm. Tunneling conditions: $i_t = 100$ pA, $U_t = 100$ mV). Figure c) shows for comparison a 2 ML MgO sample prepared in by PVD and imaged in UHV (from [200]).

In order to obtain chemical information about the processes of Pd nanoparticle formation on the 5 ML MgO/Ag(001) sample, a similar preparation as the one described above was analyzed with XPS. The clean film exhibits an O 1s photoemission peak at 529.5 eV binding energy which is typical for a thin, supported MgO film (figure 5.16, top left) [126]. This signal gets strongly attenuated upon adsorption of the Pd precursor from aqueous solution. In addition, a shoulder appears at the high binding energy side of this peak (532 eV), which can be attributed to the presence of hydroxyls. Note that the Pd 3p emission is in the same binding energy range as the O 1s emission. Because of the small concentration of Pd on this surface, the shoulder at 532 eV originates almost entirely from hydroxyl species on the MgO surface.

The corresponding Pd 3d spectrum (figure 5.16, bottom) displays the typical Pd 3d doublet structure with a separation of 5.3 eV between the Pd 3d$_{5/2}$ and Pd 3d$_{3/2}$ states. The individual components exhibit an additional fine structure, pointing to the presence of at least two chemically different Pd species with Pd 3d$_{5/2}$ binding energies of 337.3 eV and 335.2 eV, respectively. The high binding

energy component can be assigned to adsorbed precursor complexes of oxidic (hydroxidic) nature, whereas the binding energy of the second component is compatible with the presence of metallic Pd. Upon heating to 400 K, partial decomposition of the oxidic precursor into metallic Pd is observed, which is complete after further heating to 600 K. In addition, this heat treatment leads to dehydroxylation of the MgO surface, seen by the disappearance of the shoulder at 532 eV binding in the O 1s region (figure 5.16, top left). The integrated area of the Pd 3d signals does not change for samples annealed up to 600 K. This means that no Pd is lost during the first annealing steps. However, the peak intensity of the Pd 3d signal strongly decreases following further heating to 710 K. The O 1s signal of the MgO film is only half as intense after the final annealing step as compared to the initial clean MgO film. Correspondingly, an increase of the Ag 3d signal intensity is observed (figure 5.16, top right).

The XPS data provide further support for the assignment of the bright protrusions observed in the STM image (figure 5.15, b)) to metallic Pd nanoparticles. However, these results also indicate that there is a non-negligible interaction of Pd with the Ag(001) support: The strong diminishment of the Pd 3d signal upon annealing to 710 K likely results from diffusion of Pd into the Ag bulk through holes in the MgO film, which were created during exposure to the precursor solution. Likewise, the presence of metallic Pd on the non-annealed sample can be ascribed to the direct adsorption and decomposition of Pd precursor complexes on partially exposed Ag(001) support. This result is in line with our previous observation that at 5 ML nominal thickness of thin MgO films, Ag is still exposed at the surface with an estimated concentration of about 7-8 % (see figure 5.8, bottom left). In addition, a considerable fraction of the MgO substrate is expected to be dissolved after exposure to the alkaline precursor solution, reducing the film thickness even further.

## Pd Deposition on Thick MgO Films

**Calibration of Pd Loading** In order to avoid any contribution from the Ag(001) substrate during the precursor deposition and decomposition stages, the following experiments were performed with nominally 60 ML thick MgO films. Because STM cannot be applied to MgO films of this thickness, XPS was used for the quantification of Pd loading from LPD. The peak area integral of the Pd 3d region was calibrated using Pd/MgO(001)/Ag(001) samples prepared by PVD as a reference (figure 5.17, c)). In figure 5.17, d), the Pd loadings for LPD experiments using different exposure times and $Pd^{+2}$ concentrations are summarized. The plot illustrates, that the Pd loading is correlated in an approximately linear manner to the precursor concentration within the time range investigated here (1-20 min). Longer deposition times also lead to an increase of loading, but low numbers of experiments and short deposition times prevent more specific conclusions about the type of correlation. Long-term deposition experiments could give further insight into the loading behaviour over time.
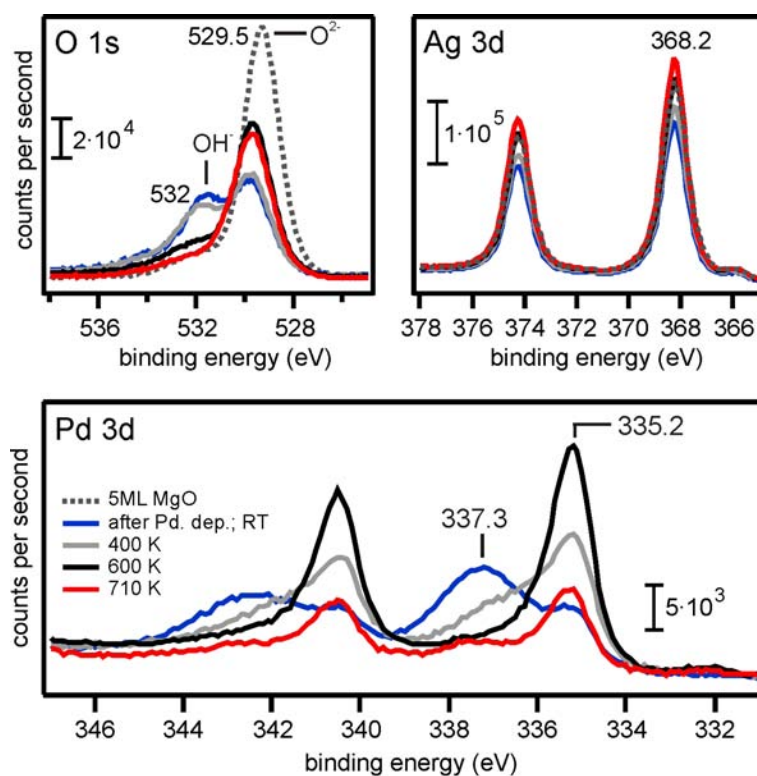
Figure 5.16.: XP spectra of a 5 ML MgO/Ag(001) after Pd deposition (0.5 mM Pd$^{+2}$, 5 min) and subsequent annealing to 400 K, 600 K and 710 K.

Table 5.2 lists the Pd loadings for the concentrations applied in this measurement series and - based on these values - the corresponding Pd loadings for a typical Pd-MgO powder catalyst in weight %, calculated with the assumption that its surface area is 40 m$^2$/g [157, 160].

A closer look at the Pd 3d photoelectron regions of both PVD and LPD samples directly after deposition shows chemical differences between samples of similar loading (figure 5.17 a), b)). By trend, the LPD samples exhibit more oxidized Pd compared to the PVD samples. This reflects the fact that the Pd(OH)$_4^{2-}$ precursor comprises Pd$^{2+}$ cations whereas in PVD, metallic Pd is deposited. Furthermore, the Pd 3d$_{5/2}$ line of LPD samples shifts to higher values for increased loadings (from 337.0,eV for 0.08 ML Pd to 337.6 eV for 1.3 ML Pd). For low loadings, precursor complexes bound to the support will account for most of the signal, whereas it should be increasingly dominated by multilayer deposits of the complexes when the loading in increased. It seems, therefore, that the interaction with the support may lead to partial reduction of the adsorbed precursors.

PVD samples show an opposite behaviour regarding the binding energy shift. Here, the Pd 3d$_{5/2}$ position tends to decrease for higher loadings (336.6 eV for 0.07 ML Pd to 335.6 eV for 1.2 ML Pd). This can be explained by the increasingly
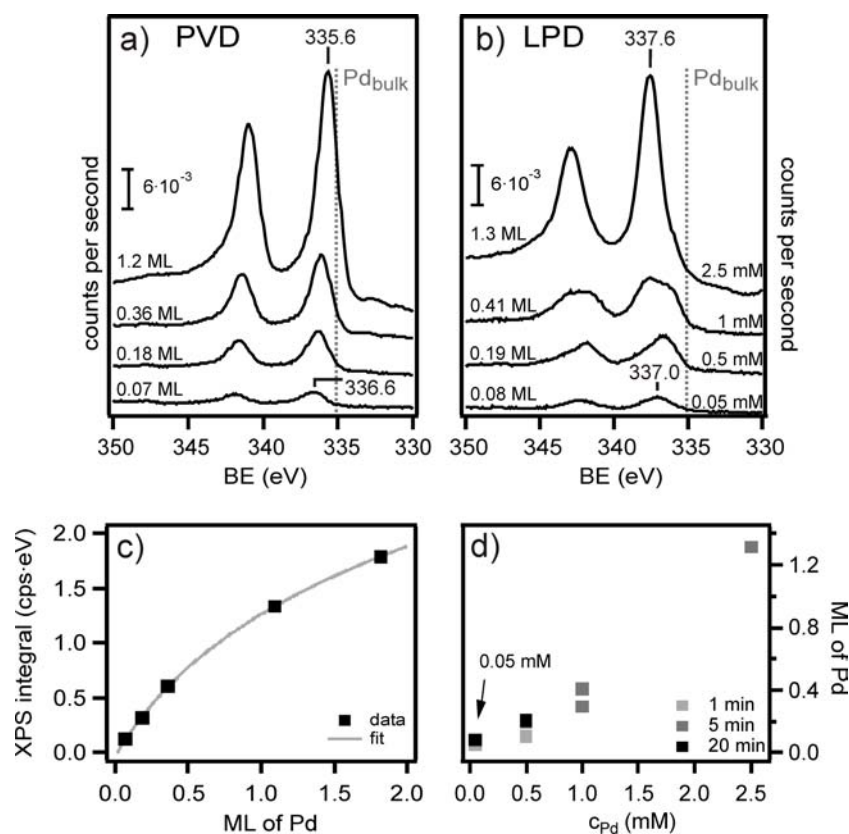
Figure 5.17.: Quantification of Pd loading by XPS: a) Pd 3d region of Pd/MgO(001)/Ag(001) samples prepared by PVD. b) Pd 3d region of Pd‑MgO/Ag(001) samples prepared by LPD (deposition time = 5 min). c) Calibration curve: Pd 3d peak areas from PVD samples and exponential fit. d) Pd loading after LPD on 60 ML MgO/Ag(001) as a function of precursor concentration and deposition time.

metallic character of larger metal particles. Furthermore, charging and band bending contributions of the support have a stronger influence on small particles.

Since absolute Pd loadings could be determined, assumptions about the absolute particle size can be made based on results of previous studies.. Even though there is no Pd particle size study for the MgO/Ag(001) system in UHV, Pd‑alumina/NiAl(001)[201] and Pd‑$Fe_3O_4$/Pt(111) [202] studies from our group and a study from Goodman's group on Pd‑MgO/Mo(001) [141] can be used as a reference. These reports suggest that particle sizes of about 1 nm can be expected for a loading of 0.05 ML, obtained by using 0.05 mM $Pd^{2+}$ precursor solutions. Roughly 3 nm sized particles correspond to a coverage of 0.4 ML (from a 1 mM $Pd^{2+}$ precursor solution) and up to 5 nm sized particles to a coverage of 1 ML (from a 2.5 mM $Pd^{2+}$ precursor solution). Similar amounts of CO desorption for similar Pd loadings in TPD measurements shown in section 5.3.3 justify the comparison of LPD and UHV prepared samples.

| Pd$^{2+}$ concentration (mM) figure 5.17, b) | Nominal Pd loading (ML) figure 5.17, b) | Pd loading wt. % |
|---|---|---|
| 0.05 | 0.05 | 0.5 |
| 0.5 | 0.22 | 2.3 |
| 1 | 0.41 | 4.3 |
| 2.5 | 1.05 | 11.0 |

Table 5.2.: Nominal Pd coverage after LPD on 60 ML MgO/Ag(001)(pH 12, 5 min exposure time, different Pd$^{2+}$ concentrations) and calculated Pd loading on a typical Pd - MgO model catalyst with a surface area of 40 m$^2$/g.

**Precursor Decomposition - High Loadings**   The thermal decomposition of Pd precursor complexes after LPD was studied in more detail using XPS for a sample prepared by exposing 60 ML MgO/Ag(001) to a 1 mM Pd$^{+2}$ for 5 min which results in a Pd loading of about 0.4 ML (figure 5.18 a)). The spectrum of the raw catalyst can be decomposed into two Pd 3d doublets with Pd 3d$_{5/2}$ binding energies of 337.8 and 336.2 eV, respectively. Upon heating to 400 K, the high binding energy component converts almost completely into a Pd species exhibiting a Pd 3d$_{5/2}$ binding energy of 336.0 eV. Further heating to 600 K and 710 K leads to a gradual reduction which is reflected by a - 0.2 eV shift after each step up to a final value of 335.6 eV. The absence of a Pd 3d$_{5/2}$ component at 335.2 eV, which had been observed on a 5 ML MgO/Ag(001) support (see figure 5.16) confirms the previous assumption about the active role of Ag in the decomposition of the Pd precursor (see section 5.3.2)

The Pd 3d photoelectron spectra of figure 5.18 a) are qualitatively similar to those reported in a previous study of Pd deposition from alkaline precursor solution on Fe$_3$O$_4$(111) by our group [163]. In agreement with this study and with reported binding energies of hydroxidic and oxidic Pd species [203, 204, 205, 206], Pd - hydroxide precursor complexes bind to the MgO surface during exposure to the alkaline Pd$^{2+}$ precursor solution, giving rise to the Pd species with a Pd 3d$_{5/2}$ binding energy of 337.8 eV. Because the MgO surface is expected to be essentially uncharged at the employed pH, the initial interaction of the precursor with the support surface can be described as hydrolytic interaction of Pd(OH)$_4^{2-}$ complexes present in solution with surface hydroxyls. The adsorbed Pd - hydroxide precursor complexes easily decompose at slightly elevated temperature (400 K) into partially oxidized Pd particles exhibiting a Pd 3d$_{5/2}$ binding energy of 336.0 eV. A shift to 335.6 eV after a thermal treatment at 710 K is indicative for further decomposition, resulting in metallic Pd nanoparticles. This interpretation is corroborated by the simultaneous appearance of weak satellite peaks at 342 eV and 347 eV, which are due to energy losses resulting from plasmon
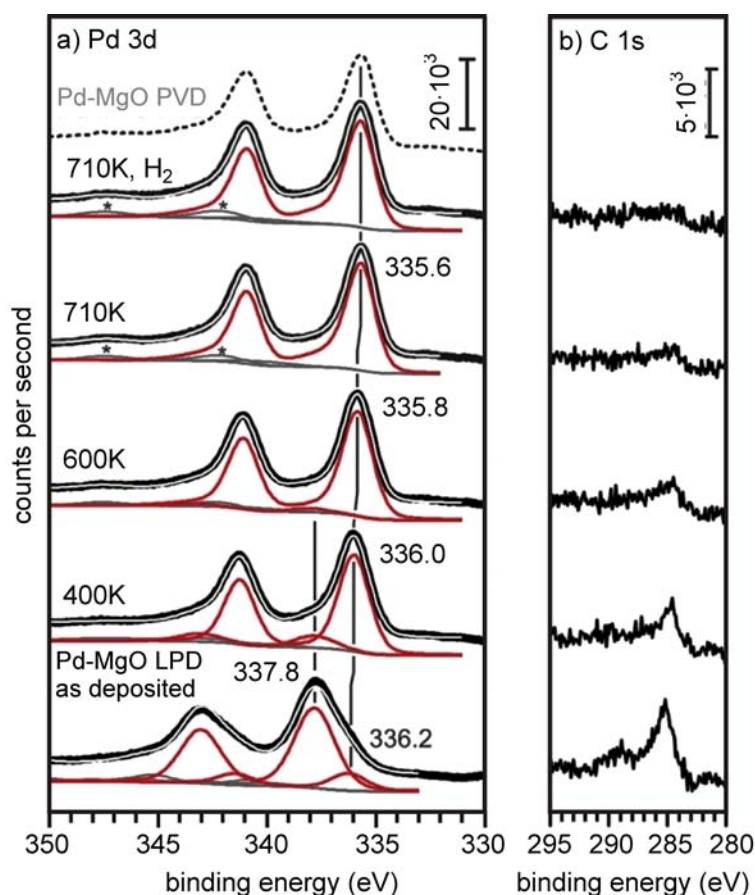
Figure 5.18.: LPD ($5\,min\,1\,mM\,Pd^{2+}$) on $60\,ML\,MgO/Ag(001)$ analyzed by XPS. a) Pd 3d region. b) C 1s region.

excitation in metallic Pd systems [207], as well as by the fact that the XP spectrum remains essentially unchanged following a subsequent reductive treatment in $H_2$ atmosphere (figure 5.18 a), topmost spectrum).

The $Pd\,3d_{5/2}$ binding energy of $335.6\,eV$ recorded for metallic Pd nanoparticles on our $60\,ML\,MgO(001)/Ag(001)$ films is $0.4\,eV$ higher than that of bulk‑like metallic Pd ($335.1\,eV$) [25], and considerably higher than $334.4\,eV$, which has been taken as indication for electron‑rich Pd particles, recorded by Claus *et al.* for a Pd‑MgO powder sample [157]. Because the MgO films employed in the present study are relatively thick (nominally $60\,ML$), charging effects could potentially lead to a shift to higher binding energy. However, this possibility is excluded based on the similarity of the C 1s binding energies on the $60\,ML\,MgO$ sample and on the $5\,ML\,MgO$ sample, where charging effects are negligible.

Alternatively, the binding energy shift could arise from (i) reduced final state screening of the core hole created during the photoemission process in the small Pd particles on the insulating support (final state effect), (ii) initial state contributions such as charge transfer between the MgO support and the Pd particles or lattice contraction in small Pd particles, or (iii) some combination of (i) and (ii). Auger parameter analysis is a potential method to discriminate between those

effects [207, 208, 209]. We performed a preliminary Auger parameter analysis for this sample. The raw catalyst was annealed to 710 K and finally heated in reducing atmosphere (710 K in $1 \cdot 10^{-6}$ mbar $H_2$). After each step, the Pd $L_3M_{45}M_{45}$ Auger emission and the Pd 3d photoemssion was recorded (see figure 5.19). The Auger analysis of this data yields a shift of -0.1 eV of extra-atomic relaxation energy and -2.1 eV of the core level position for the raw catalyst with respect to a bulk metallic Pd reference sample [25, 210]. The shifts for the reduced sample (the peak positions were equal for thermal and chemical reduction in $H_2$ atmosphere), are -0.5 eV and 0.0 eV, respectively. In summary, our analysis suggests that the raw catalyst exhibits oxidic Pd whereas the reduced Pd particles are essentially neutral and the observed 0.4 eV shift to higher binding energy is caused by a reduced final state screening in the small Pd particles.

This interpretation is corroborated by the fact that the Pd $3d_{5/2}$ binding energy approaches 335.2 eV, that is, bulk-like behavior, in samples with higher Pd coverage that contain larger Pd particles. For example, on a sample prepared by exposure of MgO to 2.5 mM $Pd^{2+}$ precursor solution, which results in a coverage of about 1 ML Pd, the Pd $3d_{5/2}$ binding energy is 335.25 eV after thermal treatment at 710 K.
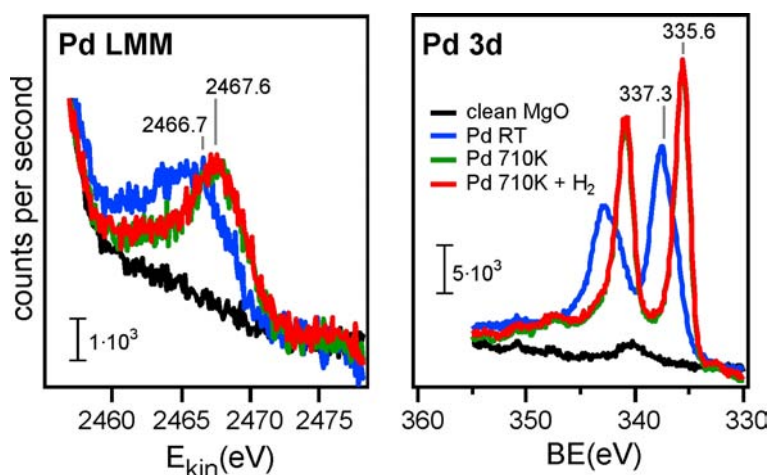


Figure 5.19.: Pd $L_3M_{45}M_{45}$ Auger and Pd 3d photoemission spectra of an LPD prepared Pd-MgO/Ag(001) catalyst for Auger parameter analysis (1 mM $Pd^{2+}$ was deposited at pH 12 for 5 min on a 60 ML MgO/Ag(001) film).

Figure 5.18 b) shows the C 1s regions of corresponding measurements during the annealing series. Typically, there are both carbonaceous species (289-291.5 eV) and adventitous carbon (284.1-285.5 eV) present on the surface after LPD. It is important to note that in this measurement all carbon contaminations could be effectively removed. In general, during annealing, carbonates can be easily removed whereas the removal of adventitious carbon was not always equally effective as will be explained in more detail below.

**Precursor Decomposition - Low Loadings**   As shown in section 5.3.2, the precursor concentration has a large impact on the Pd loading. However, not only the loading is of interest in catalyst preparation, but the chemical state as well. For example, for total oxidation processes like methane combustion, PdO has been proposed to be the most active phase [211, 212, 213], whereas selective partial oxidation requires a more reduced state of Pd [214].

Figure 5.20 shows Pd 3d and C 1s photoelectron spectra of Pd - MgO/Ag(001) samples prepared by LPD using $0.5\,mM$ $Pd^{+2}$ with deposition times of $1\,min$, $5\,min$ and $20\,min$. All samples were annealed to $400\,K$, $600\,K$ and $710\,K$. After each heating step, photoelectron spectra were recorded.



Figure 5.20.: Variation of deposition time: XP Pd 3d (left) and C 1s (right) spectra of Pd - MgO/Ag(001) samples prepared by LPD ($0.5\,mM$ $Pd^{+}$ for 1, 5 and 20 minutes) which were annealed to $400\,K$, $600\,K$ and $710\,K$.

Directly after deposition, all samples show a broad Pd 3d doublet characteristic for the precursor with its Pd $3d_{5/2}$ peak centered around $336.6 - 337.1\,eV$. During the following annealing steps, the broad Pd doublet splits into two sharper doublets reflecting the decomposition of the precursor and conversion to oxidic and

metallic Pd at $Pd\,3d_{5/2}$ binding energies of $337.9\,eV$ and $335.8\,eV$, respectively, in different ratios depending on deposition time. Among the samples, the one prepared by 1 min. exposure to precursor solution reaches a stable surface state fastest, i.e. already after heating to 600 K. Interestingly, this state is characterized by almost exclusively oxidic Pd species, which are very stable and do not decompose into metallic Pd during heat treatment at higher temperature. By contrast, conversion of oxidic into metallic Pd species is observed at higher temperatures (710 K) for the samples prepared by 5 min. and 20 min. exposure, which exhibit higher Pd loadings relative to the 1 min. exposure sample. The last spectra, measured after annealing to 710 K for 20 min, show roughly equal amounts of oxidic Pd ($337.9\,eV$) for all samples, and an additional contribution of metallic Pd ($335.8\,eV$), the amount of which is correlated with the exposure time.

Plots of the C 1s region illustrate that after deposition, mainly adventitious carbon ($285.8\,eV$) and to some extent carbonates ($289.8\,eV$) are present on the surface. As in the case of high Pd loadings (see above), an annealing step to 600 K is sufficient to completely remove the carbon species. The Pd decomposition series shown in figure 5.20 differs vastly from what has been introduced in figure 5.18 as being a 'typical' decomposition behaviour and which holds for higher loadings. It is important to note that the highly stable oxidic Pd species was only observed for small loadings ($\leq 0.4\,ML$). On the one hand, this observation could be due to the fact that in case of high loadings, where most of the precursor is converted already after 400 K annealing, the much smaller oxidic contribution might simply be overseen. On the other hand, a self-promoted reduction process in larger particles could lead to a complete conversion of oxidic into metallic Pd species. Alternatively, the surface processes at the MgO/aqueous precursor interface might also have an impact on the stabilization of oxidic Pd species. By far the most changes to the MgO substrate occur within the first minutes of deposition, where the surface is out of equilibrium and the dissolution rate is highest (see figure 5.11). Precursor complexes might be incorporated into the subsurface in open pores or cracks when the deposition is interrupted at this stage, such that the embedding might contribute to stabilizing oxidic Pd.

## Influence of Carbon Impurities

Carbon is known to deactivate Pd catalysts [215]. Inactivation by coking, for example, is a common and considerable problem in industry. In some cases, however, the reactivity can also be enhanced by carbon, as for example for the selective oxidation of ethene and of vinyl acetate, where a near-surface modification of Pd metal with carbon seems to be most effective [216, 217]. In our LPD studies, carbon was a permanent byproduct upon exposure to ambient conditions. The results of the previous section have shown that annealing in UHV is sufficient to remove the carbon contaminations. However, additional experiments have shown that occasionally carbon could not be completely removed by

heating. The impact of residual carbon on Pd precursor decomposition will be discussed in this section.

Figure 5.21 shows an annealing series similar to figure 5.20 of the previous section, where it was concluded, that for low loadings ($\leq 0.4\,$ML), a particular amount of stable oxidic Pd remains present on the MgO surface after thermal treatment at $710\,$K. In the case of figure 5.21, the loadings are even lower (LPD using $0.05\,$mM Pd$^{+2}$) than in the case of figure 5.20 (LPD using $0.5\,$mM Pd$^{+2}$).

Therefore, a high abundance of oxidic Pd species is expected. Instead, one observes that only in the case of effective thermal carbon removal (figure 5.21, C 1s region, 1 min deposition time), a high amount of Pd remains oxidized after annealing to $710\,$K (figure 5.21, Pd 3d region, 1 min deposition time). In the cases of longer deposition times (5 and 20 min), part of the adventitious carbon (at about $286\,$eV) cannot be removed by heating in contrast to the carbonaceous species ($289.8\,$eV). In this case, more oxidic Pd is converted to metallic Pd at $710\,$K than in the absence of carbon.

Further experiments on the influence of carbon are shown in figure 5.22. Here, three experiments are compared that were carried out in an identical manner (LPD of 1 min $0.05\,$mM Pd$^{2+}$ on $60\,$ML MgO/Ag(001)), but independently on three different films. Directly after deposition, a significant amount of carbon was detected in all three cases. In analogy to previous experiments, both carbonaceous ($289.6\,$eV) and adventitious carbon ($285.0$-$285.5\,$eV) were detected on the surface. All carbonaceous species as well as most of the adventitious carbon could be removed in two cases (grey and black traces) upon heating to $600\,$K. In one experiment, however (red trace), a significant amount of adventitious carbon remained present even after annealing at $710\,$K for $20\,$min. At the same time, clear differences in the precursor decomposition can be observed. While in the case of effective carbon removal (grey, black) a highly oxidized Pd species is stable up to $710\,$K (as shown previously in figure 5.20), Pd is mainly reduced after such treatment if adventitious carbon remains present on the surface (red traces). However, differences in the precursor decomposition become apparent much earlier. Already after the $400\,$K step, the tendencies are visible.

Obviously, the question arises how variations of carbon loading and stability can be explained. All glass dishes used for LPD were cleaned by a wet chemical procedure prior to use (see section 5.2.2). Solutions were prepared just before LPD from freshly collected Millipore water. The exposure time of the sample to ambient air was minimized. The sample was taken out of the chamber at a maximum of $5\,$min before deposition and was reinserted into UHV immediately afterwards. Therefore, we assign the apparent randomness of carbon loading and stability to day-to-day fluctuations of the laboratory air composition. Sources of carbon are most likely hydrocarbons, but it might also originate from carbonate dissolved in the aqueous solution which is possibly embedded by precipitation of MgCO$_3$ (as discussed in section 5.1.4).

In order to test whether carbon enrichment is associated with Pd deposition, a control experiment was performed, where a $60\,$ML MgO film was exposed to blank solution, i.e. $0.01\,$M NaOH, pH 12 (blue traces in figure 5.22). Here, less
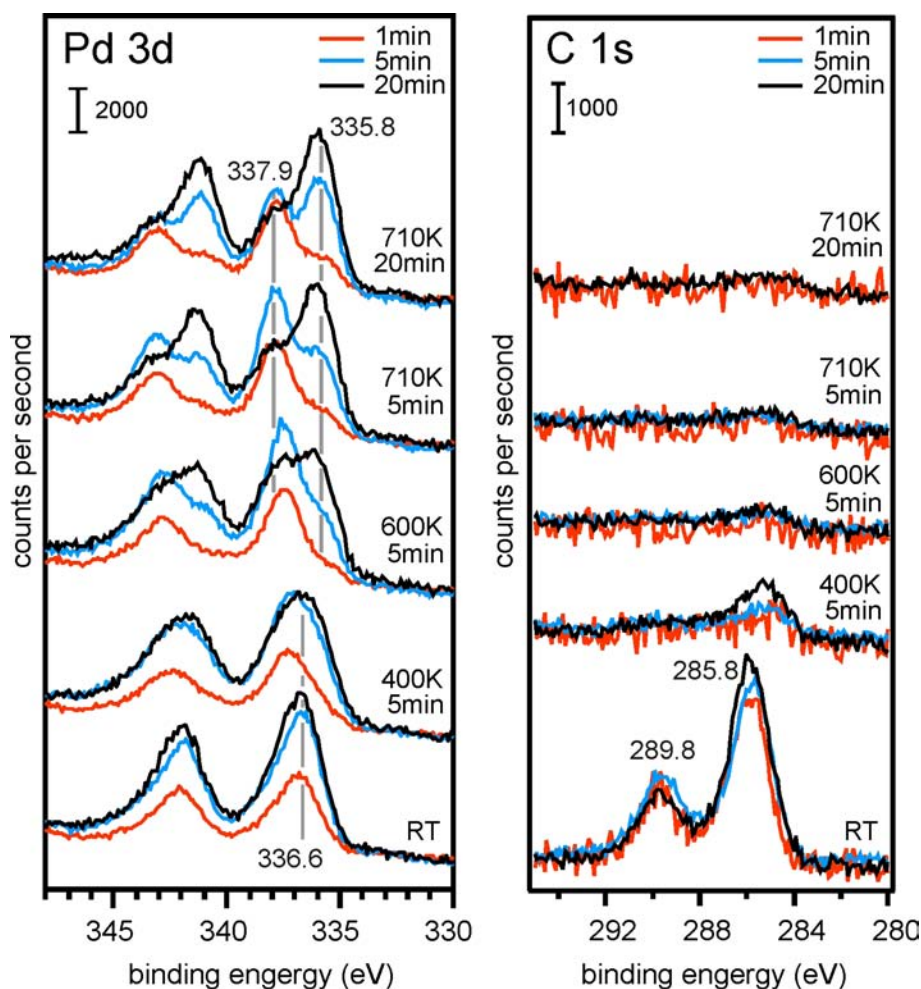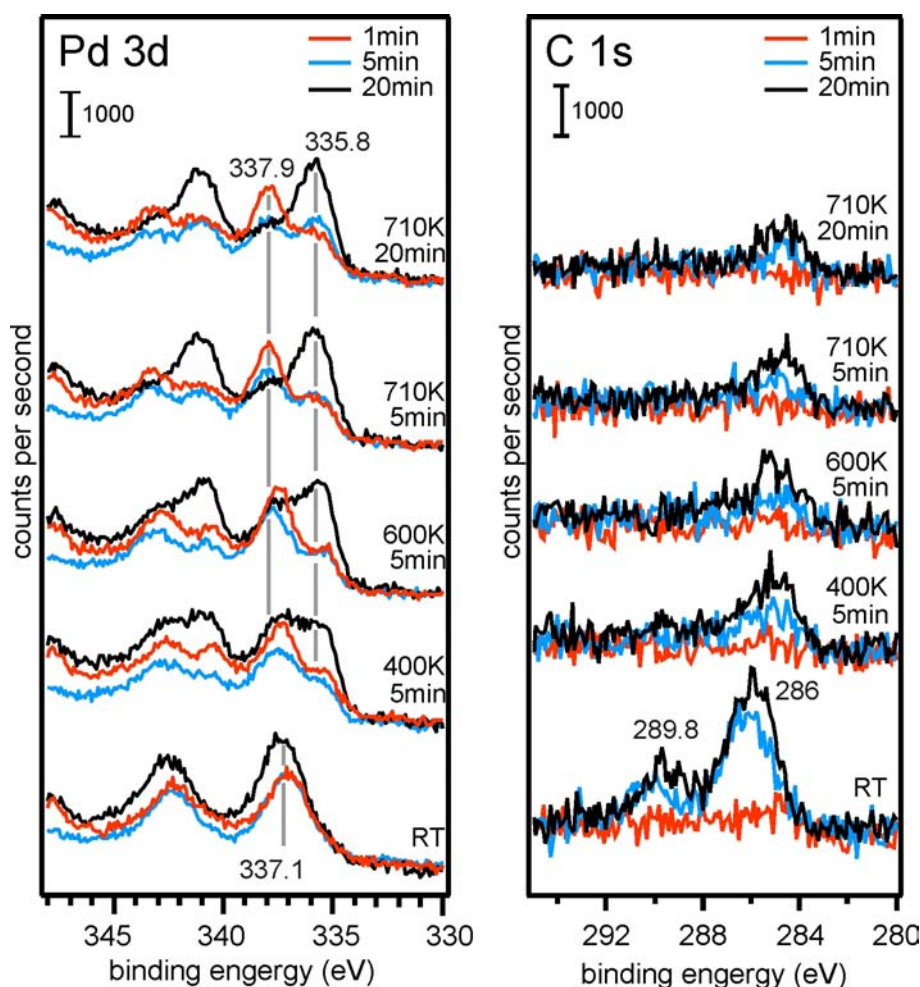
Figure 5.21.: Variation of deposition time: XP Pd 3d (left) and C 1s (right) spectra of Pd - MgO/Ag(001) samples prepared by LPD (0.05 mM Pd$^+$ for 1, 5 and 20 minutes) which were annealed to 400 K, 600 K and 710 K.

carbon is detected directly after exposure. Furthermore, carbon is removed after annealing at 600 K. We cannot draw general conclusions from this control, of course, since evidently the result might be subject to statistical fluctuations.

There is, however, a deviation compared to all LPD experiments which should be mentioned here. Both the carbonate peak and the adventitious carbon peak are roughly of equal size and exhibit similar thermal stability. In contrast, if Pd$^{+2}$ is present in solution, the adventitious carbon peak was always dominant and more stable upon heating. This indicates that the presence of Pd might play a role in the agglomeration of carbon during LPD and its stabilization during precursor decomposition. In the literature it has been reported, that $CO_2$ can dissociate at supported Pd nanoparticles [218]. It has also been observed that carbon can migrate into the Pd lattice. It forms a PdC$_x$ phase by occupying interstitial sites which leads to a wideing of the lattice parameter [219]. Therefore, it is conceivable that enhanced interaction between Pd and carbon stabilizes
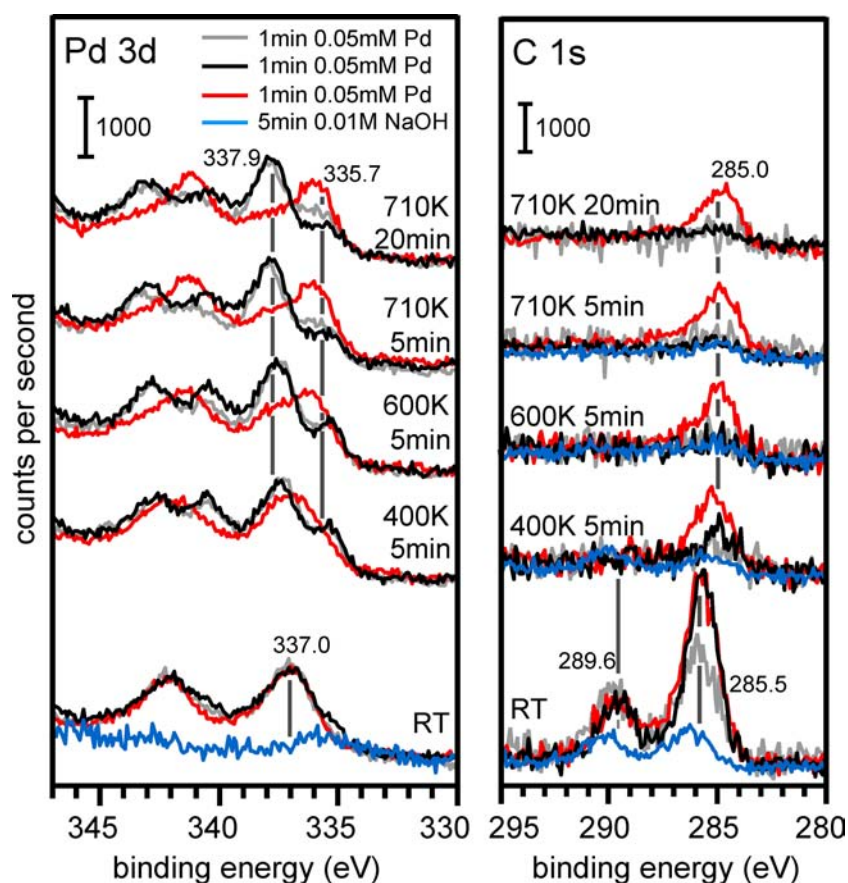
Figure 5.22.: Role of Carbon on reducibility of Pd investigated by XPS (left: Pd 3d region; right: C1s region). In three independent experiments (gray, black and red) with identical protocols, $50\,\mu$M Pd were deposited for $1\,$min on $60\,$ML MgO. Blue traces: Control experiment using blank solution ($5\,$min $0.01\,$M NaOH).

carbon on the surface. In summary, the results shown here illustrate how even small contaminations of carbon apparently affect the chemical state of Pd during precursor decomposition.

## Surface Pretreatment and Aging of Solution

So far, the chemical state of the final Pd catalyst was found to depend on a number of parameters such as deposition time, precursor concentration and carbon contamination. As mentioned earlier, the highly oxidized Pd species was found to be stable only at low concentrations and short deposition times in the absence of carbon.

Another aspect, which might affect the outcome of the final catalyst, is the age of the precursor solution. For all experiments in this work, the solution was usually prepared a few minutes prior to deposition. There was, however, a time uncertainty, i.e. the age of the solution could vary a couple of minutes in different

experiments. This might possibly change the carbon or Pd loading due chemical changes of the precursor complex in solution.

To shed more light on both questions, control experiments were carried out which are summarized in figure 5.23. Photoelectron spectra of both, the Pd 3d and the C 1s region are shown. For comparison, data obtained from a standard experiment without surface pretreatment and using a freshly prepared solution, is shown (figure 5.23, left). For all experiments, a 60 ML MgO/Ag(001) substrate was used and during LPD the sample was exposed for 1 min to 0.5 mM $Pd^{2+}$. To investigate the effect of a surface pretreatment, one MgO/Ag(001) film was first exposed to a blank solution (60 ML MgO/Ag(001), 4 min 0.01 M NaOH, pH 12) before Pd was deposited (figure 5.23, center). The influence of solution aging was tested on another film by applying a precursor solution, which had been prepared 2 hours prior to use (figure 5.23, right).

After deposition, the C 1s photoelectron spectra of all samples show a similar spectral shape and initial carbon loading. The Pd 3d region, however, shows differences in loading and the chemical state of Pd. In the control experiment, the Pd $3d_{5/2}$ peak is centered at around 336.7 eV. The pretreated sample, in contrast, exhibits a Pd $3d_{5/2}$ binding energy (338.6 eV) which is higher than for all other LPD experiments. As a result of the pretreatment, the precursor most likely 'sees' a surface which is changed in structure and OH functionalisation. This could lead to stronger binding and higher dispersion of the precursor resulting in higher binding energies for Pd. Pretreating the support with alkaline solution (pH 10) has, for example, been found to enhance the long-term stability and significantly increase the catalytic activity of a Au catalyst deposited on $TiO_2$ [220] which the authors attribute to the formation of strongly bound hydroxyl species. The aged solution sample exhibits a multicomponent Pd $3d_{5/2}$ feature which is roughly the sum of the control and the pretreated Pd 3d peaks. So this sample apparently comprises both, the 'normal' precursor deposit and some higher binding energy component. The latter might be a result of chemical modifications of the precursor complex in solution during aging.

After annealing to 710 K, Pd is reduced on both the pretreated sample (335.8 eV) as well as on the aged solution sample (335.8 eV), whereas on the standard sample Pd is mainly oxidized (337.8 eV). The C 1s region reveals, that at the same time, carbon is only fully removed from the standard sample. Therefore, the differences in reducibility of Pd can not unambiguously assigned to the pretreatment or solution aging, but might be affected by carbon contaminations.

In summary, the results show that the chemical state of the raw Pd catalyst is very sensitive to the state of the surface and the quality of the precursor solution.

### 5.3.3. Activity Towards CO Oxidation

At the final stage of this study, results on CO adsorption properties and catalytic activity towards CO oxidation of LPD-prepared Pd-MgO/Ag(001) catalysts were compared to those of corresponding samples prepared by PVD. On Pt group metals, CO can bind with the carbon atom facing towards the metal surface in an
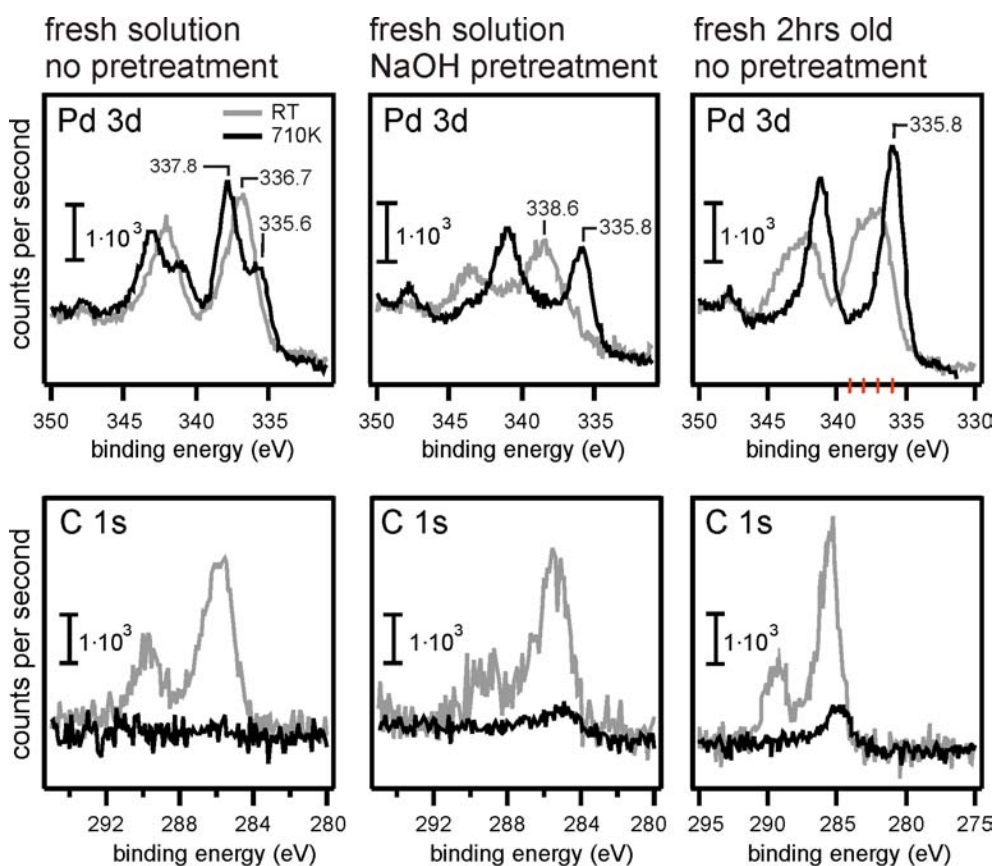
Figure 5.23.: Photoelectron spectra of Pd 3d (top) and C 1s (bottom) regions after LPD (1 min 0.5 mM $Pd^{2+}$ on 60 ML MgO/Ag(001)). Left: No pretreatment was applied and fresh precursor solution was used. Center: Prior to LPD of Pd, the sample was exposed for 4 min to a 0.01 M NaOH solution (pH 12); fresh precursor solution was used. Right: No pretreatment was applied; the precursor solution had aged 2 hours prior to LPD.

on-top, bridge or three fold hollow configuration. According to the Blyholder model [42], which describes the binding mechanism of CO on metals, the CO molecule donates electrons from its highest occupied molecular orbital $(5\sigma)$ to unoccupied $d$ orbitals in the metal. On the other hand, back donation from the metals occupied $d$ orbitals into the antibonding $2\pi^*$ occurs.

CO oxidation is one of the most simple and widely investigated model reactions. It is therefore considered as a benchmark reaction for chemical and catalytic properties [221] and allows to compare results to a broad range of existing studies. On noble metal surfaces, CO oxidation proceeds via the Langmuir-Hinshelwood (LH) mechanism [222, 223, 224, 225]. In the LH mechanism, both educts adsorb on the surface before they react and the product finally desorbs. The overall process

$$2\,CO_{gas} + O_{2,gas} \quad \leftrightarrow \quad 2\,CO_{2,gas}$$

can be split into several steps:

$$
\begin{aligned}
2\,CO_{gas} &\leftrightarrow 2\,CO_{ads}\\
O_{2,gas} &\leftrightarrow O_{2,ads}\\
O_{2,ads} &\leftrightarrow 2\,O_{ads}\\
2\,CO_{ads} + 2\,O_{ads} &\leftrightarrow 2\,CO_{2,ads}\\
2\,CO_{2,ads} &\leftrightarrow 2\,CO_{2,gas}
\end{aligned}
$$
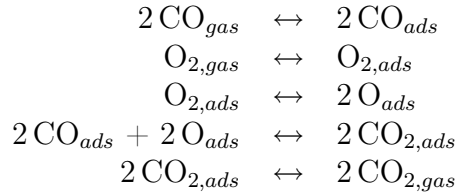
CO binds in a closely packed fashion on Pd which prevents oxygen adsorption. Therefore, the reaction is blocked if there is an excess of CO. Oxygen, on the other hand, adsorbs in a open layer which does still allow for CO to adsorb. Therefore, at low CO pressures, the reaction rate is proportional to the oxygen pressure and limited by CO adsorption.
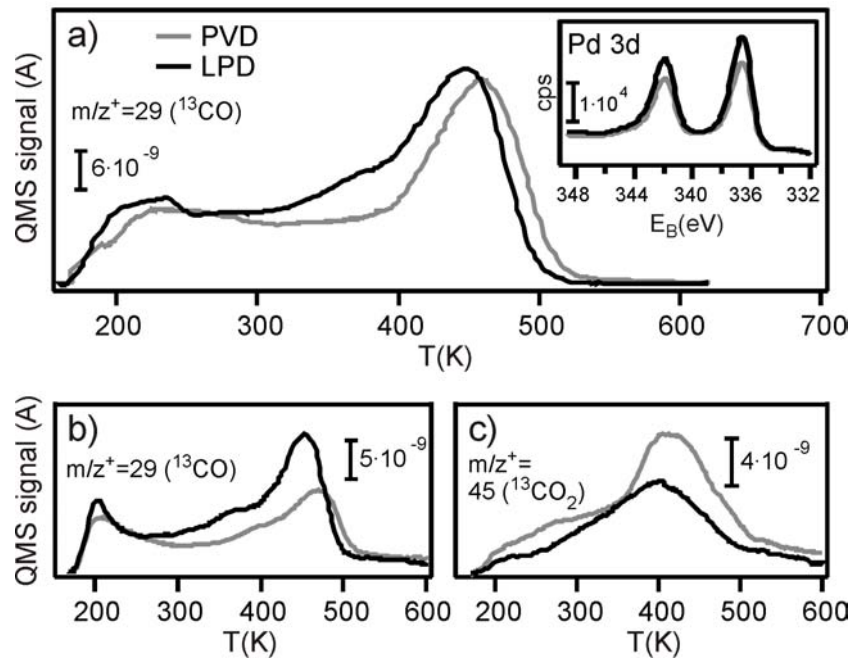


Figure 5.24.: TPD spectra ($2\,K/sec$) of Pd-LPD ($60\,ML$ MgO/Ag(001), $5\,min$ $1\,mM$ $Pd^{+2}$) and Pd-PVD ($60\,ML$ MgO(001)/Ag(001), $1\,Å$ Pd) samples. a) $^{13}CO$ desorption after a $0.2\,L$ $^{13}CO$ dose at $150\,K$. Inset: XPS Pd $3d$ region of LPD and PVD samples. b) $^{13}CO_2$ evolution after (i) a $2\,L$ $O_2$ dose at $400\,K$ and (ii) a $0.2\,L$ $^{13}CO$ dose at $150$.

Figure 5.24 shows TPD spectra of $^{13}CO$ desorption and $^{13}CO$ oxidation of an LPD ($60\,ML$ MgO/Ag(001), $5\,min$ $1\,mM$ $Pd^{+2}$) and a PVD ($60\,ML$

MgO(001)/Ag(001), 1 Å Pd) sample. Prior to CO oxidation measurements, the samples were exposed to an activation procedure comprising thermal precursor decomposition at 710 K in UHV followed by an oxidation($1 \cdot 10^{-6}$ mbar $O_2$)/reduction($1 \cdot 10^{-6}$ mbar $H_2$) treatment at 600 K. The inset in figure 5.24 a) shows the Pd 3d photoelectron regions of both samples after activation. The data demonstrates that both samples have a similar Pd loading of about 0.4 ML.

The main window of figure 5.24 a) shows $^{13}$CO desorption spectra recorded after a saturation dose of $^{13}$CO at 150 K. Compared to CO desorption from oxide supported Pd samples reported in literature, the PVD sample shows a similar behaviour [226, 227]. In general, the desorption between 200 K and 400 K can be assigned to CO bound linearly to Pd, whereas the higher temperature feature at 465 K is due to multiple, mainly 3 - fold coordinated CO. The sharp, outstanding peak at 465 K indicates, that the Pd particles exhibit well defined facets. In comparison, the LPD sample shows in general a similar spectral shape and signal size. There is, however, an additional shoulder at the low temperature side of the 465 K peak (350 K - 400 K). Since there is a good correlation between the $^{13}$CO desorption signal and the XPS signal, a similar loading and particle size distribution can be assumed for both samples. The higher number of low - coordinated $^{13}$CO molecules on the LPD sample therefore indicates that here, the Pd particles have a slightly more irregular surface and less extended facets compared to the PVD sample. Similar conclusions have been obtained previously in our group for a Pd - $Fe_3O_4$ model catalyst [163].

The catalytic activity towards CO oxidation was tested by first applying a saturation dose of oxygen at 400 K and subsequently a $^{13}$CO dose at 150 K. Figure 5.24, b) and c) show the $^{13}$CO and $^{13}$CO$_2$ desorption traces obtained after this treatment. Clearly, for both LDP and PVD samples $^{13}$CO$_2$ evolution can be observed which goes along with a decrease of $^{13}$CO desorption. The signal intensities are similar, indicating a similar activity of both catalysts. The $^{13}$CO$_2$ desorption maximum at 400 K - 420 K is in perfect agreement with previous studies [227].

In summary, the XPS and TPD data shows, that the activation treatment including heating and oxidation/reduction steps results in Pd particles of similar properties for LPD and PVD samples. Small deviations are due to slight differences in Pd loading or can be explained by smaller facet sizes and higher numbers of low - coordinated Pd atoms on the particle surface of LPD samples. The structural differences of the particles are probably a result of the strong surface roughening of MgO upon exposure to ambient conditions.

## 5.4. Conclusions

In this study, a surface science approach of metal deposition by LPD onto a thin, metal single crystal supported oxide film, which had recently been introduced by our group, was applied to the Pd - MgO/Ag(001) system. The interest of this particular system in LPD arises from the fact that due to its relative simplicity, MgO is a widely studied model system and support material in fundamental

catalysis research. Thus, using MgO thin films as a support for LPD, contributes to bridging the gap between fundamental catalyst research and applied catalysis.

Since the stability of the support is a precondition for successful metal deposition, we investigated the stability of thin MgO films in aqueous solutions of different pH prior to any LPD experiments. In the acidic regime (pH 2), 20 ML MgO/Ag(001) films dissolved instantly within the time resolution of our experiment (5 sec). At pH 7, an equivalent film was dissolved after about 40 sec. Only at pH 12, which is the point of zero charge of MgO, the films were stable on the long term after a few monolayers dissolved within the first 5 - 10 minutes of exposure.

An important aspect for the next step - the deposition of Pd - was the closeness of the MgO/Ag(001) films. Only completely closed films turned out to guarantee a stable Pd loading. This was shown by a Pd - LPD experiment on a MgO/Ag(001) film of 5 ML nominal thickness, where the majority of Pd diffused into the bulk of the Ag crystal upon annealing to 710 K. More detailed XPS and ISS analysis showed, that only above a nominal thickness of 20 - 30 monolayers, the MgO films are completely closed. In subsequent experiments, LPD of Pd was performed on 60 ML films exclusively. Strong structural surface modifications induced by LPD were evidenced by LEED. The pristine MgO pattern could only be partially restored after annealing. The high degree of surface roughness after liquid exposure was also illustrated by STM images recorded in air.

Techniques for removing undesired contaminations, such as sodium, chlorine and carbon, which would increase the complexity of our system, were tested as well. Sodium and chlorine, which are present in the precursor solution, could be removed successfully by a short Millipore water rinse subsequent to the liquid deposition. The removal of carbon, on the other hand, was not straight forward. Whereas carbonaceous species could be removed by annealing to 710 K, adventitious carbon was sometimes remarkably stable. Remaining carbon seemed furthermore to affect the chemical state of the decomposed precursor. Daily changes in carbon loading and stability could not be avoided despite of great experimental care, such that we tentatively assign them to fluctuations of the ambient air composition.

The loading of Pd was found to correlate in an almost perfectly linear way with the precursor concentration in solution and also increase with exposure time. For small loadings ($\leq 0.4$ ML) and in the absence of carbon, a highly stable oxidic Pd species was detected on the surface after thermal precursor decomposition (annealing at 710 K).

Finally, Pd - LPD samples were compared to Pd - PVD samples by means of TPD with respect CO desorption and catalytic activity towards CO oxidation. The total $^{13}$CO desorption of LPD and PVD samples was similar for similar loadings. Thus, the Pd surface area and particle size can be assumed to be similar as well. However, the LPD sample showed a higher degree of desorption from low or single - coordinated Pd sites, indicating smaller facets on the particle surfaces. This can be understood in the context of strong surface roughening which the MgO support experiences in ambient conditions.

By applying an annealing/oxidation/reduction procedure, Pd‑LPD precursors could be successfully decomposed and activated. Upon codosing $O_2$ and $^{13}CO$, $^{13}CO_2$ evolution was observed for both PVD and LPD samples in approximately equal amounts and with resembling shapes of the desorption trace. The desorption maximum was around $400\,K$‑$420\,K$, in agreement with literature [227]. In summary, these results show that Pd/MgO/Ag catalysts of similar catalytic properties were obtained after applying both a surface science (Pd‑PVD) and a wet chemical (Pd‑LPD) preparation procedure.

# Chapter 6.

# Conclusions

Catalyst research faces the challenge of getting an understanding of catalytic processes at the molecular scale. Only comprehensive knowledge on this subject will allow one day for a systematic design of catalysts for specific target reactions. Fundamental research has been tackling this demanding issue for many decades.

Still, up to now, we have to rely on trial‑and‑error studies to a great extent since there remain large discrepancies between systems that we are able to understand (model catalysts) and the highly complex systems used in applied catalysis.

Basic knowledge, which has been acquired in the past, is essential to build up on. Still, in order to overcome the large existing gaps, it is indispensable to use present knowledge as a base and to increase the complexity of models stepwise in a controlled way towards more realistic systems.

In this thesis, two approaches were followed to achieve this goal:

1) Commonly, model systems, like dispersed metal particles on thin, metal single crystal supported oxide films, are prepared, characterized and tested in UHV conditions. One way to approach a more realistic scenario is to investigate the structure and catalytic activity of such model systems in ambient conditions. This can be done, for example, by exposing a model catalyst to elevated pressures, air or even aqueous solutions. Also, a catalytic reaction might be run in ambient conditions using a model catalyst. In this work, experimental results documenting the stability and reactivity of ultrathin, metal supported oxide films in ambient conditions are presented. Such systems have recently attracted increasing attention when it was found that they can exhibit outstanding catalytic activity due to their unique properties.

The present work focuses on the behaviour of $FeO(111)$ and $MgO(001)$ ultrathin films in ambient conditions. There are fundamental differences between both systems which could lead to different catalytic properties. a) $FeO(111)$ is a polar surface in contrast to $MgO(001)$. b) Iron is a group 8 transition metal with a rich chemistry due to its wide range of oxidation states (-2 to +6, with +2 and +3 being the most common states). Magnesium, on the other hand, is an alkaline earth metal which adapts preferentially an oxidation state of +2 due to the closed shell configuration.

$FeO(111)/Pt(111)$ films were characterized upon exposure to air and water. Furthermore, their catalytic activity towards CO oxidation - a benchmark reaction in surface science - was tested at ambient pressure. Ultrathin MgO

films were grown on Mo(001) and Ag(001). Again, CO oxidation was used as a test reaction to investigate the catalytic activity at ambient pressure. Pristine and post‑reacted MgO films were compared by chemical characterization.

2) Another possible approach towards more realistic model catalysts is to mimic realistic preparation procedures on model substrates. This field has not been explored intensively in the past. The preparation method can, however, be crucial for the final performance, since it affects morphology, stability and composition of a catalyst to a great extent. Particularly interesting are wet chemical methods, since the majority of heterogeneous catalysts used in industry is prepared in this way. Using a metal supported oxide film as a substrate for LPD allows to mimic a realistic preparation on a sample exhibiting a well defined surface structure which can be characterized and tested under controlled conditions by surface science techniques.

In this thesis, for the first time, Pd/MgO(001)/Ag(001) catalysts were successfully prepared by wet impregnation. In the deposition step, MgO(001)/Ag(001) films were exposed to an aqueous solution containing $Pd(OH)_4^{2-}$ precursor complexes. The samples were investigated at relevant stages of the preparation and the influence of several deposition parameters was studied in detail.

### 6.0.1. Ultrathin Films in Ambient Conditions

Ultrathin films investigated in this work comprise FeO(111)/Pt(111), MgO(001)/Mo(001) and MgO(001)/Ag(001).

We investigated the behaviour of FeO films in $H_2O$ vapor, $H_2O/O_2$ atmosphere, in air and in water. In the presence of oxygen in the gas phase or upon exposure to water, a significant oxygen enrichment and hydroxylation is observed. A regular arrangement of islands, which is due to different thermodynamic properties within the Moiré unit cell of the film, was observed in air and even in water. Previously, a bilayer $\rightarrow$ trilayer transition from FeO to $FeO_2$ upon mild heating in oxygen atmosphere was reported [58]. Comparing that study to our data and regarding the conditions we exposed our samples to, we postulate the formation of a hydroxylated trilayer (FeO(OH)).

A different kind of hydroxylated film is obtained if FeO(111)/Pt(111) is exposed to water vapor only. If, during dosing, the ion gauge is turned on, the resultant film also shows different properties. In both situations, the OH groups absorb IR light at different wavenumbers compared samples exposed to $H_2O/O_2$ atmosphere, air or water. Upon dosing in the presence of a glowing ion gauge filament, no enrichment of oxygen is observed. Therefore, we suggest the formation of a hydroxylated bilayer in this case.

As a whole, these results show that the oxygen chemical potential is the driving force for a bilayer $\leftrightarrow$ trilayer transition. These experimental observations were corroborated by DFT calculations of Pacchioni and coworkers.

Analog to the $FeO_2$ trilayer, the FeO(OH) films showed a pronounced catalytic activity towards CO oxidation and a reversible dewetting behaviour. Our

results show that the catalytic properties of the FeO(111)/Pt(111) system are maintained in ambient conditions.

In summary, this work demonstrates that the ultrathin FeO(OH) trilayer exhibits a remarkable stability in air and water and exhibits a pronounced activity towards CO oxidation at ambient pressure.

These results indicate that also ultrathin oxide overlayers, which can grow as a consequence of strong metal support interaction (SMSI) on dispersed metal particles, might be stable in ambient conditions. Such structures might, therefore, also form on applied catalysts.

Ultrathin MgO(001)/Ag(001) films had theoretically been predicted to efficiently activate $O_2$ and to catalyze CO oxidation [2]. Furthermore, activated oxygen had been observed in a UHV study on ultrathin MgO(001)/Mo(001) [3]. We tested the activity of both systems towards CO oxidation at ambient pressure in atmospheres of different $O_2$:CO ratios and for different film thicknesses. We did not find evidence for enhanced catalytic activity in any case. Differences between both systems can only be assigned to the Ag(001) and Mo(001) substrates. Ag shows intrinsic activity towards CO oxidation but is not chemically altered after the reaction. Mo, on the other hand, exhibits no activity, but gets superficially oxidized with increasing degrees for higher oxygen pressures. Even though we have no direct measure for activated oxygen, the strongly suppressed $O_2$ adsorption on MgO(001)/Ag(001) observed by TPD suggests the formation of the peroxide anion must be very small even in the most optimistic case.

The distinctive feature of this study compared to previously cited reports is, that here, the samples were tested at *ambient* pressure. A lack of oxygen supply being the reason for a lack of activity is unlikely, since the films are inactive even for very oxygen rich conditions (5 mbar CO + 250 mbar $O_2$).

### 6.0.2. A Pd/Mg(001)/Ag(001) catalyst prepared by LPD in ambient conditions

MgO, which is a widely studied model system of relatively simple structure, was used in this work as a catalyst substrate. Since catalyst preparation by wet chemical methods has not been reported on thin, metal supported MgO films so far, the first step of this project was to investigate the stability of these films in aqueous solutions. They turned out to dissolve fastest in acidic solutions. Only at pH 12, around the point of zero charge of MgO, the films were long-term stable after initial dissolution of a few monolayers in the first minutes.

LEED indicated strong surface roughening after the liquid phase deposition. The MgO pattern was only partially restored after annealing which indicates permanent modifications of the surface structure.

For the first LPD experiments implemented on a 5 ML MgO film, Pd was found to dissolve into the Ag bulk crystal upon annealing. This motivated a more detailed study on the closeness of MgO(001)/Ag(001) films. Results from AES, XPS and ISS are all consistent in suggesting that even films as thick as

20 ML expose silver at the surface. Only for a thickness of 32 ML, silver was not detected at the surface any more. Therefore, subsequent LPD studies were continued using 60 ML thick films only.

The Pd loading and chemical state were investigated as a function of precursor concentration and deposition time. The loading turned out to be an almost perfectly linear function of the precursor concentration whereas the deposition time had only a minor effect. The thermal decomposition of the precursor was, however, strongly affected by the deposition time in the case of small loadings ($\leq 0.4\,\mathrm{ML}$).

Since deposition was carried out in ambient air, carbonaceous species were always detected at the surface after deposition. Their amount and thermal stability varied from day to day. This parameter could not be controlled precisely despite of great experimental care.

Regarding chemical and catalytic properties, Pd/MgO/Ag catalysts prepared by LPD were compared to corresponding samples prepared by PVD. Both samples showed similar CO TPD spectra and catalytic activity towards CO oxidation. The CO TPD measurements indicated, however, a slightly higher degree of low coordinated CO on the LPD prepared samples. Apparently, here, the Pd particle have less extended facets. This could be a consequence of the strong surface roughening which the MgO substrate experiences upon exposure to the precursor solution.

In summary, in this work, the widely studied model system MgO(001)/Ag(001) has been used as a substrate for catalyst preparation by LPD for the first time. It shows a more complex behaviour in aqueous solution than the previously studied $Fe_3O_4$/Pt(111) support [162]. However, if the experimental conditions are chosen appropriately, Pd can be deposited successfully. The resulting catalysts show similar properties and catalytic activity towards CO oxidation as corresponding samples prepared by PVD.

# Appendix A.

# Two Dimensional Silica on Ru(0001)

## A.1. Introduction

### A.1.1. General

Silica and its derivatives are of huge technological importance [228, 229, 230]. Broad knowledge about tuning their material properties is available and expanding this knowledge is of great scientific interest. In catalysis, silica constitute a common support material [231] due to their chemical inertness, thermal stability and since being an abundant low cost material. A silica derivative, which constitutes an important group of materials in catalysis, are zeolithes [232, 233]. They form porous materials with a high surface area and consist of a crystalline network of interconnected silica and alumina tetrahedra.

In surface science, silica has also been intensively investigated for several decades [234, 235, 236, 237], but it was not until about 13 years ago, that the first ultrathin, structurally well defined film could be prepared. This system was a crystalline silica monolayer on Mo(112) [238]. The structure of the film consists of a corner‐sharing network of $SiO_4$ tetrahedra, i.e. a two dimensional anaologon to the three dimensional network of glass. However, the system shows strong interaction between the silica monolayer and the metal support. Therefore, as a model system for glass or zeolithes, is has certain limitations. Recently, an new $SiO_2$ bilayer structure grown on Ru(0001) has been developed [239] which can be grown - depending on preparation conditions - in a vitreous or crystalline form [240]. The crystallinity of the film depends on the interplay of a number of paramters. Amongst others, the cooling rate after the final oxidation step is of crucial importance. Low cooling rates favour the formation of a crystalline phase whereas fast cooling leads to a vitreous structure [241]. The electronic structure of the film can be tuned by reversible chemisorption of oxygen atoms directly on the Ru(0001) surface underneath the silica bilayer [242].

The bilayer is bound to the Ru substrate by weak van der Waals interactions, such that the chemistry of the film is influenced much less by the metal support than in the case of the monolayer. Therefore, it can be considered a better model system. Still, on an absolute scale, the film‐support interaction on Ru(0001) is intermediate, such that a monolayer, which requires stronger interaction, can be grown on Ru(0001) as well. On Pt(111), in contrast, only a bilayer structure could be prepared successfully [243]. Here, the interaction between metal and film is weak. The general advantage of being able to grow ultrathin, crystalline silica films consists in the applicability of surface sensitive techniques as well as a well defined structure with reduced complexity as compared to amorphous samples.

Chemical process can be assigned to particular sites within the unit cell. On the other hand, these crystalline films are a starting point for the preparation of mixed silica‑alumina bilayer films which constitute a model system for zeolithes [244].

The aim of this work was to introduce ultrathin, metal supported bilayer silica films (SiO$_2$/Ru(0001)) in our group. We wanted to provide a solid base with respect to reproducible sample growth and comparability to samples prepared by other groups of our department [239, 240]. On the long term, this system is of interest for us as a support for catalyst preparation using liquid phase deposition. Silica is a very inert material, and thin silica films are stable over a wide pH range upon exposure to metal precursor solutions - as we can conclude from LPD experiments which have meanwhile been implemented in our group.

### A.1.2. SiO$_2$/Ru(0001)

Figure A.1 depicts the structure of the SiO$_2$/Ru(0001) bilayer in its crystalline form. The Ru(0001) surface is of hexagonal symmetry with a lattice constant of 0.271 nm [245]. The unit cell of crystalline silica is just twice as large (0.54 nm [239]), such that there is a very good match between substrate and film.

By annealing in oxygen atmosphere ($1 \cdot 10^{-7}$ mbar O$_2$) or UHV, the film can be reversibly switched between an oxygen rich (figure A.1, right) and an oxygen poor (figure A.1, left) configuration. The additional oxygen is adsorbed on the Ru(0001) surface exclusively, which it can access trough the open pores of the silica rings.
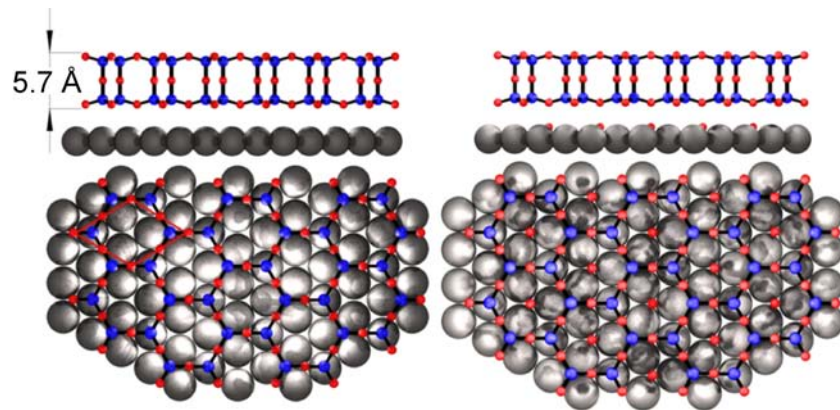


Figure A.1.: Oxygen poor and oxygen rich structure of SiO$_2$/Ru(0001). Silicon atoms are indicated in blue, oxygen atoms are indicated in red [1].

The phonon spectrum gives insight about the state of the sample. After deposition of silica on the Ru(0001) surface, a broad absorption feature is centered around 1230 cm$^{-1}$ in the IRA spectrum. Absorption at this position has previously been observed for amorphous silica films where it has been assigned to the asymmetric longitudinal‑optical phonon mode [246]. After the final oxidation

---

[1]with courtesy of Dr. William Kaden

step, the absorption feature shifts to about $1300 \, cm^{-1}$ and transforms into a much sharper peak. The asymmetric stretching vibration of the silicon‑oxygen‑silicon bond perpendicular to the surface gives rise to this phonon, which is observed for both vitreous and crystalline samples [244]. It is, therefore, an indicator for the presence of the bilayer structure but not for crystallinity.

## A.2. Experimental

All experiments were implemented in the IRAS‑setup, which is described in section 2.7.1. The Ru(0001) crystal was cleaned by sputter‑annealing cycles ($2 \mu A$ $Ar^+$ sputtering for 20 min followed by annealing at 1420 K for 10 min). Order an cleanliness of the surface were checked by LEED and XPS.

Prior to silicon deposition, the Ru crystal was heated in oxygen to prepare a O(2×1)/Ru(0001) surface. Presumably, the adlayer of chemisorbed atomic oxygen prevents intermixing of silicon and ruthenium. Furthermore, silicon can probably be oxidized more easily if dissociated oxygen is already present at the surface [241]. For our experiments, we treated the surface with $1 \cdot 10^{-7}$ mbar $O_2$ at 400 K for 5 min prior to silicon deposition. After this oxygen pretreatment, the LEED pattern showed in addition to the bright Ru spots additional, slightly dimmer spots originating from the O(2×1) superstructure.

As a next step, 2 ML equivalents of silicon were deposited at 633 K in a $2 \cdot 10^{-7}$ mbar $O_2$ atmosphere. After deposition, the silicon was still not fully oxidized and in an amorphous state, as evidenced by the absence of a LEED pattern. The bilayer formation was induced by a final oxidation step ($2 \cdot 10^{-6}$ mbar $O_2$ at $\sim 1180$ K for 10 min).

Nowadays, a more intense oxygen pretreatment ($3 \cdot 10^{-6}$ mbar $O_2$ at 1200 K for 5 min), which leads to the formation of a 3O(2×2) superstructure instead of a O(2×1) superstructure, has become the standard procedure in our department [241].

## A.3. Results and Discussion

### A.3.1. Film Preparation

Our aim was to establish the growth of crystalline 2 ML $SiO_2$/Ru(0001) films in our group. In order to provide good comparability, we characterized our samples by LEED, XPS, IRAS and TPD.

LEED gives important insight about the state of the sample after each preparation step. In figure figure A.2, our LEED patterns are compared to those of the "Structure and Reactivity" group of our department[2], whose data we refer from now on to as 'reference data'. After the crystal cleaning, the characteristic hexagonal pattern of Ru(0001) is observed. The subsequent oxygen treatment

---

[2]Fritz‑Haber Institute, Berlin, Department of Chemical Physics
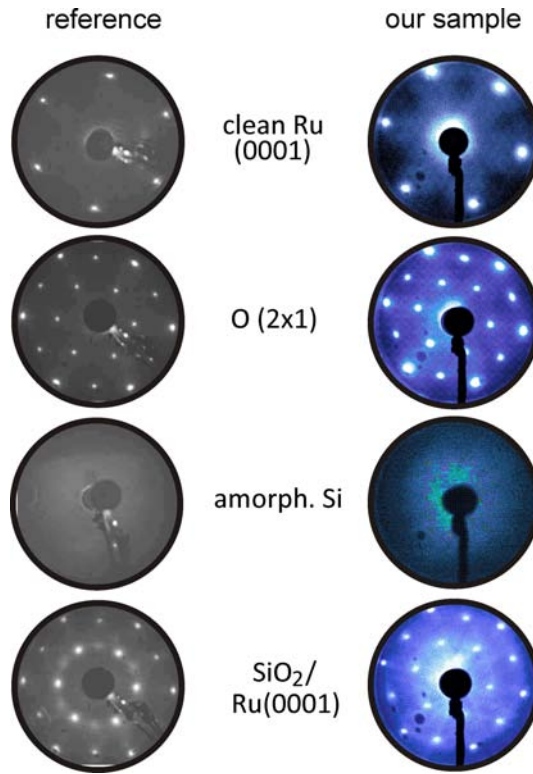
Figure A.2.: Growth of $SiO_2$ films monitored by LEED. Left: Reference images. Right: LEED images taken in our IRAS‑setup.

leads to additional spots in the pattern which are a little fainter than the Ru spots and originate from a $O(2\times1)$ superstructure. Upon the deposition of $2\,ML$ equivalents of silicon, the structural long range order is completely gone as evidenced by a dark LEED screen. The final oxidation step, however, recovers a LEED pattern where the spot positions are identical to those observed for the $O(2\times1)/Ru(0001)$ surface. This hexagonal pattern reappears if the $SiO_2$ bilayer is crystalline or sufficiently dewetted to reveal large areas of the O/Ru support. In the vitreous case, it is characterized by ring structures. Our data matches the reference images well and suggests the crystalline state of our samples.

We also compared our XP spectra measured during film growth to reference data. Our data is, in general, in good agreement with the reference spectra. Binding energy differences are $0.3\,eV$ at maximum. A comparison of XP O 1s as well as Si 2p regions is shown in figure A.3. After the deposition of silicon, there is only one O 1s species present at $532.6\,eV$. For silicon, on the other hand, we observe a reduced $(100\,eV)$ and an oxidized $(103.1\,eV)$ Si 2p species. A Si 2p binding energy at $100\,eV$ is at the upper edge of the spectrum of reported $Si^0$ binding energies, which lie in the range of about $98.5\,eV$ up to $100\,eV$ [247, 248]. The $103.1\,eV$ peak, on the other hand, is in the range of what is reported for $SiO_2$ [249, 250]. Apparently, the atomic oxygen adlayer has been consumed to oxidize part of the silicon, but it was not sufficient for complete oxidation.
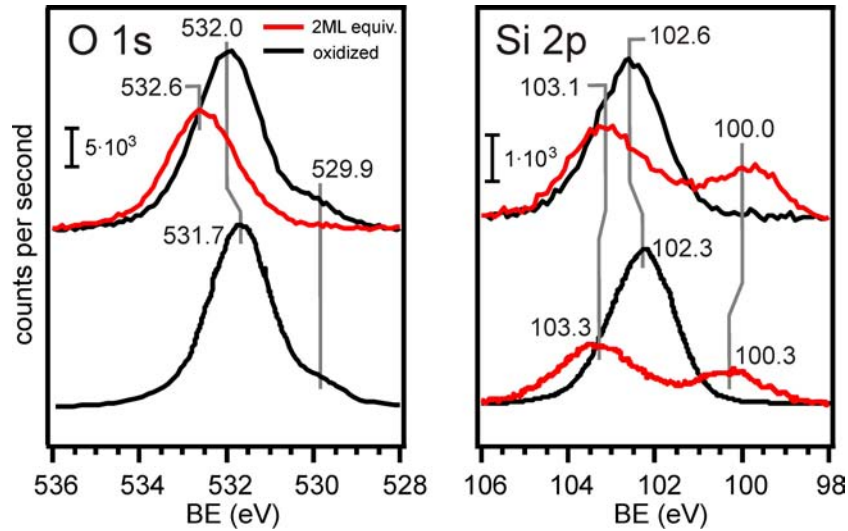
Figure A.3.: XP O 1s and Si 2p regions of a nominal 2 ML SiO$_2$ film. Red traces were taken after deposition of Si. Black traces were measured after a final oxidation step at 1260 K. Top graphs: Data obtained from our IRAS - setup. Bottom graphs: Reference data.

After the final oxidation step, only one Si 2p feature remains at 102.6 eV. Taking into account the presence of the metal underneath the ultrathin film, this can be assigned to Si$^{4+}$ [251, 235]. The O 1s peak is found at 532.0 eV as can be assigned to SiO$_2$ as well [252, 253] using an analog argumentation. A small low binding energy shoulder is located at about 529.9 eV, which is due to chemisorbed oxygen on Ru(0001) underneath the bilayer [239].

Since it had been reported prior to our studies, that the film can be reversibly switched between an oxygen poor and an oxygen rich state, we wanted to test this behaviour on our samples as well. We prepared an oxygen poor film by annealing a pristine film at 1170 K in UHV for 10 min. By annealing at 1220 K in 2.6·10$^{-6}$ mbar O$_2$ for 10 min, we switched the film to the oxygen rich state. XPS data, comparing both states of our sample and the reference data, is depicted in figure A.4. For the oxygen poor peaks, there is a very good agreement with the reference spectra with a maximum deviation of the binding energies of 0.1 eV. The O 1s region shows only one single oxygen species located at about 532.8 eV which represents the lattice oxygen of the bilayer. The silicon peak is located at 105.5 eV. The transition to the oxygen rich state is characterized by the evolution of a low binding energy shoulder at 529.9 eV in the O 1s region. This feature represents chemisorbed oxygen on the Ru(0001). The appearance of such a shoulder in our spectrum confirms that we have enriched our sample with oxygen. Another characteristic change during the transition is a binding energy shift of $\sim$ (-0.7) - (-0.8) eV for both the Si 2p and the O 1s peak [242]. We do observe negative shifts in our spectra (-0.7 eV for oxygen and -0.6 eV for silicon). However, they are slightly smaller than the shifts reported in literature and seen in the reference data. Later on, we changed our standard oxidation procedure such that
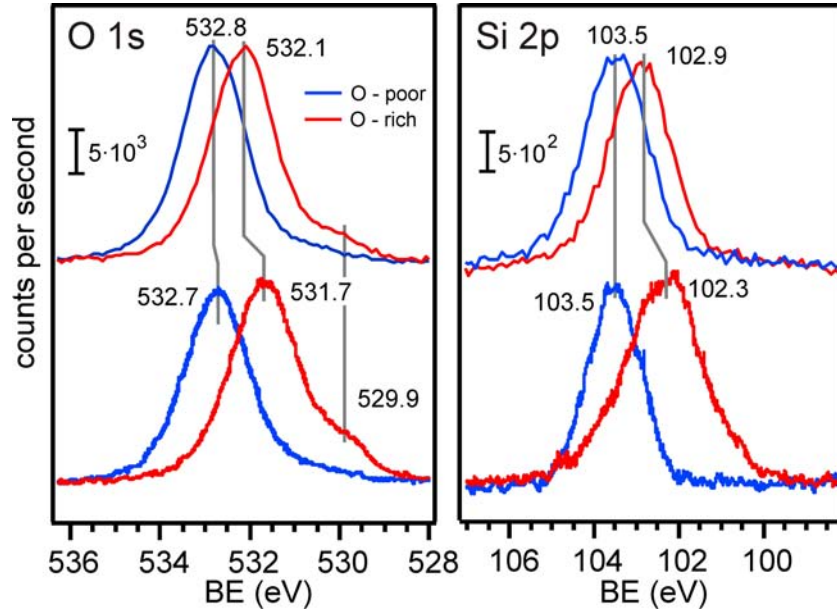
Figure A.4.: XP O 1s and Si 2p regions of nominal 2 ML SiO$_2$ films in oxygen rich (red) and oxygen poor (blue) modes. Top graphs: Data obtained from our IRAS-setup. Bottom graphs: Reference data.

we annealed in $3 \cdot 10^{-6}$ mbar O$_2$ both before and after silicon deposition. With this modification, we are able to achieve a more effective oxygen enrichment and we observe the same binding energy shifts in our spectra as they are observed in the reference data.

In figure A.5, CO TPD spectra from our SiO$_2$/Ru(0001) bilayer films and our clean Ru(0001) and O(2×1)/Ru(0001) surface (upper traces) are compared to CO TPD spectra from clean and oxygen precovered Ru(0001) from literature [254] (lower traces). The CO adsorption capacity is strongly reduced for bilayer samples compared to the corresponding Ru surface (clean or oxygen precovered). Furthermore, much less CO desorbs from an oxygen rich compared to an oxygen poor bilayer sample (compare absolute scales figure A.5 of a) and b)).

The CO desorption from our oxygen rich SiO$_2$/Ru(0001) film resembles a superposition of the CO desorption from O(2×2) and O(2×1) covered Ru(0001) surfaces (figure A.5, a)). A characteristic O(2×2)/Ru(0001) feature at about 440 K is found for the bilayer sample. The O(2×1)/Ru(0001) features at about 220 K and 380 K are, however, more dominant in comparison. Note, that our control spectrum from O(2×1)/Ru(0001) is scaled down by a factor of 10.

For the CO desorption from our oxygen poor sample, we find a strong resemblance to the desorption from a clean Ru(0001) surface in both our control measurement and the spectrum from literature (figure A.5, b)). Again, the control spectrum is scaled down (÷ 3) for comparison. The TPD spectrum from our clean crystal is in perfect agreement with the CO-Ru(0001) spectrum from literature, which confirms that the sample quality and temperature calibration are indeed comparable.

105
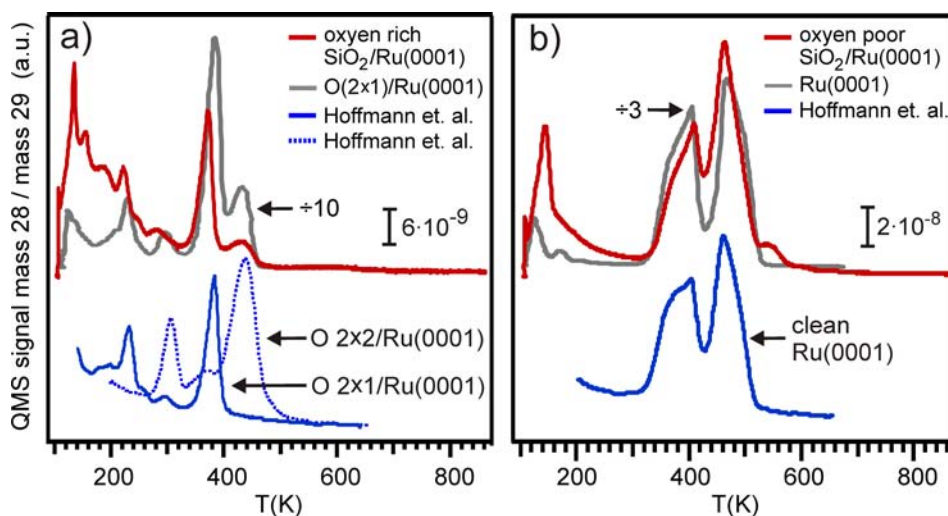
Figure A.5.: CO TPD spectra of our $SiO_2/Ru(0001)$ (red traces, $^{12}CO$, $m/z^+{=}28$) and clean Ru(0001) (grey trace,$^{13}CO$, $m/z^+{=}29$) samples (dose $= 5\,L$ CO at $< 110\,K$, heating rate $= 3\,K/sec$) in comparison with literature data from clean and oxygen precovered Ru(0001) (blue traces, from [254], signal intensity scaled arbitrarily). a) oxygen covered Ru(0001) and oxygen rich silica bilayer. b) clean Ru(0001) and oxygen poor silica bilayer.

The close similarities between desorption from Ru(0001) and $SiO_2/Ru(0001)$ (apart from a scaling factor) strongly suggest that any potential interaction between the silica bilayer and CO is very weak. The Ru(0001) desorption features from the oxygen poor sample might indicate that CO is able to access the metal surface through the six‑membered rings of the crystalline film, such that the film seems partially 'transparent'to the CO molecules (figure A.6, right). However, we can not exclude incomplete coverage, i.e. open Ru patches (figure A.6, middle) or a film comprising vitreous regions (including larger ring sizes) to some extent. The film might also partially consist of monolayer regions (figure A.6, left). Indeed, the coexistence of monolayer and bilayer regions has been observed by STM in UHV in our department [241].
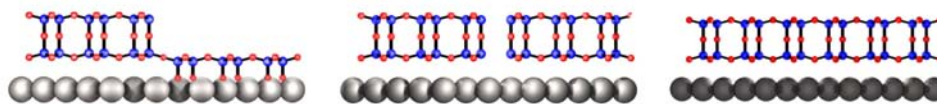


Figure A.6.: Possible pathways for the interaction between CO and Ru(0001) are through pores of monolayer patches (left), completely open patches (middle) or through the pores of the bilayer film (right) [3].

Regarding the oxygen rich bilayer, our data suggests that CO adsorption is strongly suppressed, but qualitatively comparable to desorption spectra

---

[3]with courtesy of Dr. William Kaden

O(2×2)/Ru(0001) and O(2×1)/Ru(0001) surfaces. However, it was found later on, that a higher oxygen enrichment, which can be achieved by a more intense oxygen treatment, leads to the complete suppression of CO adsorption [241].

### A.3.2. Stability in Ambient Conditions
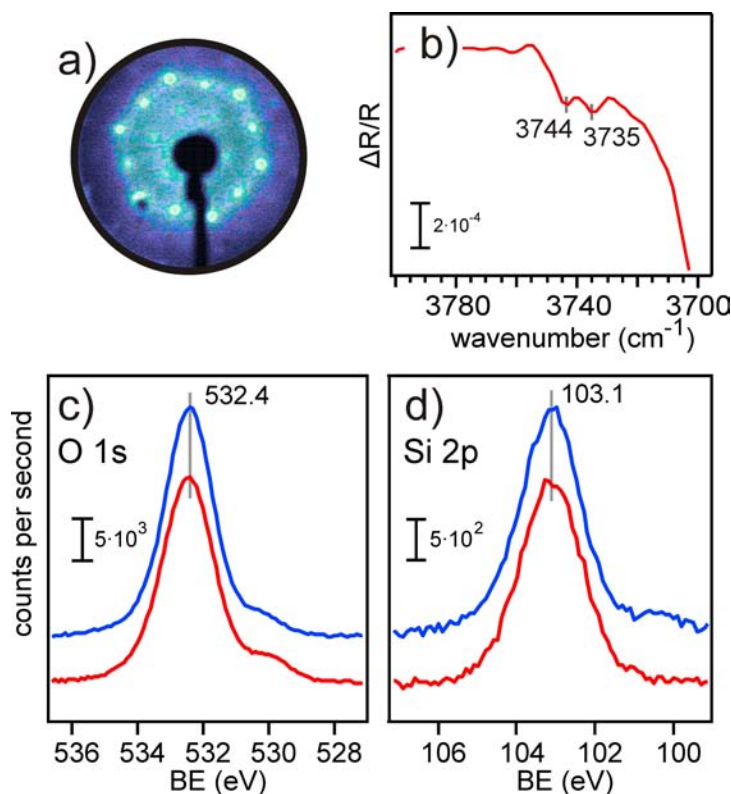


Figure A.7.: Exposure of a $SiO_4$/Ru(0001) bilayer film to ambient conditions. a) LEED image after exposure to air. b) IRAS spectrum after exposure to water. c) and d) XP O 1s and Si 2p regions before and after exposure to water.

In principle, silica is known to be an inert and hydrophobic material. However, for ultrathin, metal supported oxide films, physical and chemical properties can be strongly altered due to the influence of the support. For this reason, and since we were aiming to use the $SiO_2$/Ru(0001) bilayer as a support for LPD, we investigated its stability in ambient conditions.

Figure A.7, a) shows the LEED pattern of our bilayer film after exposure to air. The spots are not as sharp any more as those of pristine films. The pattern and image contrast, however, remain the same. No ring formation, which would indicate a loss of crystallinity, is observed.

These results are complemented by information from XPS (figure A.7, c) and d)). The O 1s and Si 2p regions show no change in binding energy, full width at half maximum or signal intensity. In summary, these results indicate that the film is chemically not altered and its structural integrity is maintained.

We observed two interesting features in the OH region of the IRA spectrum at $3744\,cm^{-1}$ and $3735\,cm^{-1}$ after water exposure and subsequent annealing in UHV to $1070\,K$ (figure A.7, b)). Since OH groups are not detectable in the XP O 1s region, the degree of hydroxylation must be very low. Later on, low degrees of defect-mediated hydroxylation of silica bilayers upon exposure to water vapor were reported [255]. There, the silanol groups were found to be stable up to $\sim 1000\,K$. We have no explanation for the high thermal stability of our IR absorption features in the OH region other than deviations of film properties and temperature readings between the different experimental setups.
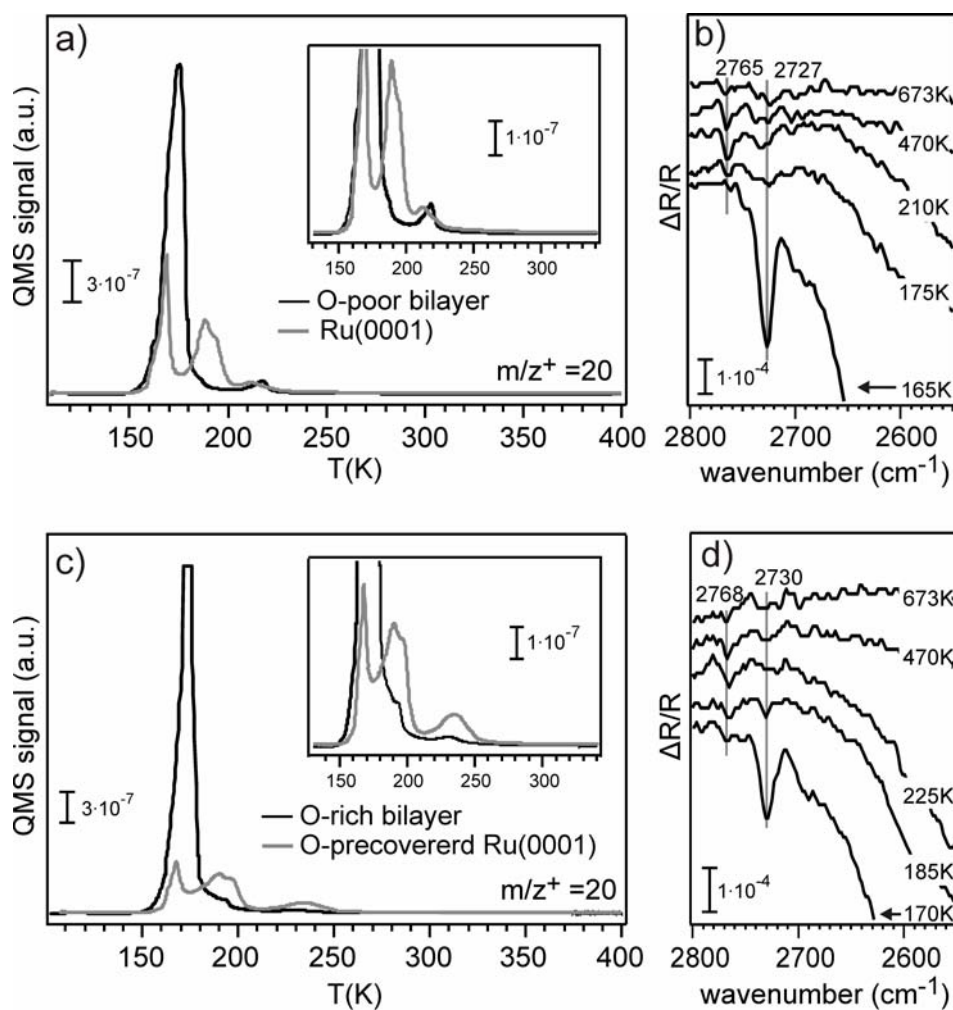


Figure A.8.: $D_2O$ TPD spectra from $SiO_2/Ru$ films in the oxygen rich and oxygen poor state in comparison to $D_2O$ TPD spectra from a clean and $O(2\times1)$ covered $Ru(0001)$ surface (dose $= 2\,L\ D_2O$ at $< 120\,K$, heating rate $= 1\,K/sec$).

Surface hydroxylation has been found to have a major influence on the intrinsic properties and metal nucleation behaviour on ultrathin oxide films. Furthermore, the surface chemistry of zeolithes is known to be determined by bridging OH groups. From the point of view that the silica bilayer is a kind of precursor

model for mixed alumina - silica bilayers, and especially since we wanted to use the silica bilayer as a support for catalyst preparation by LPD, silanol formation was of great interest for us. Therefore, we investigated this issue in more detail by $D_2O$ TPD and temperature dependent $D_2O$ - IRAS measurements. The results are summarized in figure A.8.

Figure A.8 a) and c) depict $D_2O$ TPD spectra, where oxygen poor and rich bilayers are compared to their corresponding Ru(0001) counterparts (clean Ru and O(2×1)/Ru(0001)). Multilayer desorption occurs at ∼ 160 - 180 K for all samples. It is smaller for the Ru samples. However, this is most likely an effect of different effective doses and different amounts of monolayer desorption (which is discussed in the following), since the formation of a multilayer in principle evident. Apart from the multilayer water, there are additional desorption features, at around 190 - 200 K and around 215 - 235 K. The desorption at 190 - 200 K, just above the multilayer feature, can most likely be assigned to monolayer desorption. For the silica samples, this feature is diminished compared to the corresponding Ru samples indicating that the film reduces, but not completely suppresses monolayer adsorption on Ru. The desorption temperature, however, is similar for all samples which suggests that water desorbs from similar binding sites, whose binding energy is not significantly affected by the presence of a bilayer film. The feature at even higher temperatures (215 - 235 K) must be due to some even stronger bound species and is particularly pronounced in the case of oxygen precovered Ru(0001) where it is located at about 235 K. On the oxygen poor samples, on the other hand, it is sharper and shifted to lower temperatures (around 215 K).

In summary, the results indicate, that the adsorption of a strongly interacting monolayer of water on the Ru(0001) substrate is diminished by the presence of chemisorbed oxygen. Silica itself does not lead to additional desorption features of $D_2O$, which is consistent with its hydrophobic properties.

For the IRA spectra shown in figure A.8 b) and d), $D_2O$ was dosed only once at ∼ 100 K. The sample was then flashed to increasingly high temperatures and each time after a flash an IRA spectrum was measured at ∼ 100 K. Up to 165 K, one feature was observed in the O - D region at 2730 cm$^{-1}$. It can be assigned to free surface OD bonds on top of $D_2O$ multilayer of $D_2O$ ice [256]. This signal disappears at 185 K and a new signal emerges around 2765 cm$^{-1}$. In the literature, this signal has been attributed to isolated silanol groups [257, 258]. Since the signal intensity is barely above the signal to noise ratio and much lower than the surface OD signal of the ice layer, the silanol density can be assumed to be very low, such that silanol formation is most likely defect - mediated.

### A.3.3. Hydroxylation by Defect Formation

As explained in the previous section, we had, for several reasons, a great interest in the exploration of silanol formation on the silica bilayer. Upon $D_2O$ dosing and subsequent annealing, only little, most likely defect - mediated silanol formation was observed. These results were confirmed later on by Yang et. al. [255].
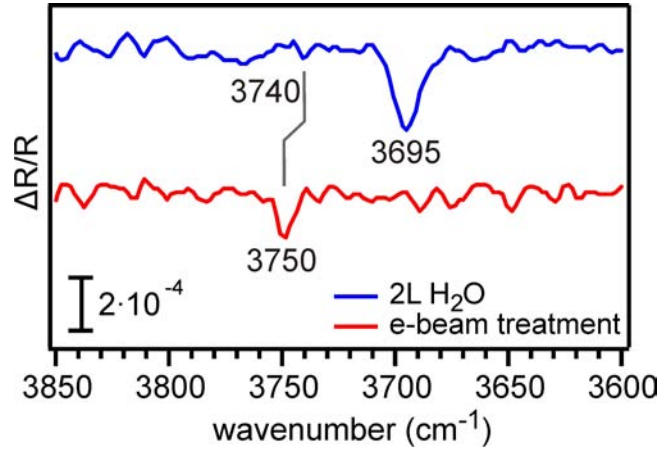
Figure A.9.: Defect formation by electron bombardment (Beam settings: 2.5 mA, 200 eV, 10 min. Sample temperature: 0°C). IRA spectra of a hydroxylated bilayer after electron bombardment in comparison to a bilayer after a 2 L $H_2O$ dose (dose at 110 K; temperature during measurement: 160 K).

We wanted to test the stability of the silica bilayer and see whether we could enhance the silanol formation by artificially inducing defects. Therefore, we exposed a pristine film to electron bombardment for 10 min at 0°C sample temperature (beam settings: 2.5 mA, 200 eV, 10 min). The beam settings were chosen as a compromise between hydroxyl formation on one hand and film disordering and sputtering leading to the exposure of Ru on the other hand. The temperature could not be further reduced despite of liquid nitrogen cooling during the bombardment since the electron beam heated the sample up. The OH region of the resulting IRA spectrum is shown in figure A.9, where it is compared to a 'naturally' hydroxylated sample, i. e. a pristine bilayer after exposure to 2 L $H_2O$ at about 110 K and measured at about 160 K, i.e. in the presence of ice on the surface.

After the electron bombardment, we observe an IR band at $3750\,\mathrm{cm^{-1}}$. This can be assigned straightforwardly to O‑H vibrations [255]. The 'naturally' hydroxylated sample shows a small feature at about $3740\,\mathrm{cm^{-1}}$ which might also indicate the presence of O‑H groups of the same type as observed in the electron bombarded sample. However, in addition, it features a very intense band at $3695\,\mathrm{cm^{-1}}$, which is due to OH groups on ice.

Furthermore, the $3695\,\mathrm{cm^{-1}}$ feature of the water exposed sample is more intense than the $3750\,\mathrm{cm^{-1}}$ band of the electron bombarded sample. The peak areas differ by a factor of 2.3. The silanol formation after exposure to the electron beam is, therefore, rather low, such that the bilayer seems to be remarkably stable.

## A.4. Conclusions

The aim of this work was to establish the silica bilayer system on Ru(0001) in our group for the long‑term purpose of using it as a substrate for LPD experiments. Our results show that we are now able to prepare films, which show very similar characteristics compared to reference data regarding all characterization methods applied (LEED, XPS, IRAS, TPD).

We succeeded in the reversible switching between the oxygen rich and the oxygen poor phase. When this work was implemented, we used slightly milder oxidation conditions than nowadays, which explains deviations of the XP spectra and CO desorption characteristics with respect to the reference data.

The stability of the crystalline bilayer films in ambient conditions was tested in this work. Upon exposure to air and water, LEED, XPS and IRAS indicate, that the films generally preserve their chemical and structural properties. Only small amounts of silanol groups, which had formed most likely on defects, were detected by IRAS. Due to their low density, they were not detectable by XPS.

CO and $D_2O$ measurements revealed that the silica bilayer does not interact strongly with any of the molecules. No additional desorption features emerged on $SiO_2/Ru(0001)$ as compared to spectra from the pure Ru surface. The features originating from CO/Ru or $D_2O$/Ru interaction were mostly diminished in the presence of a silica film. On oxygen rich films, this diminishment was stronger than on the oxygen poor films - most likely due to a blocking of adsorption sites by the chemisorbed oxygen adatoms.

Temperature dependent IRAS measurements gave proof for the strongly hydrophobic character of the silica bilayer - analog to silica bulk systems. Only a small, most likely defect‑mediated amount of silanol formation was observed upon water exposure. Intentional defect formation by electron bombardment resulted only in a small increase of the silanol density and documented the inertness and stability of the bilayer structure.

Meanwhile, the research on this system has further progressed. In our group, metal particles have been successfully deposited on silica bilayers by liquid phase deposition by Kaden et al. [259]. In our department, mixed silica‑alumina bilayers have been prepared and evidence has been provided that these systems do indeed constitute a suitable surface science model system for zeolithes [258, 260]. Certainly, both pathways - using silica bilayers as a support for LPD catalyst preparation and modeling zeolithes by mixed alumina‑silica bilayers, constitute a starting point for a broad range of further investigations.

# Bibliography

[1] Y. N. Sun, Z. H. Qin, M. Lewandowski, E. Carrasco, M. Sterrer, S. Shaikhutdinov, and H. J. Freund, "Monolayer Iron Oxide Film on Platinum Promotes Low Temperature CO Oxidation," *Journal of Catalysis*, vol. 266, pp. 359–368, Sep 10 2009.

[2] A. Hellman, S. Klacar, and H. Groenbeck, "Low Temperature CO Oxidation over Supported Ultrathin MgO Films," *Journal of the American Chemical Society*, vol. 131, pp. 16636+, Nov 25 2009.

[3] A. Gonchar, T. Risse, H.-J. Freund, L. Giordano, C. Di Valentin, and G. Pacchioni, "Activation of Oxygen on MgO: $O_2 \cdot^-$ Radical Ion Formation on Thin, Metal-Supported MgO(001) Films," *Angewandte Chemie - International Edition*, vol. 50, no. 11, pp. 2635–2638, 2011.

[4] J. W. G. Ertl, H. Knoezinger, *Environmental Catalysis*. Wiley-VCH Weinheim, 1999.

[5] I. McConnell, G. Li, and G. W. Brudvig, "Energy Conversion in Natural and Artificial Photosynthesis," *Chemistry & Biology*, vol. 17, pp. 434–447, May 28 2010.

[6] A. T. Najafabadi, "$CO_2$ Chemical Conversion to Useful Products: An Engineering Insight to the Latest Advances Toward Sustainability," *International Journal of Energy Research*, vol. 37, pp. 485–499, May 2013.

[7] A. van Dillen, R. Terorde, D. Lensveld, J. Geus, and K. de Jong, "Synthesis of Supported Catalysts by Impregnation and Drying Using Aqueous Chelated Metal Complexes," *Journal of Catalysis*, vol. 216, pp. 257–264, May 15 2003.

[8] J. Niemantsverdriet, A. Engelen, A. de Jong, W. Wieldraaijer, and G. Kramer, "Realistic Surface Science Models of Industrial Catalysts," *Applied Surface Science*, vol. 144-45, pp. 366–374, Apr 1999. 14th International Vacuum Congress/10th International Conference on Solid Surfaces/5th International Conference on Nanometre-Scale Science and Technology/10th International Conference on Quantitative Surface Analysis, Birmingham, England, Aug 31- Sep 04, 1998.

[9] E. Gallei, M. Hesse, F. Schwab, E. Schüth, and W. J., *Handbook of Heterogeneous Catalysis*. Wiley-VCH, Weinheim, 2008.

[10] D. Goodman, "Model Catalysts - From Extended Single-Crystals to Supported Particles," *Surface Review and Letters*, vol. 2, pp. 9–24, Feb 1995. 11th International Summer Institute in Surface Science (ISISS-94), Univ. Wisconsin Milwaukee, Milwaukee, Wi, Jun 01-03, 1994.

[11] C. Henry, "Surface Studies of Supported Model Catalysts," *Surface Science Reports*, vol. 31, no. 7-8, pp. 235–325, 1998.

[12] J. Schnadt, J. Knudsen, J. N. Andersen, H. Siegbahn, A. Pietzsch, F. Hennies, N. Johansson, N. Martensson, G. Ohrwall, S. Bahr, S. Maehl, and O. Schaff, "The New Ambient-Pressure X-ray Photoelectron Spectroscopy Instrument at MAX-Lab," *Journals of Synchrotron Radiation*, vol. 19, pp. 701–704, Sep 2012.

[13] M. Borasio, *Polarization Modulation Infrared Reflection Absorption Spectroscopy on Pd Model Catalysts at Elevated Pressure.* PhD thesis, FU Berlin, FB Biologie, Chemie, Pharmazie, 2006.

[14] B. Hendriksen and J. Frenken, "CO Oxidation on Pt(110): Scanning Tunneling Microscopy Inside a High-Pressure Flow Reactor," *Physical Review Letters*, vol. 89, p. 046101, Jul 22 2002.

[15] G. Somorjai, "Surface Science at High Pressures," *Zeitschrift für Physikalische Chemie - International Journal of Research in Physical Chemistry & Chemical Physics*, vol. 197, no. Part 1-2, pp. 1–19, 1996.

[16] M. Morkel, V. Kaichev, G. Rupprechter, H. Freund, I. Prosvirin, and V. Bukhtiyarov, "Methanol Dehydrogenation and Formation of Carbonaceous Overlayers on Pd(111) Studied by High-Pressure SFG and XPS Spectroscopy," *Journal of Physical Chemistry B*, vol. 108, pp. 12955–12961, Aug 26 2004.

[17] J. Nickl, R. Schlögl, A. Baiker, H. Knozinger, and G. Ertl, "Preparation and Characterization of a Model System for the Study of Monolayers and Multilayers of Vanadia Supportes Titania," *Catalysis Letters*, vol. 3, no. 5-6, pp. 379–387, 1989.

[18] L. vandeLoosdrecht, M. vanderHaar, A. vanderKraan, A. vanDillen, and J. Geus, "Preparation and Properties of Supported Cobalt Catalysts for Fischer-Tropsch Synthesis," *Applied Catalysis A - General*, vol. 150, pp. 365–376, Mar 13 1997.

[19] L. Coulier. PhD thesis, Eindhoven University of Technology, The Netherlands, 2001.

[20] M. Sterrer and H.-J. Freund, "Towards Realistic Surface Science Models of Heterogeneous Catalysts: Influence of Support Hydroxylation and Catalyst Preparation Method," *Catalysis Letters*, vol. 143, pp. 375–385, May 2013.

[21] S. Shaikhutdinov and H. J. Freund, "Ultrathin Oxide Films on Metal Supports: Structure-Reactivity Relations," in *Annual Review of Physical Chemistry, Vol. 63* (Johnson, MA and Martinez, TJ, ed.), vol. 63 of *Annual Review of Physical Chemistry*, pp. 619–633, Annual Reviews, 2012.

[22] *Surface Analysis - The Principal Techniques.* Vickermann J. and Gilmore I., 2009.

[23] S. Hofmann, *Auger- and X-Ray Photoelectron Spectroscopy in Materials Science.* Springer, 2013.

[24] S. Doniach and M. Sunjic, "Many-Electron Singularity in X-Ray Photoemission and X-ray Line Spectra from Metals," *Journal of Physics Part C - Solid State Physics*, vol. 3, no. 2, pp. 235–239, 1970.

[25] F. Moulder, W. Stickle, P. Sobol, and K. Bomben, *Handbook of X-ray Photoelectron Spectroscopy.* Perkin-Elmer Corporation, 1992.

[26] C. Wagner, "Chemical Shifts of Auger Lines and Auger Parameter," *Faraday Discussions*, vol. 60, pp. 291–300, 1975.

[27] P. Auger, "Secondary Beta Rays Produced in Gas by X rays," *Comptes Rendus Hebdomadaires des Seances de l'Academie die Sciences*, vol. 177, pp. 169–171, Jul-Dec 1925.

[28] O. Oen, "Universal Shadow Cone Expressions for an Atom in an Ion-Beam," *Surface Science*, vol. 131, no. 2-3, pp. L407–L411, 1983.

[29] C. Davisson and L. Germer, "Diffraction of Electrons by a Crystal of Nickel," *Physical Review*, vol. 30, pp. 705–740, Dec 1927.

[30] M. Cox, G. Ertl, and R. Imbihl, "Spatial Self-Organization of Surface-Structure During an Oscillating Catalytic Reaction," *Physical Review Letters*, vol. 54, no. 15, pp. 1725–1728, 1985.

[31] M. Prutton, *Introduction to Surface Physics*. Oxford University Press, 1994.

[32] P. Willmott, *An Introduction to Synchrotron Radiation: Techniques and Applications*. Wiley-VHC, 2011.

[33] D. King, "Thermal Desorption from Metal-Surfaces," *Surface Science*, vol. 47, no. 1, pp. 384–402, 1975.

[34] J. Niemantsverdriet, P. Dolle, K. Markert, and K. Wandelt, "Thermal-Desorption of Strained Monoatomic Ag and Au Layers from Ru(001)," *Journal of Vacuum Science & Technology A - Vacuum Surfaces and Films*, vol. 5, pp. 875–878, Jul-Aug 1987.

[35] M. Hopstaken, W. van Gennip, and J. Niemantsverdriet, "Reactions Between NO and CO on Rhodium(111): an Elementary Step Approach," *Surface Science*, vol. 433, pp. 69–73, Aug 2 1999. 14th International Vacuum Congress/10th International Conference on Solid Surfaces/5th International Conference on Nanometre-Scale Science and Technology/10th International Conference on Quantitative Surface Analysis, Birmingham, England, Aug 31 - Sep 04, 1998.

[36] M. Hopstaken and J. Niemantsverdriet, "Lateral Interactions in the Dissociation Kinetics of NO on Rh(100)," *Journal of Physical Chemistry B*, vol. 104, pp. 3058–3066, Apr 13 2000.

[37] J. Niemantsverdriet, *Spectroscopy in Catalysis*. Wiley-VHC, 2007.

[38] P. Redhead, "Thermal Desorption of Gases," *Vacuum*, vol. 12, pp. 203–211, 1962.

[39] J. K. E. Habenschaden, "Evaluation of Flash Desorption Spectra," *Surface Science*, vol. 138, pp. L147–L150, 1984.

[40] R. Greenler, "Infrared Study of Adsorbed Molecules on Metal Surfaces by Reflection Techniques," *Journal of Chemical Physics*, vol. 44, no. 1, pp. 310–315, 1966.

[41] R. Greenler, "Design of a Reflection-Absorption Experiement for Studying IR-Spectrum of Molecules Adsorbed on a Metal-Surface," *Journal of Vacuum Science & Technology*, vol. 12, no. 6, pp. 1410–1417, 1975.

[42] G. Blyholder, "Molecular Orbital View of Chemisorbed Carbon Monoxide," *Journal of Physical Chemistry*, vol. 68, no. 10, p. 2772–2777, 1964.

[43] M. Wilms, *Potentiodynamische Rastertunnelmikroskopie an Fest/Flüssig - Grenzflächen: Apparative Entwicklung und Untersuchungen zur Sulfat - Adsorption auf Cu(111)*. PhD thesis, Rheinische Friedrich - Wilhelms - Universität, Bonn, 1999.

[44] P. Atkins, T. Overton, J. Rourke, M. Weller, and F. Armstrong, *Shriver and Atkins' Inorganic Chemistry (Fifth Edition)*. W. H. Freeman and Company, New York, 2010.

[45] J.-Y. Park, Y.-J. Lee, P. K. Khanna, K.-W. Jun, J. W. Bae, and Y. H. Kim, "Alumina-Supported Iron Oxide Nanoparticles as Fischer-Tropsch Catalysts: Effect of Particle Size of Iron Oxide," *Journal of Molecular Catalysis A - Chemical*, vol. 323, pp. 84–90, May 17 2010.

[46] *Ullmann's Encyclopedia of Industrial Chemistry.* Wiley-VCH, 2005.

[47] V. Indovina, M. Campa, F. Pepe, D. Pietrogiacomi, and S. Tuti, "The Catalytic Activity of $FeO_x/ZrO_2$ and $FeO_x$/sulphated-$ZrO_2$ for the NO Abatement with $C_3H_6$ in the Presence of Excess $O_2$," *Applied Catalysis B: Environmental*, vol. 60, pp. 23–31, Sep 1 2005.

[48] A. L. Kustov, S. B. Rasmussen, R. Fehrmann, and P. Simonsen, "Activity and Deactivation of Sulphated $TiO_2$- and $ZrO_2$-based V, Cu, and Fe Oxide Catalysts for NO Abatement in Alkali Containing Flue Gases," *Applied Catalysis B: Environmental*, vol. 76, pp. 9–14, Oct 30 2007.

[49] H. Zeuthen, W. Kudernatsch, G. Peng, L. Merte, L. Ono, L. Lammich, Y. Bai, L. Grabow, M. Mavrikakis, S. Wendt, and F. Besenbacher, "Structure of Stoichiometric and Oxygen-Rich Ultra-Thin FeO(111) Films Grown on Pd(111)," *Journal of Physical Chemistry C*, vol. 117, p. 15155–15163, 2013.

[50] M. Ritter, W. Ranke, and W. Weiss, "Growth and Structure of Ultrathin FeO Films on Pt(111) Studied by STM and LEED," *Physical Review B*, vol. 57, pp. 7240–7251, Mar 15 1998.

[51] G. Vurens, V. Maurice, M. Salmeron, and G. Somorjai, "Growth, Structure and Chemical Properties of FeO Overlayers on Pt(100) and Pt(111)," *Surface Science*, vol. 268, pp. 170–178, May 1 1992.

[52] G. Ketteler and W. Ranke, "Heteroepitaxial Growth and Nucleation of Iron Oxide Films on Ru(0001)," *Journal of Physical Chemistry B*, vol. 107, pp. 4320–4333, May 8 2003.

[53] G. Waddill and O. Ozturk, "Epitaxial Growth of Iron Oxide Films on Ag(111)," *Surface Science*, vol. 575, pp. 35–50, Jan 20 2005.

[54] N. A. Khan and C. Matranga, "Nucleation and Growth of Fe and FeO Nanoparticles and Films on Au(111)," *Surface Science*, vol. 602, pp. 932–942, Feb 15 2008.

[55] J. Corneille, J. He, and D. Goodman, "Preparation and Characterization of Ultra-Thin Iron-Oxide Films on a Mo(100) Surface," *Surface Science*, vol. 338, pp. 211–224, Sep 10 1995.

[56] W. Zhang, Z. Li, Y. Luo, and J. Yang, "First Principles Study on the Geometric and Electronic Structures of the FeO/Pt(111) Surface," *Journal of Physical Chemistry C*, vol. 113, pp. 8302–8305, May 14 2009.

[57] L. Giordano, G. Pacchioni, J. Goniakowski, N. Nilius, E. D. L. Rienks, and H.-J. Freund, "Interplay between Structural, Magnetic, and Electronic Properties in a FeO/Pt(111) Ultrathin Film," *Physical Review B*, vol. 76, p. 075416, Aug 2007.

[58] L. Giordano, M. Lewandowski, I. M. N. Groot, Y. N. Sun, J. Goniakowski, C. Noguera, S. Shaikhutdinov, G. Pacchioni, and H. J. Freund, "Oxygen-Induced Transformations of an FeO(111) Film on Pt(111): A Combined DFT and STM Study," *Journal of Physical Chemistry C*, vol. 114, pp. 21504–21509, Dec 16 2010.

[59] R. Baker, E. Prestrige, and G. McVicker, "The Interaction of Palladium with Alumina and Titanium-Oxide Supports," *Journal of Catalysis*, vol. 89, no. 2, pp. 422–432, 1984.

[60] S. Tauster and S. Fung, "Strong Metal-Support Interactions - Occurence among Binary Oxides of Groups IIA-VB," *Journal of Catalysis*, vol. 55, no. 1, pp. 29–35, 1978.

[61] J. I. Flege, J. Hrbek, and P. Sutter, "Structural Imaging of Surface Oxidation and Oxidation Catalysis on Ru(0001)," *Physical Review B*, vol. 78, p. 165407, Oct 2008.

[62] J. Gustafson, A. Mikkelsen, M. Borg, E. Lundgren, L. Kohler, G. Kresse, M. Schmid, P. Varga, J. Yuhara, X. Torrelles, C. Quiros, and J. Andersen, "Self-Limited Growth of a Thin Oxide Layer on Rh(111)," *Physical Review Letters*, vol. 92, p. 126102, Mar 26 2004.

[63] W. Li, L. Osterlund, E. Vestergaard, R. Vang, J. Matthiesen, T. Pedersen, E. Laegsgaard, B. Hammer, and F. Besenbacher, "Oxidation of Pt(110)," *Physical Review Letters*, vol. 93, p. 146104, Oct 1 2004.

[64] G. Zheng and E. Altman, "The Oxidation of Pd(111)," *Surface Science*, vol. 462, pp. 151–168, Aug 10 2000.

[65] E. Lundgren, G. Kresse, C. Klein, M. Borg, J. Andersen, M. De Santis, Y. Gauthier, C. Konvicka, M. Schmid, and P. Varga, "Two-dimensional Oxide on Pd(111)," *Physical Review Letters*, vol. 88, p. 246103, Jun 17 2002.

[66] Z. H. Qin, M. Lewandowski, Y. N. Sun, S. Shaikhutdinov, and H. J. Freund, "Encapsulation of Pt Nanoparticles as a Result of Strong Metal-Support Interaction with $Fe_3O_4$ (111)," *Journal of Physical Chemistry C*, vol. 112, pp. 10209–10213, Jul 10 2008.

[67] M. Lewandowski, Y. N. Sun, Z. H. Qin, S. Shaikhutdinov, and H. J. Freund, "Promotional Effect of Metal Encapsulation on Reactivity of Iron Oxide Supported Pt Catalysts," *Applied Catalysis A - General*, vol. 391, pp. 407–410, Jan 4 2011.

[68] C. J. Powell, "Recommended Auger Parameters for 42 Elemental Solids," *Journal of Electron Spectroscopy and Related Phenomena*, vol. 185, pp. 1–3, Mar 2012.

[69] N. McIntyre and D. Zetaruk, "X-ray Photoelectron Spectroscopic Studies of Iron-Oxides," *Analytical Chemistry*, vol. 49, no. 11, pp. 1521–1529, 1977.

[70] S. Karlsson, C. Norberg, O. Nilsson, S. Hogberg, A. Elfarras, C. Nordling, and K. Siegbahn, "Electron Binding Energies in Platinum," *Arkiv for Fysik*, vol. 38, no. 4, p. 341, 1968.

[71] D. Hawn and B. Dekoven, "Deconvolution as a Correction for Photoelectron Inelastic Energy-Losses in the Core Level XPS Spectra of Iron-Oxides," *Surface and Interface Analysis*, vol. 10, pp. 63–74, Mar 1987.

[72] M. Oku and K. Hirokawa, "X-rays Photoelectron-Spectroscopy of $Co_3O_4$, $Fe_3O_4$, $Mn_3O_4$ and Related Compounds," *Journal of Electron Spectroscopy and Related Phenomena*, vol. 8, no. 6, pp. 475–481, 1976.

[73] H. Konno and M. Nagayama, "X-ray Photoelectron-Spectra of Hexavalent Iron," *Journal of Electron Spectroscopy and Related Phenomena*, vol. 18, no. 4, pp. 341–343, 1980.

[74] D. Haycock, D. Urch, C. Nicholls, and M. Kasrai, "Electronic-Structure of Magnesium-Hydroxide (Brucite) Using X-ray Emission, X-ray Photelectron, and Auger Spectroscopy," *Journal of the Chemical Society - Dalton Transactions*, no. 12, pp. 1791–1796, 1978.

[75] E. Carrasco, M. A. Brown, M. Sterrer, H.-J. Freund, K. Kwapien, M. Sierka, and J. Sauer, "Thickness-Dependent Hydroxylation of MgO(001) Thin Films," *Journal of Physical Chemistry C*, vol. 114, pp. 18207–18214, Oct 28 2010.

[76] K. Wandelt, "Photoemission Studies of Adsorbed Oxygen and Oxide Layers," *Surface Science Reports*, vol. 2, pp. 1–121, Sept. 1982.

[77] T. Schedel-Niedrig, W. Weiss, and R. Schlögl, "Electronic Structure of Ultrathin Ordered Iron Oxide Films Grown Onto Pt(111)," *Physical Review B*, vol. 52, pp. 17449–17460, Dec 15 1995.

[78] Y.-N. Sun, *Enhanced Reactivity of Ultrathhin Oxide Films in Oxidation Reactions: Back to 'Electronic Theory of Catalysis'.* PhD thesis, Freie Universität Berlin, 2010.

[79] J. Knudsen, L. R. Merte, L. C. Grabow, F. M. Eichhorn, S. Porsgaard, H. Zeuthen, R. T. Vang, E. Laegsgaard, M. Mavrikakis, and F. Besenbacher, "Reduction of FeO/Pt(111) Thin Films by Exposure to Atomic Hydrogen," *Surface Science*, vol. 604, pp. 11–20, Jan 1 2010.

[80] J. Goniakowski, C. Noguera, L. Giordano, and G. Pacchioni, "Adsorption of Metal Adatoms on FeO(111) and MgO(111) Monolayers: Effects of Charge State of Adsorbate on Rumpling of Supported Oxide Film," *Physical Review B*, vol. 80, p. 125403, Sep 2009.

[81] F. Ringleb, Y. Fujimori, H.-F. Wang, H. Ariga, E. Carrasco, M. Sterrer, H.-J. Freund, L. Giordano, G. Pacchioni, and J. Goniakowski, "Interaction of Water with FeO(111)/Pt(111): Environmental Effects and Influence of Oxygen," *Journal of Physical Chemistry C*, vol. 115, pp. 19328–19335, Oct 6 2011.

[82] M. A. Brown, Y. Fujimori, F. Ringleb, X. Shao, F. Stavale, N. Nilius, M. Sterrer, and H.-J. Freund, "Oxidation of Au by Surface OH: Nucleation and Electronic Structure of Gold on Hydroxylated MgO(001)," *Journal of the American Chemical Society*, vol. 133, pp. 10668–10676, Jul 13 2011.

[83] S. Wang, S. Liu, J. Guo, and Q. Guo, "Surface Electronic Structure and Morphology of Silver on Iron Oxide Films," *Surface Science*, vol. 607, pp. 124–129, Jan 2013.

[84] L. Giordano, G. Pacchioni, J. Goniakowski, N. Nilius, E. D. L. Rienks, and H.-J. Freund, "Charging of Metal Adatoms on Ultrathin Oxide Films: Au and Pd on FeO/Pt(111)," *Physical Review Letters*, vol. 101, p. 026102, Jul 11 2008.

[85] C. Lemire, R. Meyer, S. Shaikhutdinov, and H. Freund, "CO Adsorption on Oxide Supported Gold: From Small Clusters to Monolayer Islands and Three-Dimensional Nanoparticles," *Surface Science*, vol. 552, pp. 27–34, Mar 10 2004.

[86] M. Lewandowski, I. M. N. Groot, S. Shaikhutdinov, and H. J. Freund, "Scanning Tunneling Microscopy Evidence for the Mars-van KrevelenType Mechanism of Low Temperature CO Oxidation on an FeO(1 1 1) Film on Pt(1 1 1)," *Catalysis Today*, vol. 181, pp. 52–55, Feb 12 2012.

[87] L. Giordano, M. Baistrocchi, and G. Pacchioni, "Bonding of Pd, Ag, and Au Atoms on MgO(100) Surfaces and MgO/Mo(100) Ultra-Thin Films: A Comparative DFT Study," *Physical Review B*, vol. 72, p. 115403, Sep 2005.

[88] K. Honkala and H. Hakkinen, "Au Adsorption on Regular and Defected Thin MgO(100) Films Supported by Mo," *Journal of Physical Chemistry C*, vol. 111, pp. 4319–4327, Mar 22 2007.

[89] L. Savio, E. Celasco, L. Vattuone, M. Rocca, and P. Senet, "MgO/Ag(100): Confined Vibrational Modes in the Limit of Ultrathin Films," *Physical Review B*, vol. 67, p. 075420, Feb 15 2003.

[90] G. Pacchioni, L. Giordano, and M. Baistrocchi, "Charging of Metal Atoms on Ultrathin MgO/Mo(100) Films," *Physical Review Letters*, vol. 94, p. 226104, Jun 10 2005.

[91] M. Sterrer, T. Risse, M. Heyde, H.-P. Rust, and H.-J. Freund, "Crossover From Three-Dimensional to Two-Dimensional Geometries of Au Nanostructures on Thin MgO(001) Films: A Confirmation of Theoretical Predictions," *Physical Review Letters*, vol. 98, p. 206103, May 18 2007.

[92] D. E. Starr, C. Weis, S. Yamamoto, A. Nilsson, and H. Bluhm, "$NO_2$ Adsorption on Ag(100) Supported MgO(100) Thin Films: Controlling the Adsorption State with Film Thickness," *Journal of Physical Chemistry C*, vol. 113, pp. 7355–7363, Apr 30 2009.

[93] P. Broqvist and H. Groenbeck, "Effects of the Metal in the Adsorption of $NO_2$ on Platinum Supported BaO Films," *Surface Science*, vol. 600, pp. L214–L218, Aug 15 2006.

[94] A. Hellman and H. Groenbeck, "Activation of $Al_2O_3$ by a Long-Ranged Chemical Bond Mechanism," *Physical Review Letters*, vol. 100, p. 116801, Mar 21 2008.

[95] W. OBrien, J. Jia, Q. Dong, T. Callcott, J. Rubensson, D. Mueller, and D. Ederer, "Intermediate Coupling in $L_2$-$L_3$ Core Excitons of MgO, $Al_2O_3$, and $SiO_2$," *Physical Review B*, vol. 44, pp. 1013–1018, Jul 15 1991.

[96] O. Madelung, U. Rössler, and M. Schulz, eds., *Landolt-Börnstein - Group III Condensed Matter; Volume 41B*. SpringerMaterials - The Landolt-Börnstein Database.

[97] M. Wu, J. Corneille, C. Estrada, J. He, and D. Goodman, "Synthesis and Characterization of Ultra-Thin MgO Films on Mo(100)," *Chemical Physics Letters*, vol. 182, pp. 472–478, Aug 9 1991.

[98] *GESTIS Datenbank.* `http://gestis.itrust.de/nxt/gateway.dll/gestis_de/001210.xml?f=templates$fn=default.htm$3.0`.

[99] T. König, *Investigation of Defects on MgO Films grown on Ag(001) - A Combined Dynamic Force and Scanning Tunneling Microscopy Study*. PhD thesis, Technische Universität Berlin, 2010.

[100] P. Tasker, "Stablity of Ionic-Crystal Surfaces," *Journal of Physics C - Solid State Physics*, vol. 12, no. 22, pp. 4977–4984, 1979.

[101] G. Haas, A. Menck, H. Brune, J. Barth, J. Venables, and K. Kern, "Nucleation and Growth of Supported Clusters at Defect Sites: Pd/MgO(001)," *Physical Review B*, vol. 61, pp. 11105–11108, Apr 15 2000.

[102] S. Benedetti, P. Myrach, A. di Bona, S. Valeri, N. Nilius, and H.-J. Freund, "Growth and Morphology of Metal Particles on MgO/Mo(001): A Comparative STM and Diffraction Study," *Physical Review B*, vol. 83, p. 125423, Mar 23 2011.

[103] S. Abbet, A. Sanchez, U. Heiz, and W. Schneider, "Tuning the Selectivity of Acetylene Polymerization Atom by Atom," *Journal of Catalysis*, vol. 198, pp. 122–127, Feb 15 2001.

[104] T. Ito and J. Lunsford, "Synthesis of Ethylene and Ethane by Partial Oxidation of Methane over Lithium-Doped Magnesium-Oxide," *Nature*, vol. 314, no. 6013, pp. 721–722, 1985.

[105] C. Shi, M. Xu, M. Rosynek, and J. Lunsford, "Origing of Kinetic Isotope Effects during the Oxidative Coupling of Methane over a $Li^+MgO$ Catalyst," *Journal of Physical Chemistry*, vol. 97, pp. 216–222, Jan 7 1993.

[106] T. Shido, Y. Asakura, and Y. Iwasawa, "The Hydrogen-Exchange Reaction of Surface Deuteroxyl Groups of MgO with $H_2$," *Journal of the Chemical Society - Faraday Transactions I*, vol. 85, pp. 441–453, Feb 1989.

[107] T. Shido, K. Asakura, and Y. Iwasawa, "Reactant-Promoted Reaction-Mechanism for Catalytic Water Gas Shift Reaction on MgO," *Journal of Catalysis*, vol. 122, pp. 55–67, Mar 1990.

[108] P. Mars, J. Scholten, and P. Zwietering, "The Catalytic Decomposition of Formic Acid," *Advances in Catalysis*, vol. 14, pp. 35–113, 1963.

[109] P. Eckerlin, H. Kandler, K.-H. Hellwege, and A. M. Hellwege, "Landolt-Börnstein - Group III Condensed Matter 2.1 Table of the Structures of Elements," vol. 6.

[110] H. Schultz and H. Ullmaier, "Landolt-Börnstein - Group III Condensed Matter 2.2 bcc Metals," vol. 25.

[111] S. Benedetti, P. Torelli, S. Valeri, H. M. Benia, N. Nilius, and G. Renaud, "Structure and Morphology of Thin MgO Films on Mo(001)," *Physical Review B*, vol. 78, p. 195411, Nov 2008.

[112] J. Stejskal, J. Prokes, and I. Sapurina, "The Reduction of Silver Ions with Polyaniline: The Effect of the Type of Polyaniline and the Mole Ratio of the Reagents," *Materials Letters*, vol. 63, pp. 709–711, Mar 31 2009.

[113] G. Ertl, H. Knözinger, F. Schüth, and J. Weitkamp, eds., *Handbook of Heterogeneous Catalysis*. Wiley-VHC, 2008.

[114] U. Heiz and W. Schneider, "Nanoassembled Model Catalysts," *Journal of Physics D-Applied Physics*, vol. 33, pp. R85–R102, Jun 7 2000.

[115] J. Wollschlager, D. Erdos, and K. Schroder, "The Formation of Mosaics During the Reactive Growth of MgO Films on Ag(100)," *Surface Science*, vol. 402, pp. 272–276, May 15 1998. 17th European Conference on Surface Science, Enschede, Netherlands, Sep 16-19, 1997.

[116] J. Serafin and C. Friend, "Inhibition of C-H and C-O Bond Activation by Surface Oxygen - Stabilization of Surface Phenoxide in the Reaction of Phenol in Oxygen-Precovered Mo(110)," *Journal of the American Chemical Society*, vol. 111, pp. 4233–4239, Jun 7 1989.

[117] N. McIntyre, D. Johnston, L. Coatsworth, R. Davidson, and J. Brown, "X-ray Photoelectron Spectroscopic Studies of Thin-Film Oxides of Cobalt and Molybdenum," *Surface and Interface Analysis*, vol. 15, pp. 265–272, Apr 1990.

[118] D. Sarma and C. Rao, "XPES Studies of Oxides of $2^{nd}$-Row and $3^{rd}$-Row Transition-Metals Including Rare-Earths," *Journal of Electron Spectroscopy and Related Phenomena*, vol. 20, no. 1-2, pp. 25–45, 1980.

[119] T. Patterson, J. Carver, D. Leyden, and D. Hercules, "Surface Study of Cobalt-Molybena-Alumina Catalysts Using X-ray Photelectron-Spectroscopy," *Journal of Physical Chemistry*, vol. 80, no. 15, pp. 1700–1708, 1976.

[120] F. Jahan and B. Smith, "Investigation of Solar Selective and Microstructural Properties of Molybdenum Black Immersion Coatings on Cobalt Substrates," *Journal of Materials Science*, vol. 27, pp. 625–636, Feb 1 1992.

[121] T. Fleisch and G. Mains, "An XPS Study of the UV Reduction and Photochromism of MoO$_3$ and WO$_3$," *Journal of Chemical Physics*, vol. 76, no. 2, pp. 780–786, 1982.

[122] C. Tenretnoel, J. Verbist, and Y. Gobillon, "Oxidation-States of Molybdenum Oxides and Mixed-Oxide C2MO1 by Photelectron-Spectroscopy," *Journal de Microscopie et de Spectroscopie Electroniques*, vol. 1, no. 2, pp. 255–262, 1976.

[123] B. Brox and I. Olefjord, "ECSA Studies of MoO$_2$ and MoO$_3$," *Surface and Interface Analysis*, vol. 13, pp. 3–6, Oct 1988.

[124] M. Iwamoto, Y. Yoda, N. Yamazoe, and T. Seiama, "Study of Metal-Oxide Catalysts by Temperature Programmed Desorption .4. Oxygen-Adsorption on Various Metal-Oxides," *Journal of Physical Chemistry*, vol. 82, no. 24, pp. 2564–2570, 1978.

[125] M. A. Brown, F. Ringleb, Y. Fujimori, M. Sterrer, H.-J. Freund, G. Preda, and G. Pacchioni, "Initial Formation of Positively Charged Gold on MgO(001) Thin Films: Identification by Experiment and Structural Assignment by Theory," *Journal of Physical Chemistry C*, vol. 115, pp. 10114–10124, May 26 2011.

[126] S. Altieri, L. Tjeng, F. Voogt, A. Hibma, and G. Sawatzky, "Reduction of Coulomb and Charge-Transfer Energies in Oxide Films on Metals," *Physical Review B*, vol. 59, pp. R2517–R2520, Jan 15 1999.

[127] G. Agostini, E. Groppo, A. Piovano, R. Pellegrini, G. Leofanti, and C. Lamberti, "Preparation of Supported Pd Catalysts: From the Pd Precursor Solution to the Deposited Pd$^{2+}$ Phase," *Langmuir*, vol. 26, pp. 11204–11211, Jul 6 2010.

[128] H. Blaser, A. Indolese, A. Schnyder, H. Steiner, and M. Studer, "Supported Palladium Catalysts for Fine Chemicals Synthesis," *Journal of Molecular Catalysis A - Chemical*, vol. 173, pp. 3–18, Sep 10 2001.

[129] V. Polshettiwar and A. Molnar, "Silica-Supported Pd Catalysts for Heck Coupling Reactions," *Tetrahedron*, vol. 63, pp. 6949–6976, Jul 23 2007.

[130] M. Seki, "Recent Advances in Pd/C-Catalyzed Coupling Reactions," *Synthesis - Stuttgart*, pp. 2975–2992, Sep 18 2006.

[131] M. Wagner, K. Kohler, L. Djakovitch, S. Weinkauf, V. Hagen, and M. Muhler, "Heck Reactions Catalyzed by Oxide-Supported Palladium - Structure-Activity Relationships," *Topics in Catalysis*, vol. 13, no. 3, pp. 319–326, 2000. 5th Symposium on Heterogeneous Catalysis and Fine Chemicals, Lyon, France, Aug 30 - Sep 03, 1999.

[132] R. Varma, K. Naicker, and P. Liesen, "Palladium Chloride and Tetraphenylphosphonium Bromide Intercalated Clay as a New Catalyst for the Heck Reaction," *Tetrahedron Letters*, vol. 40, pp. 2075–2078, Mar 12 1999.

[133] A. Biffis, M. Zecca, and M. Basato, "Palladium Metal Catalysts in Heck C-C Coupling Reactions," *Journal of Molecular Catalysis A - Chemical*, vol. 173, pp. 249–274, Sep 10 2001.

[134] L. Yin and J. Liebscher, "Carbon-Carbon Coupling Reactions Catalyzed by Heterogeneous Palladium Catalysts," *Chemical Reviews*, vol. 107, pp. 133–173, Jan 2007.

[135] C. Henry, C. Chapon, C. Duriez, and S. Giorgio, "Growth and Morphology of Palladium Particles Epitaxially Deposited on a MgO(100) Surface," *Surface Science*, vol. 253, no. 1-3, pp. 177 – 189, 1991.

[136] G. Renaud, R. Lazzari, C. Revenant, A. Barbier, M. Noblet, O. Ulrich, F. Leroy, J. Jupille, Y. Borensztein, C. Henry, J. Deville, F. Scheurer, J. Mane-Mane, and O. Fruchart, "Real-Time Monitoring of Growing Nanoparticles," *Science*, vol. 300, pp. 1416–1419, May 30 2003.

[137] C. Becker and C. Henry, "Cluster Size Dependent Kinetics for the Oxidation of CO on a Pd/MgO(100) Model Catalyst," *Surface Science*, vol. 352-354, no. 0, pp. 457 – 462, 1996. Proceedings of the 15th European Conference on Surface Science.

[138] P. Nolte, A. Stierle, N. Kasper, N. Y. Jin-Phillipp, N. Jeutter, and H. Dosch, "Reversible Shape Changes of Pd Nanoparticles on MgO(100)," *Nano Letters*, vol. 11, pp. 4697–4700, Nov 2011.

[139] M. Sterrer, T. Risse, L. Giordano, M. Heyde, N. Nilius, H.-P. Rust, G. Pacchioni, and H.-J. Freund, "Palladium Monomers, Dimers, and Trimers on the MgO(001) Surface Viewed Individually," *Angewandte Chemie - International Edition*, vol. 46, no. 45, pp. 8703–8706, 2007.

[140] M. Sterrer, T. Risse, U. M. Pozzoni, L. Giordano, M. Heyde, H.-P. Rust, G. Pacchioni, and H.-J. Freund, "Control of the Charge State of Metal Atoms on Thin MgO Films," *Physical Review Letters*, vol. 98, p. 096107, Mar 2 2007.

[141] C. Xu, W. Oh, G. Liu, D. Kim, and D. Goodman, "Characterization of Metal Clusters (Pd and Au) Supported on Various Metal Oxide Surfaces (MgO and TiO$_2$)," *Journal of Vacuum Science & Technology A - Vacuum Surfaces and Films*, vol. 15, pp. 1261–1268, May-Jun 1997. 43rd American-Vacuum-Society Symposium, Philadelphia, PA, Oct 14-18, 1996.

[142] Q. Guo and P. J. Moller, "Initial Interaction of Pd with MgO(100) Films," *Journal of Physical Chemistry C*, vol. 114, pp. 18167–18172, Oct 28 2010.

[143] V. Nasluzov, V. Rivanenkov, A. Gordienko, K. Neyman, U. Birkenheuer, and N. Rosch, "Cluster Embedding in an Elastic Polarizable Environment: Density Functional Study of Pd Atoms Adsorbed at Oxygen Vacancies of MgO(001)," *Journal of Chemical Physics*, vol. 115, pp. 8157–8171, Nov 1 2001.

[144] L. Giordano, J. Goniakowski, and G. Pacchioni, "Characteristics of Pd Adsorption on the MgO(100) Surface: Role of Oxygen Vacancies," *Physical Review B*, vol. 64, p. 075417, Aug 15 2001.

[145] L. Xu, G. Henkelman, C. Campbell, and H. Jonsson, "Small Pd Clusters, up to the Tetramer at Least, are Highly Mobile on the MgO(100) Surface," *Physical Review Letters*, vol. 95, p. 146103, Sep 30 2005.

[146] G. Barcaro, A. Fortunelli, F. Nita, and R. Ferrando, "Diffusion of Palladium Clusters on Magnesium Oxide," *Physical Review Letters*, vol. 95, p. 246103, Dec 9 2005.

[147] G. Barcaro, A. Fortunelli, G. Rossi, F. Nita, and R. Ferrando, "Epitaxy, Truncations, and Overhangs in Palladium Nanoclusters Adsorbed on MgO(001)," *Physical Review Letters*, vol. 98, p. 156101, Apr 13 2007.

[148] G. Rossi, C. Mottet, F. Nita, and R. Ferrando, "Global Optimization Study of Small (10 ≤ N ≤ 120) Pd Clusters Supported on MgO(100)," *Journal of Physical Chemistry B*, vol. 110, pp. 7436–7442, Apr 13 2006.

[149] B. Huber, P. Koskinen, H. Hakkinen, and M. Moseler, "Oxidation of Magnesia-Supported Pd-Clusters Leads to the Ultimate Limit of Epitaxy with a Catalytic Function," *Nature Materials*, vol. 5, pp. 44–47, Jan 2006.

[150] S. Bertarione, D. Scarano, A. Zecchina, V. Johanek, J. Hoffmann, S. Schauermann, M. Frank, J. Libuda, G. Rupprechter, and H. Freund, "Surface Reactivity of Pd Nanoparticles Supported on Polycrystalline Substrates as Compared to Thin Film Model Catalysts: Infrared Study of CO Adsorption," *Journal of Physical Chemistry B*, vol. 108, pp. 3603–3613, Mar 18 2004.

[151] H. Borchert, B. Jürgens, V. Zielasek, G. Rupprechter, S. Giorgio, C. Henry, and M. Bäumer, "Pd Nanoparticles with Highly Defined Structure on MgO as Model Catalysts: An FTIR Study of the Interaction with CO, $O_2$, and $H_2$ under Ambient Conditions," *Journal of Catalysis*, vol. 247, no. 2, pp. 145 – 154, 2007.

[152] Y. Ryndin, R. Hicks, A. Bell, and Y. Yermakov, "Effects of Metal-Support Interactions on the Synthesis of Methanol over Palladium," *Journal of Catalysis*, vol. 70, no. 2, pp. 287 – 297, 1981.

[153] J. Driessen, E. Poels, J. Hindermann, and V. Ponec, "On the Selectivity of Palladium Catalysts in Synthesis Gas Reactions," *Journal of Catalysis*, vol. 82, no. 1, pp. 26 – 34, 1983.

[154] S. Bertarione, D. Scarano, A. Zecchina, V. Johanek, J. Hoffmann, S. Schauermann, J. Libuda, G. Rupprechter, and H. Freund, "Surface Reactivity of Pd Nanoparticles Supported on Polycrystalline Substrates as Compared to Thin Film Model Catalysts: Infrared Study of $CH_3OH$ Adsorption," *Journal of Catalysis*, vol. 223, no. 1, pp. 64 – 73, 2004.

[155] S. Galvagno, A. Donato, G. Neri, and R. Pietropaolo, "Hydrogenation of Phenol to Cyclohexanone over Pd/MgO," *Journal of Chemical Technology and Biotechnology*, vol. 51, no. 2, pp. 145–153, 1991.

[156] N. Mahata and V. Vishwanathan, "Influence of Palladium Precursors on Structural Properties and Phenol Hydrogenation Characteristics of Supported Palladium Catalysts," *Journal of Catalysis*, vol. 196, no. 2, pp. 262 – 270, 2000.

[157] P. Claus, H. Berndt, C. Mohr, J. Radnik, E. Shin, and M. Keane, "Pd/MgO: Catalyst Characterization and Phenol Hydrogenation Activity," *Journal of Catalysis*, vol. 192, pp. 88–97, May 15 2000.

[158] E. Groppo, S. Bertarione, F. Rotunno, G. Agostini, D. Scarano, R. Pellegrini, G. Leofanti, A. Zecchina, and C. Lamberti, "Role of the Support in Determining the Vibrational Properties of Carbonyls Formed on Pd Supported on $SiO_2$-$Al_2O_3$, $Al_2O_3$, and MgO," *Journal of Physical Chemistry C*, vol. 111, pp. 7021–7028, May 17 2007.

[159] M. Kappers, C. Dossi, R. Psaro, S. Recchia, and A. Fusi, "DRIFT Study of CO Chemisorption on Organometallics-Derived Pd/MgO Catalysts: The Effect of Chlorine," *Catalysis Letters*, vol. 39, no. 3-4, pp. 183–189, 1996.

[160] H. Aytam, V. Akula, K. Janmanchi, S. Kamaraju, K. Panja, K. Gurram, and J. Niemantsverdriet, "Characterization and Reactivity of Pd/MgO and Pd/*gamma*-$Al_2O_3$ Catalysts in the Selective Hydrogenolysis of $CCl_2F_2$," *Journal of Physical Chemistry B*, vol. 106, pp. 1024–1031, Feb 7 2002.

[161] M. A. Brown, E. Carrasco, M. Sterrer, and H.-J. Freund, "Enhanced Stability of Gold Clusters Supported on Hydroxylated MgO(001) Surfaces," *Journal of the American Chemical Society*, vol. 132, no. 12, pp. 4064–4065, 2010. PMID: 20199021.

[162] H.-F. Wang, H. Ariga, R. Dowler, M. Sterrer, and H.-J. Freund, "Surface Science Approach to Catalyst Preparation - Pd Deposition onto Thin $Fe_3O_4$(111) Films From $PdCl_2$ Precursor," *Journal of Catalysis*, vol. 286, pp. 1–5, Feb 2012.

[163] H.-F. Wang, W. E. Kaden, R. Dowler, M. Sterrer, and H.-J. Freund, "Model Oxide-Supported Metal Catalysts - Comparison of Ultrahigh Vacuum and Solution Based Preparation of Pd Nanoparticles on a Single-Crystalline Oxide Substrate," *Physical Chemistry Chemical Physics*, vol. 14, no. 32, pp. 11525–11533, 2012.

[164] K. P. de Jong, ed., *Synthesis of Solid Catalysts*. Wiley-VHC, 2009.

[165] M. Toebes, J. van Dillen, and Y. de Jong, "Synthesis of Supported Palladium Catalysts," *Journal of Molecular Catalysis A - Chemical*, vol. 173, pp. 75–98, Sep 10 2001.

[166] J. Brunelle, "Preparation of Catalysts by Metallic Complex Adsorption on Mineral Oxides," *Pure and Applied Chemistry*, vol. 50, pp. 1211–1229, 1978.

[167] L. Bonneviot, O. Legendre, M. Kermarec, D. Olivier, and M. Che, "Characterization by UV-VIS-NIR Reflectance Spectroscopy of the Exchange Sites of Nickel on Silica," *Journal of Colloid and Interface Science*, vol. 134, pp. 534–547, 1990.

[168] C. Contescu, C. Sivaraj, and J. Schwarz, "Selective Ion-Exchange of Palladium on Alumina Silica Composite Oxides," *Applied Catalysis*, vol. 74, pp. 95–108, Jun 27 1991.

[169] J. J. Cruywagen and R. J. Kriek, "Complexation of Palladium(II) with Chloride and Hydroxide," *Journal of Coordination Chemistry*, vol. 60, pp. 439–447, Feb 20 2007.

[170] *Preparation of Catalysts VII, Volume 118*. Maggi, R. and Martens, J.A. and Poncelet, G. and Grange, P. and Jacobs, P.A. and Delmon, B., 1998.

[171] S. Troitskii, A. Chuvilin, D. Kochubei, B. Novgorodov, V. Kolomiichuk, and V. Likholobov, "Structure of Polynuclear Palladium(II) Hydroxocomplexes Formed upon Alkaline Hydrolysis of Palladium(II) Chloride Complexes," *Russian Chemical Bulletin*, vol. 44, pp. 1822–1826, Oct 1995.

[172] P. Patnaik, *Handbook of Inorganic Chemicals*. McGraw-Hill, 2003.

[173] D. Simpson, T. Bredow, R. Smart, and A. Gerson, "Mechanisms of Acidic Dissolution at the MgO(100) Surface," *Surface Science*, vol. 516, pp. 134–146, Sep 10 2002.

[174] K. Sangwal, T. Patel, and M. Kotak, "Kinetics and Mechanism of Dissolution of MgO Crystals," *Journal of Materials Science*, vol. 14, no. 8, pp. 1869–1876, 1979.

[175] A. Fedorockova and P. Raschman, "Effects of pH and Acid Anions on the Dissolution Kinetics of MgO," *Chemical Engineering Journal*, vol. 143, pp. 265–272, Sep 15 2008.

[176] M. Suarez and R. Compton, "Dissolution of Magnesium Oxide in Aqueous Acid: An Atomic Force Microscopy Study," *Journal of Physical Chemistry B*, vol. 102, pp. 7156–7162, Sep 10 1998.

[177] O. Fruhwirth, G. Herzog, I. Hollerer, and A. Rachetti, "Dissolution and Hydration Kinetics of MgO," *Surface Technology*, vol. 24, no. 3, pp. 301–317, 1985.

[178] D. Vermilyea, "Dissolution of MgO and $MgO(OH)_2$ in Aqueous Solutions," *Journal of the Electrochemical Society*, vol. 116, no. 9, pp. 1179–1183, 1969.

[179] S. Holt, C. Jones, G. Watson, A. Crossley, C. Johnston, C. Sofield, and S. Myhra, "Surface Modification of MgO Substrates from Aqueous Exposure: An Atomic Force Microscopy Study," *Thin Solid Films*, vol. 292, pp. 96–102, Jan 5 1997.

[180] J. Mejias, A. Berry, K. Refson, and D. Fraser, "The Kinetics and Mechanism of MgO Dissolution," *Chemical Physics Letters*, vol. 314, pp. 558–563, Dec 10 1999.

[181] R. Hacquart and J. Jupille, "Hydrated MgO Smoke Crystals From Cubes to Octahedra," *Chemical Physics Letters*, vol. 439, no. 1-3, pp. 91 – 94, 2007.

[182] R. Hacquart and J. Jupille, "Morphology of MgO Smoke Crystallites upon Etching in Wet Environment," *Journal of Crystal Growth*, vol. 311, pp. 4598–4604, Oct 15 2009.

[183] S. Russo and C. Noguera, "Acido-Basic Properties of Simple Oxide Surfaces .1. Magnesium-Oxide," *Surface Science*, vol. 262, pp. 245–258, Feb 1 1992.

[184] P. Thissen, V. Thissen, S. Wippermann, Y. J. Chabal, G. Grundmeier, and W. G. Schmidt, "pH-Dependent Structure and Energetics of $H_2O$/MgO(100)," *Surface Science*, vol. 606, pp. 902–907, Jun 2012.

[185] N. F. Kosenko, L. A. Vinogradova, and M. A. Smirnova, "Effect of Mechanical Processing on the Dissolution Rate of MgO," *Inorganic Materials*, vol. 44, pp. 842–845, Aug 2008.

[186] N. Deleeuw, G. Watson, and S. Parker, "Atomistic Simulation of the Effect of Dissociative Adsorption of Water on the Surface-Structure and Stability of Calcium and Magnesium-Oxide," *Journal of Physical Chemistry*, vol. 99, pp. 17219–17225, Nov 23 1995.

[187] P. Geysermans, F. Finocchi, J. Goniakowski, R. Hacquart, and J. Jupille, "Combination of (100), (110) and (111) Facets in MgO Crystals Shapes from Dry to Wet Environment," *Physical Chemistry Chemical Physics*, vol. 11, no. 13, pp. 2228–2233, 2009.

[188] T. K. Ghosh and F. J. P. Clarke, "Etching and Polishing Studies on Magnesium Oxide Single Crystals," *British Journal of Applied Physics*, vol. 12, no. 2, p. 44, 1961.

[189] M. Seah, "Quantitative Auger-Electron Spectroscopy and Electron Ranges," *Surface Science*, vol. 32, no. 3, p. 703–728, 1972.

[190] A. Akkerman, T. Boutboul, A. Breskin, R. Chechik, A. Gibrekhterman, and Y. Lifshitz, "Inelastic Electron Interactions in the Energy Range 50 eV to 10 keV in Insulators: Alkali Halides and Metal Oxides," *Physica Status Solidi B - Basic Research*, vol. 198, pp. 769–784, Dec 1996.

[191] S. Tanuma, C. Powell, and D. Penn, "Calculations of Electron Inelastic Mean Free Paths .5. Data for 14 Organic-Compounds Over the 50-2000eV Range," *Surface and Interface Analysis*, vol. 21, pp. 165–176, Mar 1994.

[192] C. Kwei, Y. Chen, C. Tung, and J. Wang, "Electron Inelastic Mean Free Paths for Plasmon Excitations and Interband-Transitions," *Surface Science*, vol. 293, pp. 202–210, Aug 20 1993.

[193] E. Kieseritzky, *Adaptation of a W-Band EPR Spectrometer to UHV Conditions*. PhD thesis, Fachbereich Biologie, Chemie, Pharmazie der Freien Universit¨at Berlin, 2010.

[194] R. L. Segall, R. S. C. Smart, and P. S. Turner, "Ionic Oxides: Distinction Between Mechanisms and Surface Roughening Effects in the Dissolution of Magnesium Oxide," *J. Chem. Soc., Faraday Trans. 1*, vol. 74, pp. 2907–2912, 1978.

[195] O. S. Pokrovsky and J. Schott, "Experimental Study of Brucite Dissolution and Precipitation in Aqueous Solutions: Surface Speciation and Chemical Affinity Control," *Geochimica et Cosmochimica Acta*, vol. 68, no. 1, pp. 31 – 45, 2004.

[196] D. Roth, P. Gelin, M. Primet, and E. Tena, "Catalytic Behaviour of Cl-Free and Cl-Containing Pd/Al$_2$O$_3$ Catalysts in the Total Oxidation of Methane at Low Temperature," *Applied Catalysis A - General*, vol. 203, pp. 37–45, Sep 18 2000.

[197] H. Oh, J. Yang, C. Costello, Y. Wang, S. Bare, H. Kung, and M. Kung, "Selective Catalytic Oxidation of CO: Effect of Chloride on Supported Au Catalysts," *Journal of Catalysis*, vol. 210, pp. 375–386, Sep 10 2002.

[198] C. Baatz, N. Decker, and U. Pruesse, "New Innovative Gold Catalysts Prepared by an Improved Incipient Wetness Method," *Journal of Catalysis*, vol. 258, pp. 165–169, Aug 15 2008.

[199] R. Gopinath, N. S. Babu, J. V. Kumar, N. Lingaiah, and P. S. S. Prasad, "Influence of Pd Precursor and Method of Preparation on Hydrodechlorination Activity of Alumina Supported Palladium Catalysts," *Catalysis Letters*, vol. 120, pp. 312–319, Jan 2008.

[200] S. Schintke, S. Messerli, M. Pivetta, F. Patthey, L. Libioulle, M. Stengel, A. De Vita, and W. Schneider, "Insulator at the Ultrathin Limit: MgO on Ag(001)," *Physical Review Letters*, vol. 87, p. 276801, Dec 31 2001.

[201] M. Bäumer and H. Freund, "Metal Deposits on Well-Ordered Oxide Films," *Progress in Surface Science*, vol. 61, pp. 127–198, Aug 1999.

[202] T. Schalow, B. Brandt, D. E. Starr, M. Laurin, S. K. Shaikhutdinov, S. Schauermann, J. Libuda, and H. J. Freund, "Particle Size Dependent Adsorption and Reaction Kinetics on Reduced and Partially Oxidized Pd Nanoparticles," *Physical Chemistry Chemical Physics*, vol. 9, no. 11, pp. 1347–1361, 2007.

[203] K. Kim, A. Gossmann, and N. Winograd, "X-ray Photelectron Spectroscopic Studies of Palladium Oxides and the Palladium-Oxygen Electrode," *Analytical Chemistry*, vol. 46, no. 2, pp. 197–200, 1974.

[204] C. Furlani, G. Mattogno, and V. Sessa, "X-ray Photoelectron Spectroscopy Characterization of Hydrated Palladium(II) Oxide Species Used in Catalysis," *Journal of the Less Common Metals*, vol. 102, no. 1, pp. 89 – 96, 1984.

[205] K. Otto, L. Haack, and J. deVries, "Identification of Two Types of Oxidized Palladium on $\gamma$-Alumina by X-ray Photoelectron Spectroscopy," *Applied Catalysis B: Environmental*, vol. 1, no. 1, pp. 1 – 12, 1992.

[206] T. Pillo, R. Zimmermann, P. Steiner, and S. Hufner, "The Electronic Structure of PdO Found by Photoemission (UPS and XPS) and Inverse Photoemission (BIS)," *Journal of Physics - Condensed Matter*, vol. 9, pp. 3987–3999, May 12 1997.

[207] C. Wagner and A. Joshi, "The Auger Parameter, Its Utility and Advantages: A Review," *Journal of Electron Spectroscopy and Related Phenomena*, vol. 47, no. 0, pp. 283 – 313, 1988.

[208] G. Hohlneicher, H. Pulm, and H.-J. Freund, "On the Separation of Initial and Final State Effects in Photoelectron Spectroscopy Using an Extension of the Auger-Parameter Concept," *Journal of Electron Spectroscopy and Related Phenomena*, vol. 37, no. 2, pp. 209 – 224, 1985.

[209] B. Richter, H. Kuhlenbeck, H. Freund, and P. Bagus, "Cluster Core-Level Binding-Energy Shifts: The Role of Lattice Strain," *Physical Review Letters*, vol. 93, p. 026805, Jul 9 2004.

[210] G. Kleiman, R. Landers, P. Nascente, and S. Decastro, "Auger Parameters and Screening Mechanisms in the 4d and 5d Metals," *Physical Review B*, vol. 46, pp. 4405–4413, Aug 15 1992.

[211] S. Oh, P. Mitchell, and R. Siewert, "Methane Oxidation over Alumina-Supported Noble-Metal Catalysts with and without Cerium Additives," *Journal of Catalysis*, vol. 132, pp. 287–301, Dec 1991.

[212] P. Salomonsson, S. Johansson, and B. Kasemo, "Methane Oxidation over $PdO_x$ - on the Mechanism for the Hysteresis in Activity and Oxygen-Content," *Catalysis Letters*, vol. 33, no. 1-2, pp. 1–13, 1995.

[213] J. McCarty, "Kinetics of PdO Combustion Catalysis," *Catalysis Today*, vol. 26, pp. 283–293, Dec 12 1995. International Workshop on Catalytic Combustion, TOKYO, JAPAN, APR 18-20, 1994.

[214] H. Gabasch, K. Hayek, B. Klotzer, A. Knop-Gericke, and R. Schlögl, "Carbon Incorporation in Pd(III) by Adsorption and Dehydrogenation of Ethene," *Journal of Physical Chemistry B*, vol. 110, pp. 4947–4952, Mar 16 2006.

[215] P. Albers, J. Pietsch, and S. Parker, "Poisoning and Deactivation of Palladium Catalysts," *Journal of Molecular Catalysis A - Chemical*, vol. 173, pp. 275–286, Sep 10 2001.

[216] M. Bowker and C. Morgan, "On Pd Carbide Formation and Vinyl Acetate Synthesis," *Catalysis Letters*, vol. 98, p. 67, Oct 2004.

[217] W. Unterberger, H. Gabasch, K. Hayek, and B. Klotzer, "Catalytic Oxidation of Ethene on Polycrystalline Palladium: Influence of the Oxidation State of the Surface," *Catalysis Letters*, vol. 104, pp. 1–8, Oct 2005.

[218] O. Balmes, A. Resta, D. Wermeille, R. Felici, M. E. Messing, K. Deppert, Z. Liu, M. E. Grass, H. Bluhm, R. van Rijn, J. W. M. Frenken, R. Westerstroem, S. Blomberg, J. Gustafson, J. N. Andersen, and E. Lundgren, "Reversible Formation of a $PdC_x$ Phase in Pd Nanoparticles upon CO and $O_2$ Exposure," *Physical Chemistry Chemical Physics*, vol. 14, no. 14, pp. 4796–4801, 2012.

[219] A. Borodzinki, "Selective Hydrogenation of Ethyne in Ethene-Rich Streams on Palladium Catalysts. Part 1. Effect of Changes to the Catalyst during Reaction," *Catalysis Reviews - Science and Engineering*, vol. 48, pp. 91–144, Apr-Jun 2006.

[220] G. M. Veith, A. R. Lupini, and N. J. Dudney, "Role of pH in the Formation of Structurally Stable and Catalytically Active $TiO_2$-Supported Gold Catalysts," *Journal of Physical Chemistry C*, vol. 113, pp. 269–280, Jan 8 2009.

[221] H.-J. Freund, G. Meijer, M. Scheffler, R. Schlögl, and M. Wolf, "CO Oxidation as a Prototypical Reaction for Heterogeneous Processes," *Angewandte Chemie - International Edition*, vol. 50, no. 43, pp. 10064–10094, 2011.

[222] I. Langmuir, "The Mechanism of the Catalytic Action of Platinum in the Reactions $2CO + O_2 = 2CO_2$ and $2H_2 + O_2 = 2H_2O$.," *Transactions of the Faraday Society*, vol. 17, pp. 0621–0654, Feb 1922.

[223] S. C. N. Hinshelwood, *The Kinetics of Chemical Change.* Clarendon Press, Oxford, 1940.

[224] E. T. and E. G., "Elementary Steps in the Catalytic Oxidation of Carbon Monoxide on Platinum Metals," *Advances in Catalysis*, vol. 28, pp. 1–78, 1979.

[225] H.-F. Wang, *Surface Science Approach to Catalyst Preparation: Palladium Deposition onto Iron Oxide Films from the Liquid Phase*. PhD thesis, Freie Universität Berlin, 2012.

[226] S. Shaikhutdinov, M. Heemeier, J. Hoffmann, I. Meusel, B. Richter, M. Bäumer, H. Kuhlenbeck, J. Libuda, H. Freund, R. Oldman, S. Jackson, C. Konvicka, M. Schmid, and P. Varga, "Interaction of Oxygen with Palladium Deposited on a Thin Alumina Film," *Surface Science*, vol. 501, pp. 270–281, Apr 1 2002.

[227] X. Xu and D. Goodman, "An Infrared and Kinetics-Study of CO Oxidation on Model Silica-Supported Palladium Catalysts From $10^{-9}$ to 15 Torr," *Journal of Physical Chemistry*, vol. 97, pp. 7711–7718, Jul 22 1993.

[228] M. Weber, "Science and Technology of Laser Glass," *Journal of Non-Crystalline Solids*, vol. 123, pp. 208–222, Aug 1990. $15^{th}$ International Congress on Glass, Leningrad, UdSSR, Jul 03-07, 1989.

[229] G. Partridge, "An Overwiew of Glass-Ceramics .1. Development and Principal Bulk Applications," *Glass Technology*, vol. 35, pp. 116–127, Jun 1994.

[230] H. B. W. Höland, *Glass-Ceramic Technology*. Wiley, 2012.

[231] C. Bianchini and P. Barbaro, "Recent Aspects of Asymmetric Catalysis by Immobilized Chiral Metal Catalysts," *Topics in Catalysis*, vol. 19, no. 1, pp. 17–32, 2002.

[232] C. C. H. Lin, K. A. Dambrowitz, and S. M. Kuznicki, "Evolving Applications of Zeolite Molecular Sieves," *Canadian Journal of Chemical Engineering*, vol. 90, pp. 207–216, Apr 2012.

[233] B. Yilmaz and U. Mueller, "Catalytic Applications of Zeolites in Chemical Industry," *Topics in Catalysis*, vol. 52, pp. 888–895, Jun 2009.

[234] J. He, X. Xu, J. Corneille, and D. Goodman, "X-ray Photoelectron Spectroscopic Characterization of Ultra-Thin Silicon-Oxide Films on a Mo(100) Surface," *Surface Science*, vol. 279, pp. 119–126, Dec 1 1992.

[235] W. Braun and H. Kuhlenbeck, "Chemical Structure of Ultrathhin Thermally Grown Oxides on a Si(100)-Wafer using Core Level Photoemission," *Surface Science*, vol. 180, pp. 279–288, Feb 1987.

[236] N. Mott, S. Rigo, F. Rochet, and A. Stoneham, "Oxidation of Silicon," *Philosophical Magazine B: Physics of Condensed, Matter, Statistical Mechanics, Electronic, Optical, and Magnetic Properties* , vol. 60, pp. 189–212, Aug 1989.

[237] M. Niwano, H. Katura, Y. Takeda, Y. Takakuwa, N. Miyamoto, and M. Maki, "Photoemission-Study of the $SiO_2$/Si Interface Structure of Thin Oxide Film on Vicinal Si(100) Surface," *Journal of Vacuum Science & Technology A - Vacuum Surfaces and Films*, vol. 10, pp. 339–343, Mar-Apr 1992.

[238] T. Schroeder, M. Adelt, B. Richter, M. Naschitzki, M. Baumer, and H. Freund, "Epitaxial Growth of $SiO_2$ on Mo(112)," *Surface Review and Letters*, vol. 7, pp. 7–14, Feb-Apr 2000.

[239] D. Loeffler, J. J. Uhlrich, M. Baron, B. Yang, X. Yu, L. Lichtenstein, L. Heinke, C. Buechner, M. Heyde, S. Shaikhutdinov, H. J. Freund, R. Wlodarczyk, M. Sierka, and J. Sauer, "Growth and Structure of Crystalline Silica Sheet on Ru(0001)," *Physical Review Letters*, vol. 105, p. 146104, Sep 30 2010.

[240] M. Heyde, S. Shaikhutdinov, and H. J. Freund, "Two-Dimensional Silica: Crystalline and Vitreous," *Chemical Physics Letters*, vol. 550, pp. 1–7, Oct 22 2012.

[241] B. Yang, W. E. Kaden, X. Yu, J. A. Boscoboinik, Y. Martynova, L. Lichtenstein, M. Heyde, M. Sterrer, R. Wlodarczyk, M. Sierka, J. Sauer, S. Shaikhutdinov, and H.-J. Freund, "Thin Silica Films on Ru(0001): Monolayer, Bilayer and Three-Dimensional Networks of $SiO_4$ Tetrahedra," *Physical Chemistry Chemical Physics*, vol. 14, no. 32, pp. 11344–11351, 2012.

[242] R. Wlodarczyk, M. Sierka, J. Sauer, D. Loeffler, J. J. Uhlrich, X. Yu, B. Yang, I. M. N. Groot, S. Shaikhutdinov, and H. J. Freund, "Tuning the Electronic Structure of Ultrathin Crystalline Silica Films on Ru(0001)," *Physical Review B*, vol. 85, p. 085403, Feb 2 2012.

[243] X. Yu, B. Yang, J. A. Boscoboinik, S. Shaikhutdinov, and H.-J. Freund, "Support Effects on the Atomic Structure of Ultrathin Silica Films on Metals," *Applied Physics Letters*, vol. 100, p. 151608, Apr 9 2012.

[244] S. Shaikhutdinov and H.-J. Freund, "Metal-Supported Aluminosilicate Ultrathin Films as a Versatile Tool for Studying the Surface Chemistry of Zeolites," *ChemPhysChem*, vol. 14, pp. 71–77, Jan 14 2013.

[245] P. Eckerlin and H. Kandler, *Landolt-Börnstein - Group III Condensed Matter, Bd. 6.* Springer Materials, Landolt-Börnstein Database.

[246] X. Xu and D. Goodman, "New Approach to the Preparation of Ultrathin Silicon Dioxide Films at Low Temperatures," *Applied Physics Letters*, vol. 61, pp. 774–776, Aug 17 1992.

[247] F. Sirotti, M. Desantis, and G. Rossi, "Synchrotron-Radiation Photoemission and X-ray-Absorption of Fe Silicides," *Physical Review B*, vol. 48, pp. 8299–8306, Sep 15 1993.

[248] R. Alfonsetti, L. Lozzi, M. Passacantando, P. Picozzi, and S. Santucci, " XPS Studies of $SiO_x$ Thin-Films," *Applied Surface Science*, vol. 70-1, no. A, pp. 222–225, 1993. Session on the Applications of Surface Science and Electronic Materials, at the 12th International Vacuum Congress ( IVC-12 ), The Hague, Netherlands, Oct 12-16, 1992.

[249] S. Chao, Y. Takagi, G. Lucovsky, P. Pai, R. Custer, J. Tyler, and J. Keem, "Chemical-States Study of Si in $SiO_x$ Films Grown by PECVD," *Applied Surface Science*, vol. 26, pp. 575–583, Oct 1986.

[250] E. Paparazzo, M. Fanfoni, E. Severini, and S. Priori, "Evidence of Si-OH Species at the Surface of Aged Silica," *Journal of Vacuum Science & Technology A - Vacuum Surfaces and Films*, vol. 10, pp. 2892–2896, Jul-Aug 1992. 38th National Symp of the American Vacuum Soc, Seattly, WA, Nov 11-15, 1991.

[251] F. Grunthaner, P. Grunthaner, R. Vasquez, B. Lewis, J. Maserjian, and A. Madhukar, "Local Atomic and Electronic-Structure of Oxide-GaAs and $SiO_2$-Si Interfaces Using High-Resolution XPS," *Journal of Vacuum Science & Technology*, vol. 16, no. 5, pp. 1443–1453, 1979.

[252] M. Alexander, R. Short, F. Jones, M. Stollenwerk, J. Zabold, and W. Michaeli, "An X-ray Photoelectron Spectroscopic Investigation into the Chemical Structure of Deposits Formed from Hexamethyldisiloxane/Oxygen Plasmas," *Journal of Materials Science*, vol. 31, pp. 1879–1885, Apr 1 1996.

[253] D. Sprenger, H. Bach, W. Meisel, and P. Gutlich, "XPS Study of Leached Glass Surfaces," *Journal of Non-Crystalline Solids*, vol. 126, pp. 111–129, Dec 1990.

[254] F. Hoffman, M. Weisel, and C. Peden, "Insitu FT-IRAS Study of the CO Oxidation Reaction over Ru(001). 2. Coadsorption of Carbon-Monoxide and Oxygen," *Surface Science*, vol. 253, pp. 59–71, Aug 1991.

[255] B. Yang, E. Emmez, W. E. Kaden, X. Yu, J. A. Boscoboinik, M. Sterrer, S. Shaikhutdinov, and H. J. Freund, "Hydroxylation of Metal-Supported Sheet-Like Silica Films," *Journal of Physical Chemistry C*, vol. 117, pp. 8336–8344, Apr 25 2013.

[256] I. Engquist, I. Lundstrom, B. Liedberg, A. Parikh, and D. Allara, "Infrared Characterization of Amorphous and Polycrystalline $D_2O$ Ice on Controlled Wettability Self-Assembled Alkanethiolate Monolayers," *Journal of Chemical Physics*, vol. 106, pp. 3038–3048, Feb 22 1997.

[257] S. Bordiga, L. Regli, D. Cocina, C. Lamberti, M. Bjorgen, and K. Lillerud, "Assessing the Acidity of High Silica Chabazite H-SSZ-13 by FTIR using CO as Molecular Probe: Comparison with H-SAPO-34," *Journal of Physical Chemistry B*, vol. 109, pp. 2779–2784, Feb 24 2005.

[258] J. A. Boscoboinik, X. Yu, B. Yang, F. D. Fischer, R. Wlodarczyk, M. Sierka, S. Shaikhutdinov, J. Sauer, and H.-J. Freund, "Modeling Zeolites with Metal-Supported Two-Dimensional Aluminosilicate Films," *Angewandte Chemie - International Edition*, vol. 51, no. 24, pp. 6005–6008, 2012.

[259] W. Kaden *et al. PRL*, submitted.

[260] J. A. Boscoboinik, X. Yu, E. Emmez, B. Yang, S. Shaikhutdinov, F. D. Fischer, J. Sauer, and H.-J. Freund, "Interaction of Probe Molecules with Bridging Hydroxyls of Two-Dimensional Zeolites: A Surface Science Approach," *Journal of Physical Chemistry C*, vol. 117, p. 13547, 2013.

# Danksagung

Ich möchte mich an erster Stelle bei Herrn Prof. Freund dafür bedanken, dass er mir Vertrauen entgegengebracht hat und mir die Möglichkeit gegeben hat, in seiner Abteilung am Fritz‑Haber‑Institut meine Arbeit zu erstellen.

Bei Herrn Prof. Dau möchte ich mich dafür bedanken, dass er sich bereit erklärt hat, meine Arbeit zu begutachten.

Meinem Arbeitsgruppenleiter, Dr. Martin Sterrer, bin ich zu großem Dank verpflichtet. Ich habe mich sehr gut aufgehoben gefühlt in seiner Gruppe. Auch hat er die Verwirklichung meiner Ideen immer unterstützt.

Der gesamten Arbeitsgruppe möchte ich an dieser Stelle danken für die gute Arbeitsatmosphäre, die Unterstützung und die vielen schönen Erlebnisse, die wir zusammen hatten.

Auch dem gesamten Kollegium der Abteilung Chemische Physik danke ich für die schöne Zeit.

Ich danke meinen Eltern, meiner Schwester Henriette und meinen Großeltern, die mich leider nicht alle bis zum Ende dieser Arbeit begleiten konnten, für die Unterstützung auf meinem bisherigen Lebensweg und dass sie mich immer ermutigt haben, neue Herausforderungen anzunehmen.

Meinem Freund Björn danke ich dafür, dass er immer für mich da ist, mir stets neue Denkanstöße gibt und mich glücklich macht.

## Selbständigkeitserklärung

Hiermit erkläre ich, dass ich die vorliegende Arbeit selbständig und nur unter Verwendung der angegebenen Quellen und Hilfsmittel angefertigt habe.

Berlin, 2013

Franziska Ringleb

## PUBLICATIONS

1)     M.A. Brown, **F. Ringleb**, Y. Fujimori, M. Sterrer, H. J. Freund, G. Preda, G. Pacchioni, Initial Formation of Positively Charged Gold on MgO(001) Thin Films: Identification by Experiment and Structural Assignment by Theory ,*Journal of Physical Chemistry C*, 2011 , Vol. 115, Nr. 20, 10114–10124

2)     M.A. Brown, Y. Fujimori, **F. Ringleb**, X. Shao, F. Stavale, N. Nilius, M. Sterrer, H. J. Freund, Oxidation of Au by Surface OH: Nucleation and Electronic Structure of Gold on Hydroxylated MgO(001), *Journal of the American Chemical Society*, 2011, Vol. 133, Nr. 27, 10668-10676

3)     **F. Ringleb**, Y. Fujimori*, H. F. Wang, H. Ariga, E. Carrasco, M. Sterrer, H. J. Freund, L. Giordano, G. Pacchioni, J. Goniakowski, Interaction of Water with FeO(111)/Pt(111): Environmental Effects and Influence of Oxygen, *Journal of Physical Chemistry C*, 2011, Vol. 115, Nr. 39, 19328-19335

4)     **F. Ringleb**, M. Sterrer, H.-J. Freund, Preparation of Pd‑MgO model catalysts by deposition of Pd from aqueous precursor solutions onto Ag(001)‑supported MgO(001) thin films, *Applied Catalysis A* (in press)